

Mechanical Characteristics and Adherence of Corrosion Products on Mild Steel

A thesis presented to

the faculty of

the Russ College of Engineering and Technology of Ohio University

In partial fulfillment

of the requirements for the degree

Master of Science

Claudia L. Prieto

December 2019

© 2019 Claudia L. Prieto. All Rights Reserved.

This thesis titled
Mechanical Characteristics and Adherence of Corrosion Products on Mild Steel

by

CLAUDIA L. PRIETO

has been approved for

the Department of Chemical and Biomolecular Engineering
and the Russ College of Engineering and Technology by

David Young

Associate Research Professor of Chemical and Biomolecular Engineering

Mei Wei

Dean, Russ College of Engineering and Technology

ABSTRACT

PRIETO, CLAUDIA L., M.S., December 2019, Chemical Engineering

Mechanical Characteristics and Adherence of Corrosion Products on Mild Steel.

Director of Thesis: David Young

The oil and gas industry often rely on the formation of protective corrosion product layers as a primary barrier against internal transmission pipeline corrosion. The methodologies to assess the protectiveness of such corrosion product layers generally consist of simulating the field environmental conditions where the products are formed coupled with evaluation of their protectiveness through corrosion rate measurements and microscopy. However, the mechanical integrity of the formed corrosion product layers is often neglected. Assessment of the mechanical integrity of corrosion product layers can help in the evaluation and prevention of conditions at which mechanical stresses (such as shear stress exerted by a fluid) or external agents (such as by erodent, *i.e.*, entrained sand and other particles) can impact the protectiveness of the layers, or result in black powder formation. Properties such as layer adherence, fracture toughness and hardness can potentially play a significant role in the previously described scenarios. Consequently, the primary motivation of this research was to characterize corrosion product layers with well-known methodologies utilized in tribology science and wear evaluation.

As a first step, commonly used methods to determine the adherence of layers on substrates in tribology science were tested on fully-developed corrosion product layers, such as iron carbonate and iron sulfide. Once the results were compared with those available in the open literature, testing of the same type of layers, but developed in

dewing conditions, was conducted. Scratch testing was useful to determine the adherence of the tested corrosion product layers. Moreover, the use of scratch testing allowed discrimination of values related to cohesive and adhesive failures, associated with erosion-corrosion and potential problems with localized corrosion, respectively.

After successfully performing the mechanical characterization on different corrosion product layers, it was concluded that the mechanical integrity of the layers cannot be easily challenged by external mechanical forces due to the high values of shear stresses required to delaminate the corrosion product layers (in the order of 10^7 Pa). However, the presence of calcium as a substitutional element in the iron carbonate matrix diminished the mechanical integrity of the layer, making it more susceptible to cohesive failure.

DEDICATION

To my husband, Juan Dominguez Olivo

To my parents, Arnoldo Prieto and Aurora Nieto.

ACKNOWLEDGMENTS

Firstly, I express my total gratitude to my academic advisor and mentor Dr. David Young. Without his guidance, support, and patience, I would never finish my long journey called my Master's degree. I could not ask for a better advisor. I am also grateful to Dr. Marc Singer for supporting me during my studies.

I would like to thank the PI Project and the CC-JIP for financial support of the work performed in this thesis, as well as Dr. Ricardo Nogueira for fruitful discussions. I want to thank Mr. Martin Colahan for all his time and help on dewing conditions corrosion tests as well as Dr. Ezechukwu Anyanwu for sharing critical results pertaining to FeS data. Mr. Hamed Mansoori is thanked for his help in the development of calcium carbonate scales. Mr. Alexis Barxias and Mr. Cody Shafer are thanked for their technical support for my experiments.

I thank Dr. Alain Pailleret from Laboratoire Interfaces et Systèmes Electrochimiques, Université Pierre et Marie Curie, Paris, France. The AFM experiments conducted during my research must be credited to him. Dr. Zineb Belarbi (ICMT, Ohio University) is also thanked for assisting with the AFM work.

Finally, my gratitude is extended to Prof. Srdjan Nesic, who allowed me to join the ICMT group. Dr. Frank Kraft and Dr. Martin Kordesch are also thanked for their willingness to be part of my committee.

TABLE OF CONTENTS

	Page
Abstract.....	3
Dedication.....	5
Acknowledgments.....	6
List of Tables	10
List of Figures	11
Chapter 1: Introduction.....	20
Chapter 2: Background and Literature Review	23
2.1 Corrosion of Steel	23
2.1.1 Corrosion in CO ₂ Environments	23
2.1.2 Formation of Iron Carbonate	24
2.1.3 Formation of Calcium Carbonate.....	25
2.1.4 Corrosion in H ₂ S Environments.....	26
2.1.5 Formation of Iron Sulfide	26
2.2 Corrosion in Dewing Conditions	27
2.3 Black Powder Formation	27
2.4 Adherence of Oxide Scales.....	28
2.5 Stresses on Thin Layers	29
2.5.1 Extrinsic Stresses	29
2.5.2 Intrinsic Stresses	29
2.5.3 Stress Relaxation Processes in Thin Layers.....	31
2.6 Cohesive Failures of Thin Layers	32
2.7 Adhesive Failures of Thin Layers.....	33
2.8 Layer Characterization in Tribology Science	33
2.9 Scratch Testing and Layer Adhesion	34
2.10 Scratch Testing Theory	34
2.11 Fracture Mechanics of Adhesive Films	36
2.11.1 The Energy Criterion for Thin Films.....	37
2.11.2 The Energy Criterion for Flexible Substrates and Brittle Coatings.....	41
2.11.3 Estimation of Compressive Stresses via the Ollivier and Matthews Simplification.....	43

2.11.4	Vickers Indentation Method	44
Chapter 3:	Research Objectives and Hypotheses.....	47
3.1	Objectives	47
3.2	Hypotheses	47
3.2.1	Intrinsic Stress Hypotheses:	47
3.2.2	Extrinsic Stress Hypotheses:.....	48
Chapter 4:	Mechanical Characterization of Iron Carbonate Layers	50
4.1	Introduction.....	50
4.1.1	Mechanical Assessment of Corrosion Product Layers (Iron Carbonate)..	50
4.2	Iron Carbonate Formed in Aqueous Environments	51
4.2.1	Experimental Method.....	52
4.2.2	Results and Discussion	56
4.3	Iron Carbonate in Dewing Conditions	82
4.3.1	Experimental Method.....	82
4.3.2	Results and Discussion	84
4.4	Summary	90
Chapter 5:	Mechanical Characterization of Iron Sulfide Layers	92
5.1	Introduction.....	92
5.2	Iron Sulfide Formed in Aqueous Environments	92
5.2.1	Experimental Method.....	93
5.2.2	Results and Discussion	94
5.3	Iron Sulfide in Dewing Conditions	96
5.3.1	Experimental Method.....	96
5.3.2	Results and Discussion	97
5.4	Comparison of Critical Stresses of Layers Grown under Aqueous vs. Dewing Conditions	108
Chapter 6:	Mechanical Characterization of Calcium Carbonate Scales	110
6.1	Introduction.....	110
6.2	Pure CaCO ₃ layer	111
6.2.1	Experimental Method.....	111
6.2.2	Results and Discussion	112
6.3	Calcium Carbonate Layers with Substitutional Iron Atoms (Fe _x Ca _y CO ₃) ...	122
6.3.1	Experimental Method.....	122

6.3.2	Results and Discussion	122
6.3.3	Day 1 Specimen	124
6.4	Summary	139
6.4.1	Comparison of Mechanical Integrity of FeCO ₃ , CaCO ₃ and Fe _x Ca _y CO ₃	139
Chapter 7: Conclusions and Future work.....		144
7.1	Applicability of Tribology Science Techniques to Corrosion Science.....	144
7.2	Adhesive Properties of Layers Grown under Aqueous and Dewing Conditions 145	
7.3	Presence of Substitutional Calcium in Iron Carbonate Layers	145
7.4	Recommendations and Future Work	147
References.....		149
Appendix A: Characteristics of the API 5L x65 Steel.....		157
Appendix B: Statistical Analysis for the Vickers Indentation Method.....		162
Appendix C: Lateral Force Microscopy		163
Appendix D: Scratch Models for Adhesive and Cohesive Failure		168
	Benjamin and Weaver.....	168
	Laugier	169
	Burnett and Rickerby	170
Appendix E: Preliminary Results on Wearing.....		172
	Introduction.....	172
	Working Hypothesis	173
	Experimental Method.....	174
	Preliminary Results.....	176
	Summary	180
Appendix F: Fracture Toughness at the Cross-Section.....		181
	Introduction.....	181
	Experimental Procedure.....	181
	Iron Carbonate	181
	Calcium Carbonate.....	183
	Iron Calcium Carbonate	185

LIST OF TABLES

	Page
Table 1 Experimental Conditions to Develop a Uniform Layer of Iron Carbonate (FeCO ₃)	52
Table 2 Summary of Hardness Measurements	56
Table 3 Summary of Measurements	63
Table 4 Parameters for Progressive Load Scratch Test on Iron Carbonate (FeCO ₃).....	68
Table 5 Summary of Critical Loads and Shear Stresses	77
Table 6 Experimental Conditions to Develop Iron Carbonate (FeCO ₃) and Mackinawite (FeS) Corrosion Products.....	83
Table 7 Experimental Conditions to Develop a Uniform Layer of Iron Sulfide (FeS) ...	93
Table 8 Scratch Testing Parameters for Iron Sulfide (FeS) Testing	93
Table 9 Experimental Conditions to Develop an Iron Sulfide Layer under Dewing Conditions	97
Table 10 Experimental Conditions to Develop a Calcium Carbonate Layer.....	112
Table 11 Experimental Conditions to Develop an Iron Carbonate Layer with Substitutional calcium.....	122
Table 12 Failures Detected in the Progressive Load Scratch Test.....	125
Table 13 Chemical Composition of the API 5L X65 Steel (wt. %) Used in this Research	158

LIST OF FIGURES

	Page
Figure 1. The general process of polycrystalline film formation: a) nucleation and growth of small crystalline “islands”; b) continued growth of particular small “islands”; c) impingement of crystals due to growth; d) coalescence and deformation of crystals. Adapted from [38].....	31
Figure 2. Stress produced by crystal coalescence and possible mechanisms of stress relaxation: a) crystals with no stress between them; b) tensile stress generated by the impingement of the crystals - the grains deform due to the stress and form the zone colored in gray (if such stress produces plastic deformation, the stress will diminish); c) if the deformation is elastic, the stress in the gray region can be diminished by diffusion of atoms at the crystal boundaries - this condition generates compressive stresses. Adapted from [38].....	32
Figure 3. Delamination of a thin layer due to plastic deformation of the substrate. σ_T is the tangential stress exerted by the indenter. σ_N is the normal force produced by the deformation of the layer as a function of the tangential stress and the Poisson ratio (ν). Adapted from [49].....	36
Figure 4. Shear force exerted by the scratch testing stylus on a layer until detachment. f is the shear force produced by the stylus, t is the thickness of the layer, πa^2 is the projected area of the detached layer at the critical shear force.	38
Figure 5. Three main contributors for the detachment of layers on a substrate: plowing component (a function of F_N), internal stress component (σ_{int}) and tangential force (F_T). μ is the friction coefficient of the layer. Adapted from [49].....	40
Figure 6. The principle of scratching to remove a layer (white) from a metal substrate (gray). Related physical magnitudes are color-related. W is the vertical load of the indenter, P is the vertical pressure exerted by the indenter, related to the load (orange-colored). F is the tangential force and τ the shear stress (red-colored). R is the total radius of the indenter; a is the radius at the critical load (when the indenter reached the metal substrate); h is the thickness of the layer.	42
Figure 7. Types of applied force to generate crack propagation. Mode I corresponds to tensile forces normal to the crack, mode II corresponds to sliding forces (parallel to the crack). Mode III corresponds to the ‘tearing’ mode. The forces are parallel to the crack front. Adapted from [67].....	44
Figure 8. Vickers indentation mark on a brittle material. Cracks generated during the test are related to the fracture toughness. Adapted from [66]	45
Figure 9. Localized corrosion produced by the flow. Adapted from Schmitt, <i>et al.</i> , [15]	51
Figure 10. Three electrode glass cell apparatus.	53
Figure 11. The principle of scratching to remove a layer (white) from a substrate (gray). The indenter cone has radius “ R .” After the scratch, the projected area for the layer	

removal (πa^2) has a radius “a.” These geometrical parameters are used to calculate the critical shear stress [58].	55
Figure 12. Failure map for iron carbonate precipitated on steel. Buckling is the most likely mode of failure for this system.	57
Figure 13. Iron carbonate layer formed.	57
Figure 14. The cross-section area of the iron carbonate layer. EDS confirmed the formation of iron carbonate.	58
Figure 15. Scattered iron carbonate crystals on steel (conditions listed in Table 1). Areas of select crystals marked; the lowest and highest values measured are 1.21 and $4 \mu\text{m}^2$; average crystal area: $2.25 \pm 0.85 \mu\text{m}^2$.	59
Figure 16. Removal process for a single crystal of iron carbonate by AFM: a) zone with single crystals; b) image obtained when a high normal force is applied; c) zone after crystal removal.	60
Figure 17. Topography image of the trace force corresponding to the forward movement of the AFM tip (trace).	60
Figure 18. Lateral force microscopy scan process. Horizontal arrows indicate the direction of the scan. 1) The AFM probe scans the steel in the trace movement. 2) A sudden change in the slope indicated a high torsion of the tip. It is assumed that the tip has reached the crystal. 3) An abrupt change in slope shown that the tip was scanning the steel surface again. 4) The retrace scan started on the steel surface. 5) The crystal was reached when a sudden change in slope was recorded. 6) The abrupt change in slope indicated that the steel surface was reached again by the tip.	62
Figure 19. Friction loops at different stages of the AFM scratch test. Black circular markers represent the trace, and blue triangular markers represent the retrace. Lateral forces calculated, as shown in Appendix C.	63
Figure 20. Schematic illustration of the geometric parameters required for the lateral spring constant calibration. In the figure: t is the height from the point of the tip to the bottom part of the cantilever. Adapted from [80].	64
Figure 21. Tip measurements reported by Xiong <i>et al.</i> [75]. The tip height was measured including the thickness of the cantilever. Such a difference can impact the shear stress calculations by a factor of 1.7.	65
Figure 22. SEM image of a compact iron carbonate layer (3 days, pH 8 ± 0.1 , $80 \text{ }^\circ\text{C}$, initial $[\text{Fe}^{2+}] = 50 \text{ ppm}$, stagnant conditions).	66
Figure 23. Penetration depth of the AFM tip. Reading from right to left: a change in force (V) indicates the distance (nm) at which the sample was reached by the tip (moving downwards). An increase in the force indicates that the tip is applying more force to move further. The double-headed arrow indicates the penetration distance into the iron carbonate layer.	66
Figure 24. SEM image of AFM tip before the test (left) and after scratching the compact iron carbonate layer, the tip was broken (right).	67

Figure 25. Progressive scratch test from 0.1 to 800 mN.....	68
Figure 26. Progressive scratch test results from Figure 25: a) Minimum damage detected force: 35 ± 5 mN; b) Damage of the layer with no detachment (approximately 365 mN); c) removal of the iron carbonate layer at a force of 405 ± 15 mN.....	68
Figure 27. Constant load scratch test at low penetration forces.	69
Figure 28. Constant load scratch test at 30 mN. There is superficial damage, but no detachment of the iron carbonate layer.	70
Figure 29. Profilometry data for different constant load scratch tests.....	70
Figure 30. Depth analysis for different constant load scratch tests.	71
Figure 31. Buckling detection in the iron carbonate layer around the point of failure: a) optical microscope image before the failure; b) and c) failure point; d) and e) standard mapping for buckling failure [46], [84]; f) buckling images of the iron carbonate layer with SEM.	72
Figure 32. Constant load scratch tests at different forces.....	73
Figure 33. Zoomed images of constant load scratch tests at different forces.	74
Figure 34. EDS mapping analysis of constant load scratch tests at different forces.	74
Figure 35. EDS analysis for constant load scratch tests at different forces.....	75
Figure 36. Comparison of calculated shear stresses at selected normal load forces for scratch tests. Blue bars: shear stress calculated by the Ollivier and Matthews formula, per Equation (27). Orange bars: shear stress calculated from experimental frictional forces per Equation (25). Error bars: standard deviation calculated from 5 individual experiments. Critical load determined at 390 mN.	76
Figure 37. Comparison of shear stresses obtained by different techniques [32], [71]. The estimated shear stress to produce cohesive and adhesive failure is of the order of 10^8 Pa.	78
Figure 38. Progressive load scratch test of the iron carbonate in aqueous environments. Solid lines: experimental values. Markers: calculated values by the Olliver and Matthews formulae -as per Equation (28) and Equation (29)- as a function of selected normal forces.....	79
Figure 39. Comparison of the tangential forces obtained at cohesive, adhesive and full delamination with the Ollivier and Matthews approach per Equation (28) and measured experimentally.....	80
Figure 40. Comparison of a progressive load test on bare X65 steel and on a FeCO_3 layer.	81
Figure 41. Vickers hardness mark and crack propagation on iron carbonate.	82
Figure 42. Glass cell apparatus to obtain corrosion product layers under dewing conditions.....	84

Figure 43. SEM image of iron carbonate crystals obtained under dewing conditions. The area of the crystals was calculated assuming a perfect cube. Crystal area: $17 \pm 10 \mu\text{m}^2$.	85
Figure 44. EDS Spectra and quantitative analysis of the crystals developed under CO ₂ dewing conditions.	86
Figure 45. Constant load scratch test to determine the minimum value that produces damage to the crystals.	87
Figure 46. Determination of frictional forces associated with cohesive failure of the iron carbonate crystals.	87
Figure 47. Progressive load scratch test of the iron carbonate in dewing conditions. Solid lines: experimental values. Markers: calculated values by the Olliver and Matthews formulae per Equation (28) and Equation (29) as a function of selected normal forces.	88
Figure 48. Comparison of the tangential forces obtained at cohesive, adhesive and full delamination with the Ollivier and Matthews approach per Equation (28) and measured experimentally.	89
Figure 49. Comparison of critical shear stresses to produce an adhesive failure of iron carbonate layers grown in different conditions.	91
Figure 50. Iron sulfide layer obtained after the 3-day experiment listed in Table 7.	94
Figure 51. XRD pattern showing the presence of mackinawite (M) [87]	94
Figure 52. Progressive load scratch test on mackinawite. SEM images shows a cohesive failure at low forces (<i>ca.</i> 20 mN) and adhesive failure at the range of 150-300 mN of normal force.	95
Figure 53. EDS analysis of forces indicated in Figure 52. SEM images in backscatter mode. Elemental analysis indicates adhesive failure at 300 mN of force.	96
Figure 54. Iron sulfide layer developed in dewing conditions.	97
Figure 55. EDS analysis of the iron sulfide developed in dewing conditions. Quantitative chemical analysis indicated an even presence of iron and sulfur.	98
Figure 56. XRD pattern of the iron sulfide layer. Broad peaks revealed the presence of a poorly crystalline mackinawite layer.	99
Figure 57. Comparison of O&M approach with experimental friction coefficients.	100
Figure 58. a) Constant load scratch test at 240 mN on an FeS layer grown under dewing conditions. b) zoom into the delamination zone during the test.	101
Figure 59. Experimental forces and coefficient of friction (lines) and estimated coefficient of friction (square marker) for a 300 mN constant load scratch test.	102
Figure 60. 300 mN constant load scratch test. Red circle: adhesive failure detected.	102
Figure 61. Parity plot showing the comparison between the calculated friction coefficient (y-axis) vs. the experimental coefficient of friction (x-axis) for different constant load scratch tests.	103

Figure 62. Cross-section analysis of the iron sulfide layer formed under dewing conditions. The thickness of the layer (combining outer and inner layer was $3 \pm 2 \mu\text{m}$).	104
Figure 63. EDS mapping on cross-section analysis of the iron sulfide layer formed under dewing conditions. The analysis revealed that the outer “fluffy” layer is compositionally similar to the inner, compact layer.....	105
Figure 64. Specimen profilometry of a 240 mN constant load scratch test. Penetration by the scratch tester tip: $\sim 2 \mu\text{m}$	106
Figure 65. Specimen profilometry of a 300 mN constant load scratch test. Penetration by the scratch tester tip: $\sim 3 \mu\text{m}$	107
Figure 66. EDS mapping analysis of delamination points of the 300 mN and 600 mN constant load scratch test. Red: sulfur-dominating zones. Green: iron-dominating zones.	108
Figure 67. Comparison of critical shear stresses associated with adhesive failure between iron carbonate layers and iron sulfide layers grown in aqueous and dewing conditions.	109
Figure 68. SEM image of the CaCO_3 scale.....	112
Figure 69. EDS analysis of the corrosion product formed. Oxygen, carbon and calcium are the predominant elements in the chemical composition analysis.	113
Figure 70. XRD pattern of the generated scale (black) compared with the pattern of calcite, CaCO_3 , (red) [87].	114
Figure 71. Progressive load scratch test of the calcite as a scale. Solid lines: experimental values. Markers: calculated values by the Ollivier and Matthews formulae as a function of selected normal forces.	115
Figure 72. Comparison of calculated shear stresses at selected normal load forces for progressive load scratch test. Blue bars: shear stress calculated by the Ollivier and Matthews formula, per Equation (27). Orange bars: shear stress calculated from experimental frictional forces per Equation (25). Error bars: standard deviation calculated from 5 individual experiments. Critical load determined at 600 mN.	116
Figure 73. Adhesive failure of calcium carbonate at 700 mN of normal force. Bright zones are associated with the exposure of the metal substrate.	117
Figure 74. EDS mapping analysis confirming the adhesive failure of calcium carbonate. The iron substrate (in blue) was predominant in the scratch track at the failure.	117
Figure 75. 0.1 mN constant load. Adhesive failure detected.	118
Figure 76. Specimen profilometry of the constant load test at 700 mN. Detected penetration by the scratch tester tip: $\sim 19 \mu\text{m}$	119
Figure 77. Vickers hardness mark and crack propagation on calcium carbonate.....	120
Figure 78. Cross-section analysis of the iron sulfide layer formed under dewing conditions. The thickness of the layer (combining outer and inner layer was $3 \pm 2 \mu\text{m}$).	121

Figure 79. EDS mapping cross-section analysis of the calcium carbonate layer formed as a scale.....	121
Figure 80. Top view and cross-section analysis of the iron/calcium carbonate layers developed after different times (days). The thickness of the layer increased up to 25 μm	123
Figure 81. EDS mapping analysis of the cross section of the iron/calcium carbonate layer developed after different times (days).	123
Figure 82. Progressive load scratch test on a $\text{Fe}_x\text{Ca}_y\text{CO}_3$ layer. Red circle: contact point of the scratch tester. Each arrow indicates the load and the zoomed image of the damage. Zoomed images: a) contact point of the scratch tester tip; b) cohesive failure; c) adhesive failure (first detachment); d) adhesive failure (continuous detachment); e) total removal of the layer.	125
Figure 83. Specimen profilometry of the progressive load test for a range close to 12 mN. Detected penetration by the scratch tester tip: $\sim 7 \mu\text{m}$	126
Figure 84. Specimen profilometry of the progressive load test for a range close to 170 mN. Detected penetration by the scratch tester tip: $\sim 10 \mu\text{m}$	127
Figure 85. Specimen profilometry of the progressive load test for a range close to 420 mN. Detected penetration by the scratch tester tip: $\sim 14 \mu\text{m}$	128
Figure 86. Gross spallation of the calcium/iron carbonate layer: a) SEM in backscatter mode of the calcium/iron carbonate layer; b) adaptation of the ASTM C1624 standard for gross spallation failure mode in ceramics coatings.....	129
Figure 87. Constant load scratch test to corroborate cohesive failure.	130
Figure 88. 100 and 500 mN constant load scratch test to corroborate cohesive failure.	130
Figure 89. SEM image of the scratch track after the 200 mN constant load scratch test. The zoom of the image (right picture) shows the adhesive failure of the layer.....	131
Figure 90. Profilometry of the scratch track after 200 mN constant load scratch test....	132
Figure 91. Cross-section analysis of the scratch track after the 200 mN constant load scratch test compared with the profilometry graph.....	133
Figure 92. Scratch tracks of constant load test. Load forces from 300 to 500 mN.....	134
Figure 93. Scratch tracks of the constant load test. Total removal detected at load forces close to 600 mN.	134
Figure 94. SEM in backscatter mode for a total removal scratch track. 600 mN constant load test.	135
Figure 95. EDS analysis for a total removal scratch track. 600 mN constant load test. .	136
Figure 96. Profilometry for a total removal scratch track. 600 mN constant load test. .	137
Figure 97. SEM and mapping EDS for the cross-section of a total removal scratch track. 600 mN constant load test.....	138

Figure 98. Vickers hardness mark and crack propagation on calcium carbonate with substitutional iron atoms.	139
Figure 99. Mechanical integrity comparison between iron carbonate and iron calcium carbonate layers developed at different days. Minimum shear stress values to produce damage (blue bars), minimum shear stress to produce erosion (orange), and minimum shear stress to produce partial detachment of the layer (gray). Error bars: minimum and maximum values obtained.	140
Figure 100. Fracture comparison between iron carbonate and iron calcium carbonate layers developed at different days.....	142
Figure 101. Correlation between minimum shear stress to produce erosion and fracture toughness in the calcium carbonate and iron carbonate layer developed at different days. Vertical error bars: maximum and minimum values of fracture toughness. Horizontal error bars: maximum and minimum values of shear stress.....	142
Figure 102. Correlation between minimum shear stress to produce partial delamination and fracture toughness in the calcium carbonate and iron carbonate layer developed at different days. Vertical error bars: maximum and minimum values of fracture toughness. Horizontal error bars: maximum and minimum values of shear stress.	143
Figure 103. Correlation between minimum shear stress to produce damage and fracture toughness in the calcium carbonate and iron carbonate layer developed at different days. Vertical error bars: maximum and minimum values of fracture toughness. Horizontal error bars: maximum and minimum values of shear stress.....	143
Figure 104. Crystal structures of iron's different phases. Face-centered cubic (FCC) corresponds to austenite or γ -iron; body-centered cubic (BCC) corresponds to α and δ -ferrite. The body-centered tetragonal unit cell (BCT) corresponds to a diffusionless transformation phase called martensite. Adapted from [92]......	157
Figure 105. Binary phase diagram of iron (Fe) and carbon (C). Thermodynamically stable phases are shown: α -ferrite, γ -iron (austenite), δ -ferrite and cementite (Fe_3C). A1 is the eutectoid temperature; A2 is the α -ferrite austenitic transformation temperature; A3 denotes the hypoeutectoid temperature of austenite transformation; A_{CM} is the hypereutectoid temperature of austenitization. Retrieved from https://upload.wikimedia.org/wikipedia/commons/thumb/e/e1/Fe-C.svg/2000px-Fe-C.svg.png [Accessed: 02-Jan-2017].	158
Figure 106. Thermo-mechanical control process. A_{r3} denotes the hypoeutectoid temperature of austenitic transformation and A_{r1} the eutectoid temperature. Adapted from [96]......	160
Figure 107. Microstructure of the proposed X65 steel. Ferrite is the predominant phase.	160
Figure 108. SEM images of the microstructure of the proposed X65 steel. Ferrite is the predominant phase.	161
Figure 109. XRD pattern of the X65 steel showing the presence of ferrite.....	161

- Figure 110. Blue bars represent the average value of each load population. Error bars: standard deviation for each load population. Horizontal black solid line: average of the whole sample population. Horizontal dashed lines: ± 1 standard deviation of the whole sample population. 162
- Figure 111. Basic principle of atomic force microscopy (AFM). A cantilever is placed upon a sample surface. The XYZ piezo actuator moves the sample in any desired direction in the XYZ plane. Such movements in combination with the sample interface morphology generate a torsion / bending on the cantilever. The photo sensor registers the movements of the cantilever as the displacement of the laser beam reflected from the cantilever is proportional to the torsion/bending of the cantilever. The controller sends a feedback signal to the piezo actuator for a more precise movement. 163
- Figure 112. Torsion angle (β) of the cantilever generated by lateral displacement of the cantilever. L is the length of the cantilever; l is the height of the tip; w is the width and t is the thickness of the cantilever. 164
- Figure 113. Changes in the laser deflection due to torsion recorded by the photo sensor. At the right, the forward displacement of the cantilever (trace) generates a positive deflection of the laser beam on the photo sensor. At the left, the backward movement of the cantilever (retrace) generates a negative deflection of the laser beam on the photo sensor. Such deflection is proportional to the friction force between the tip and the sample's surface. 164
- Figure 114. Voltage recorded from the lateral displacement of the cantilever. In the graph: x-axis represents the lateral displacement, y-axis represents the voltage recorded in the displacement of the cantilever. ΔV is the difference in voltage between the forward (trace) and backward (retrace) displacement of the cantilever. 165
- Figure 115. Voltage-displacement curves for vertical and lateral displacement. 166
- Figure 116. Types of wear curve. Adapted from [91] 173
- Figure 117. Multiple-pass constant load scratch test to determine the diminution of the layer thickness. 175
- Figure 118. The partial volume of a sphere based on height (h). R is the radius of the tip, a is the scratch width left by the test; α is the angle formed between R and a 175
- Figure 119. Progressive load scratch test to determine the working force for the wear test. 176
- Figure 120. Constant load scratch test to determine the working force for wear test. 177
- Figure 121. Constant load scratch test to determine the working force for the wear test. 177
- Figure 122. Multiple-pass scratch test. Top graph: loading force through multiple passes on the same zone. Lower graph: penetration measured by the scratch tester at different passes. 178
- Figure 123. Wear volume curve for the polished iron carbonate layer. Wearing rates (WR) suggest that the wear is obeying the Type III wear curve behavior. 179

Figure 124. Profilometry of a 6-pass 70mN constant load scratch test, and a single pass 420 mN constant load scratch test.	180
Figure 125. First attempt to determine the K_{IC} mode fracture toughness in the cross-section of iron carbonate. The crack propagation was stopped by the epoxy and the metal-layer interface.....	182
Figure 126. Determination of K_{IC} mode fracture toughness in the cross section of an iron carbonate layer.	183
Figure 127. Determination of K_{IC} mode fracture toughness in the cross-section of a calcium carbonate layer.	184
Figure 128. Zoomed image of the Vickers' indentation print from Figure 127.	184
Figure 129. Indentation pattern for fracture toughness determination.	185
Figure 130. Zoomed image of the Vickers' indentation prints from Figure 129.....	185
Figure 131. Summary of fracture toughness (K_{IC}) obtained at the cross-section and the top view of the layers.	186

CHAPTER 1: INTRODUCTION

The oil and gas industry produces a large variety of products essential to everyday life, such as gasoline, diesel, and natural gas as fuels as well as petrochemical feedstocks used to make a wide range of products. In order to transport refined products as liquids or gases to customers, the oil and gas industry frequently uses transmission pipelines. One of the operational problems associated with gas transmission pipelines is the formation of black powder [1]. As its name suggests, black powder is blackish dust that can impact the performance of transportation pipelines due to its accumulation, even resulting in pipelines potentially becoming blocked [1], [2]. This blockage affects the flow of gas, thereby reducing the amount that is delivered to the end user. In terms of pipeline integrity, black powder causes erosion of the internal pipe wall, compromises the functioning of critical components (e.g., sensors, valves), and induces pressure drop due to the variation of internal diameter [3]. Gas turbine blades are also susceptible to damage caused by black powder accumulation [3].

Even though the compositions of black powder have been well characterized and reported [1], [3]–[5], mechanisms relating to how it forms as a corrosion product, detaches and becomes pulverized to form an entrained powder are poorly understood [6]. While the chemical analysis of black powder provides critical data relating to the chemistry and thermodynamics governing its formation, the reasons for its spallation and detachment from pipe surfaces remains unsatisfactorily unanswered; most black powder studies have focused on its characterization and impact rather than mechanistic elucidations of its formation [6]–[9]. Black powder prevention methods involve the

injection of volatile corrosion inhibitors (VCIs) or monoethyleneglycol (MEG) to minimize the formation of corrosion products or avoid condensation of water; VCI and MEG can be introduced together [2], [6], [7]. However, the application of those compounds may be impractical for some gas companies. Mechanistic elucidation can facilitate appropriate tailoring of mitigation strategies for particular situations. Therefore, understanding mechanisms of spallation are essential so that conditions at which corrosion products form black powder can be avoided, predicted, or mitigated.

As a secondary outcome, the study of mechanical properties of corrosion product layers can potentially help explain the influence of mechanical stresses on the protectiveness of fully-developed corrosion product layers in oil transmission pipelines. Therefore, the focus of this thesis research was to establish if and how internal stresses within developing corrosion product layers can lead to the formation of black powder as well as the detachment of fully-developed corrosion product layers. In order to achieve the objectives, the most important factors that cause internal stresses were evaluated [10]–[12]. Heretofore the methodologies used for characterizing the growth of iron carbonate have been primarily based upon microscopic observations [13], [14], determination of shear stress resistance and fractomechanical properties of this particular corrosion product; focused on measurements involving single crystals or fully-developed dense layers [15]–[17]. Even though the chemical composition of corrosion products may be the same, corrosion product layers formed in dewing conditions are not as dense as would be the case for a fully developed corrosion product layer. The corrosion product may also not exist as a distribution of relatively uniform, discrete crystals, further

limiting the ability to measure their adherence characteristics individually. Therefore, morphology and mechanical properties of compositionally identical corrosion products may be different depending on their mode of formation. Intrinsic stresses within such polycrystalline corrosion product layers, as well as external stresses such as thermal stresses therein, have heretofore been generally neglected. However, they are postulated to play an essential role in corrosion product layer development and retention, hence spallation, in dewing conditions. Consequently, if the proposed research determines the tendency of corrosion products on steel to undergo spallation related to evolving stresses with loss of adherence, then this knowledge can potentially be applied for the development of black powder prevention strategies. Also, the proposed research has the potential to add to the understanding of localized corrosion mechanisms associated with local detachment of iron carbonate and iron sulfide.

CHAPTER 2: BACKGROUND AND LITERATURE REVIEW

2.1 Corrosion of Steel

Corrosion of mild steel in acidic environments is the oxidative dissolution of iron with accompanying hydrogen ion reduction [18]:



The acidity is due to the presence of hydrogen sulfide (H₂S), organic acids such as acetic acid (CH₃CO₂H), or carbonic acid (H₂CO₃) derived from aqueous carbon dioxide (CO₂) [18].

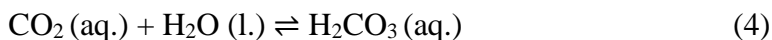
2.1.1 Corrosion in CO₂ Environments

The corrosion of steel pipelines in aqueous environments containing CO₂ is due to the formation of carbonic acid, formed as shown in the below reactions [19].

1. Dissolution of carbon dioxide (CO₂) in water:



2. Formation of carbonic acid (H₂CO₃) by hydration of aqueous carbon dioxide:



Remita, *et al.*, [20] reported that the main role of carbonic acid is to replenish the supply of hydrogen ions as they are consumed by the previously shown cathodic hydrogen ion reduction reaction. This mechanism is called the “buffering effect” and can be described by the following dissociation reactions. [19], [20]

1. Dissociation of carbonic acid into hydrogen ion and bicarbonate ion:



2. Dissociation of bicarbonate ion into carbonate ion and hydrogen ion:



Remita [20] concluded that the corrosion of iron could be adequately explained by the reduction of hydrogen ion and, therefore, the direct reduction of carbonic acid is not the primary mechanism of corrosion in CO₂ environments as previously described by other researchers [19], [21], [22].

2.1.2 Formation of Iron Carbonate

The main product due to corrosion of steel in the presence of CO₂ is iron carbonate (FeCO₃) [23]. The iron carbonate is formed through precipitation, by its heterogeneous nucleation and growth, on the metal surface [23]. The overall reaction is:



The precipitation of iron carbonate is assumed to be governed by the solubility product (K_{sp}) and crystal growth rate [22], [23]. The crystal growth rate (R_{gr}) in mol/m² s can be described with a non-elementary rate equation [24], Equation (8):

$$R_{gr} = e^{A - \frac{B}{RT}} K_{sp} (S - 1) \quad (8)$$

Where A and B are kinetic constants (with values of 28.2 and 64.85 kJ/mol, respectively), K_{sp} is the solubility product, in (mol/L)² (assuming the density of water is equal to 1 kg/L) which is a function of the absolute temperature (T , in Kelvin) and ionic strength (I , in mol/L) as determined by Equation (9) [25]:

$$\log |K_{sp}| = -59.3498 - 0.041377T - \frac{2.1963}{T} + 24.5724 \log |T| + 2.518I^{0.5} - 0.657I \quad (9)$$

Finally, S is the saturation value, which is a function of ferrous ion concentration (Fe^{2+}), carbonate ion concentration (CO_3^{2-}), and solubility product as defined by Equation (10):

$$S = \frac{[\text{Fe}^{2+}][\text{CO}_3^{2-}]}{K_{sp}} \quad (10)$$

When the value of S determined by Equation (10) is more significant than unity the resultant condition is termed as supersaturation, which is favorable for the formation of iron carbonate [22], [24], [25]. Research has also demonstrated that the main parameters that affect the formation of a layer of iron carbonate are water chemistry, pH and temperature [26].

2.1.3 Formation of Calcium Carbonate

The presence of calcium ions (Ca^{2+}) in transmission pipelines has the potential to lead to the formation of calcium carbonate (CaCO_3 , also known as calcite) in CO_2 corrosion environments [27]. The mechanism of formation is akin to that for iron carbonate; precipitation occurs when the solubility limit is exceeded [27]. Since calcium and iron carbonate are isostructural (possess the same crystal structure), the precipitation of both might lead to a solid solution in the form of $\text{Fe}_x\text{Ca}_y\text{CO}_3$ [27], where $x + y = 1$. Details on the mechanism of precipitation are summarized by Mansoori, *et al.*, in their study of how Ca^{2+} in brines can influence CO_2 corrosion [27]. The presence of substitutional calcium in a protective iron carbonate layer can potentially compromise the mechanical integrity of the aforementioned layer, making it susceptible to mechanical removal.

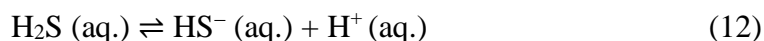
2.1.4 Corrosion in H₂S Environments

The water chemistry in H₂S corrosion follows a similar set of reactions as in CO₂ corrosion, except that aqueous H₂S itself is acidic. The fundamental reactions are as follows.

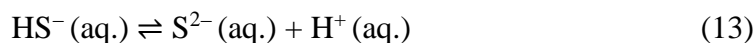
1. Dissolution of hydrogen sulfide (H₂S) in water:



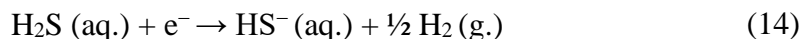
2. Dissociation of hydrogen sulfide into bisulfide ion:



3. Dissociation of bisulfide ion into sulfide ion:



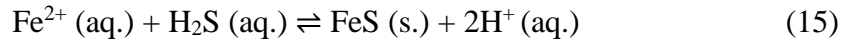
An extra electrochemical reaction (direct reduction of H₂S) is also considered [28], [29]:



2.1.5 Formation of Iron Sulfide

Even though the corrosion of steel by the direct reduction of H₂S might produce several different crystalline structures of iron sulfide (FeS) [28], mackinawite and cubic iron sulfide are the most common forms reported in top-of-the-line corrosion (TLC) environments [30]. Top-of-the-line corrosion is defined as the corrosion encountered in stratified flow regimes in which condensation happens and promotes corrosion at the 12 o'clock position in a tubular in the presence of organic acids, H₂S or CO₂ [31]. Due to similarities in the water chemistry conditions for TLC with dewing corrosion and fast kinetics, mackinawite will primarily form in H₂S containing environments.

The kinetics of precipitation of iron sulfide, in the form of mackinawite, are faster than iron carbonate precipitation [28]. The overall reaction is given by [28], [29]:



In analogy to iron carbonate, the likelihood of precipitation of mackinawite can be expressed in terms of iron sulfide saturation in the function of the H_2S and H^+ concentration [24]:

$$S_{FeS} = \frac{[\text{Fe}^{2+}][\text{H}_2\text{S}]}{K_{sp,\text{H}_2\text{S}}[\text{H}^+]^2} \quad (16)$$

Where S_{FeS} is the saturation of iron sulfide and $K_{sp,\text{H}_2\text{S}}$ is the solubility limit of iron sulfide in an acidic environment; the reverse of reaction (15).

2.2 Corrosion in Dewing Conditions

When a sales gas pipeline is transporting natural gas and if its relative humidity is sufficiently high, water will condense on the internal pipe surface [31]. This condensed water, in combination with an acid gas such as carbon dioxide (CO_2), corrodes the pipe and generates corrosion products [18], [22], [31]. Spallation of corrosion products causes black powder formation [1], [2], [6].

2.3 Black Powder Formation

Thus far, how corrosion products form has been briefly reviewed. The next step in the formation of black powder is related to the detachment of the corrosion product from the steel surface. Consequently, the mechanical integrity of corrosion product layers plays a governing role in the formation of black powder. Past research on the adherence of iron carbonate grown on steel has demonstrated that the adherence force between them

is such that up to 10-50 MPa of stress can be sustained [32]. However, in the same study, contributions to adherence *via* inter-crystal interactions were undiscussed [32]. In another study, the fractomechanical properties of a fully grown and dense iron carbonate layer were determined [15]. The high values obtained for adhesion between the iron carbonate layer and steel (8-18 MPa) led to the conclusion that wall shear (extrinsic) stress is not a factor for the delamination/detachment of iron carbonate [15]. Addressing the mechanical integrity of iron sulfide corrosion products on steel, Sun, *et al.*, proposed that their spallation is a natural process governed by the development of intralayer intrinsic stresses [24]. Consequently, the development of intrinsic strain and stress during the growth of iron carbonate and iron sulfide is postulated to be a critical parameter associated with corrosion product spallation [33].

Despite the conclusions of the researches above, the conditions in the discussed studies are different from corrosion in dewing conditions. Consequently, the corrosion product layers could potentially exhibit different behavior due to the presence of environmental factors that have, thus far, been neglected by the corrosion research community. Bearing that in mind, critical parameters and associated characterization techniques used in tribology to evaluate fractomechanical properties of thin layers are discussed below with a view to their potential application for the assessment of the mechanical integrity of corrosion product layers.

2.4 Adherence of Oxide Scales

The adherence of oxide scales has been studied by different experimental approaches. Robertson proposed that oxides formed on a metal surface (Fe_3O_4 , Cr_2O_3 ,

Al₂O₃, SiO₂, and NiO) spall when the strain energy of the product exceeds a critical point [34], Young's modulus and the thickness of the oxide layer were used as parameters to determine such critical points [34]. Burnett, *et al.*, determined a comprehensive relationship between the hardness and adhesion of titanium nitride (TiN) as a surface coating based upon microhardness measurements [35], [36].

2.5 Stresses on Thin Layers

Stresses can be described as being either extrinsic or intrinsic, implying they are generated by external or internal factors, respectively [10], [11], [37]. When a polycrystalline layer is grown on a substrate, it can be subject to both extrinsic and intrinsic stresses. Such stresses, in combination or by themselves, have the potential to cause buckling, fracturing, and eventual spallation of the layer.

2.5.1 Extrinsic Stresses

Extrinsic stresses are produced by external factors such as:

- Mechanical applied stresses: External forces that cause the substrate and/or layer to deform such as by wall shear stress produced by fluid flow [33].
- Thermal stresses: Due to differing thermal expansion coefficients the substrate can expand more or less than the layer, causing compression or tension that can result in layer fracturing [33].

2.5.2 Intrinsic Stresses

Intrinsic stresses are related to the growth and morphology of the crystalline layer on the substrate. The general process of the growth of a crystalline layer on a substrate is depicted in Figure 1. There are several possible sources of intrinsic stresses, including:

- Misfit (epitaxial) stresses: caused during film growth due to a misfit between the lattice of the substrate and the film. Such stresses can be heterogeneous (between two different compounds such as calcium carbonate and iron carbonate) or homogeneous (growth of multilayers) [38].
- Coalescence of Grain Boundaries: the growth of the layer starts with discrete “islands” that gradually and incrementally increase their size up to a point where they impinge against each other and coalesce [38]. Furthermore, grain coarsening may occur for polycrystalline layers [38], or all the voids are filled, so a continuous layer is formed. These phenomena can result in forces being generated between grains that have the potential to produce deformation.
- Grain Growth: The stresses are increased due to the increase in the size of grains. The layer may experience tensile stresses if the relaxation process does not release all the stresses generated during the growth and impingement between grains. Thereby, a denser layer may be under more compressive stress than one which is porous [39].
- Insertion of Excess Atoms: This condition refers to the nucleation of non-stoichiometric compounds that have an excess of atoms in their crystalline structure [40]. As a consequence, compressive stresses are generated in the lattice.
- Co-nucleation and Growth: Intrinsic stresses can develop when two or more different compounds undergo nucleation and grow on the same surface [39], [41]–[43]. The result is an inhomogeneous layer with residual tensile stresses in the lattice [39]–[41]. It can be thought of as two nucleation processes of two different

corrosion products that occur at the same time (*i.e.*, calcium carbonate and iron carbonate) with their subsequent growth.

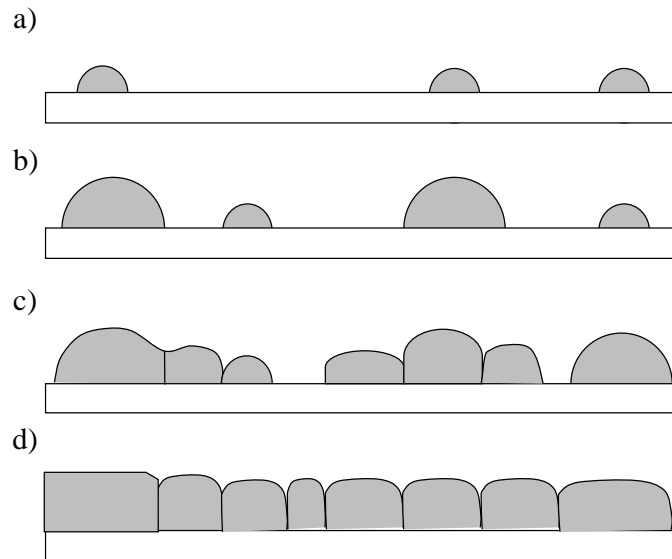


Figure 1. The general process of polycrystalline film formation: a) nucleation and growth of small crystalline “islands”; b) continued growth of particular small “islands”; c) impingement of crystals due to growth; d) coalescence and deformation of crystals. Adapted from [38].

2.5.3 Stress Relaxation Processes in Thin Layers

Floro, *et al.*, [38] have reported that, during the formation of a film, the stresses generated might diminish due to stress relaxation processes. In general, a stress relaxation process in a thin polycrystalline layer can be defined as the diminishing of stresses within the layer structure because of an internal reorganization of crystals [44]. The internal reorganization is often driven by thermal energy that facilitates plastic deformation of the crystals or promotes atom diffusion at their boundaries [42]. These possible mechanisms of relaxation are illustrated in Figure 2.

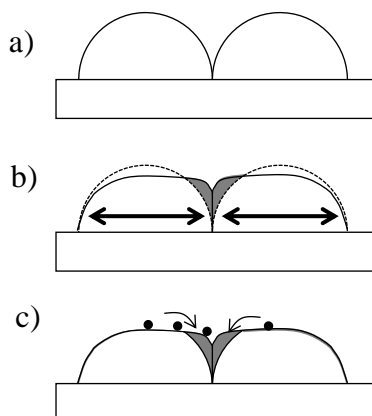


Figure 2. Stress produced by crystal coalescence and possible mechanisms of stress relaxation: a) crystals with no stress between them; b) tensile stress generated by the impingement of the crystals - the grains deform due to the stress and form the zone colored in gray (if such stress produces plastic deformation, the stress will diminish); c) if the deformation is elastic, the stress in the gray region can be diminished by diffusion of atoms at the crystal boundaries - this condition generates compressive stresses. Adapted from [38].

When these layers become fully developed, *i.e.*, when complete surface coverage is achieved, the tensile stresses are generally diminished by atom diffusion [12], [34], [38]. As the stresses within an atom diffusion stress-relaxed layer are mostly compressive, the resistance to interfacial shear stresses can be significantly increased [38], [44]. However, this resistance will be reduced if the layer is porous and/or inhomogeneous. In general, if a layer is porous, then tensile stresses will not undergo relaxation by atom diffusion [38]. In inhomogeneous layers, the different morphologies, and potentially compositions, of co-nucleated compounds may also hinder the relaxation process.

2.6 Cohesive Failures of Thin Layers

Cohesive failures are related to the partial delamination that can occur at the gas-film interface [39], [45]. The most commonly reported forms of cohesive failures are

buckling and spallation [46]. The partial delamination is generally caused by external agents such as shear stress exerted by a fluid [36]. Various causes are the internal stresses within the film. Consequently, the relaxation processes and distribution of such external stresses are the governing parameters for this type of failure [38].

2.7 Adhesive Failures of Thin Layers

This failure refers to the total detachment of a thin film from the substrate [47]. Such a condition is reported to be produced by external mechanical forces such as shear stresses generated with industrial cutting tools [39], [45]. The forces required to produce this type of failure are generally higher than the forces to produce a cohesive failure [46]. The bonding between the film and the substrate plays a governing role on this type of failure as well as other internal stresses within the layer [48]. Bull, *et al.*, have discussed the contribution of the abovementioned internal stresses in the practical assessment of adhesion of thin layers [49]. The author concluded that the friction drag force is the sum of the contribution of all the forces involved in the adhesion of a thin layer [49]. Such a postulate is further discussed in the scratch testing theory section.

2.8 Layer Characterization in Tribology Science

Microindentation methods and scratch testing are techniques commonly used in tribology science to assess the mechanical integrity of thin layers [12], [46], [47]. These methods are solidly grounded in theory and the information obtained from them is reported to be highly repeatable and meaningful [47], [50], [51]. Microindentation methods give information about the internal stresses, hardness and elastic properties of layers [47]. Scratch testing is significant as information about shear stress for initial

delamination (the minimal force required to detach a portion of the layer without reaching the substrate related to cohesive failure) [50], and complete delamination (related to the adhesion force) [50] can be obtained. Since the scratch testing is based on fracture mechanics principles, the next section discusses the theory behind the test, as well as the most common assumptions and simplifications.

2.9 Scratch Testing and Layer Adhesion

Scratch testing is a tribological technique widely utilized, among other applications, in the determination of adhesive forces between a substrate and thin layers [49], [52], [53]. This method is considered a robust technique to obtain information about the adhesion of a film on a substrate [49], [54]. The method can capture the three primary contributing parameters that govern the adhesion phenomena between a thin film/coating/layer and a substrate: internal stresses within a layer, the adhesive friction between the stylus and the contacted surface, and the plowing contribution of the indenter. These three critical parameters are discussed below.

2.10 Scratch Testing Theory

The scratch testing analysis is primarily based on the theory of sliding friction between metals developed by Tabor [55]. In general, friction can be defined as the force required to initiate or maintain motion between two bodies in contact [56]. Therefore, Tabor defined sliding friction as a surface phenomenon that depends on various factors related to the nature of the surface, such as asperity, lubrication, and the strain-stress relation of each of the two solids [55]. It is generally assumed that two fundamental laws of friction are obeyed [55]:

1. The friction force is proportional to the normal force between surfaces, and
2. The friction force is independent of the area of contact (since pressure/stress is equal to the force divided by the contact area).

These laws are usually observed by sliding metals, whereas polymeric solids might significantly deviate from these two laws [55], [57], [58]. Finally, a distinction between kinetic and static friction must be made. Static friction is the required force to initiate the motion of one of the bodies, while kinetic friction is the force required to maintain the movement of the body at a specified speed [55].

In his work, Tabor concluded that friction involves three significant factors: the area of real contact between the surfaces (A), the bonding or adhesive forces between the contact regions, and the shearing forces during sliding. The force to initiate sliding is given by:

$$F = As + P \quad (17)$$

Where s is the specific shear strength of the interface, and P is a deformation or plowing term. The use of a deformation term implies that a harder surface is sliding over a softer one [55].

The initial ideas of friction and deformation from Tabor were taken by Benjamin and Weaver to analyze the results obtained from scratch testing [59]. They proposed a comprehensive mathematical model that assumed fully plastic deformation of the substrate for coating removal (as depicted by Figure 3). Frictional forces between the indenter and the layer (σ_T), as well as the thickness and Poisson ratio (ν) of the layer, were the crucial factors that the authors took into consideration.

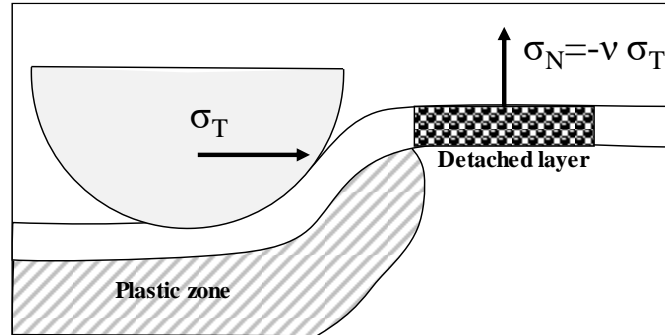


Figure 3. Delamination of a thin layer due to plastic deformation of the substrate. σ_T is the tangential stress exerted by the indenter. σ_N is the normal force produced by the deformation of the layer as a function of the tangential stress and the Poisson ratio (ν). Adapted from [49].

However, the assumption of fully plastic deformation of the substrate made impractical the application of the model for many systems since brittle coatings tend to fail before plastic deformation of the substrate occurs [36], [49], [60].

In order to overcome the drawbacks of the Benjamin and Weaver model, Laugier proposed a comprehensive energy criterion that could be extended to different modes of failure, *i.e.*, brittle films on hard substrates or hard films on flexible substrates. The basic principle was straightforward, that detachment of a layer occurs when the interfacial shear stress reaches a critical value [61], [62]; this critical value depends on the fracture mechanics properties of the film. In the next section, the fracture mechanics principles of films deposited on a substrate are reviewed.

2.11 Fracture Mechanics of Adhesive Films

Fracture mechanics is the study of crack propagation in materials [63]. The basics and historical evolution of this field are outlined elsewhere [63]. For the purpose of this thesis, the discussion is centered on the fact that fracture mechanics has two different

approaches to analyze fracture propagation: the stress intensity approach and the energy criterion [63]. Since the energy criterion is fundamental for the scratch testing adhesion analysis proposed by Laugier [62], it will be discussed in detail. The stress intensity approach is out of the scope of the present thesis.

2.11.1 *The Energy Criterion for Thin Films*

The energy criterion for the fracture of a solid material undergoing sliding friction with another was proposed initially by Griffith [64]. In simple terms, the energy approach says that the fracture of materials occurs when the energy available in a surface to form a crack overcomes the resistance of a material. Griffith postulated that the surface energies could be obtained from an energy balance when a fracture/crack of the less resistant solid occurs due to an external stress [64]. The energy balance for the depicted scenario results in Equation (18):

$$U = \frac{1}{V} \int f dx \quad (18)$$

Where U is the strain energy per unit volume of detached material, V is the volume of the stressed material, and f is the tangential force producing strain (ε) along the x-axis. Equation (18) can be simplified by stating that the volume of the stressed material can be expressed as $V = AL$; where A is the area and L is the length of the stressed material.

$$U = \int \frac{1}{AL} f dx$$

Recognizing that $f/A = \sigma$ (stress) and x/L is the strain (ε):

$$U = \sigma \int d\varepsilon \quad (19)$$

If the behavior of the material is linear, *i.e.*, the stress is proportional to the strain, then $\sigma = E\varepsilon$, where E is the Young's modulus. Equation (19) can then be expressed as:

$$U = E \int \varepsilon d\varepsilon \quad (20)$$

Evaluating the integral under the limits from zero to a strain ε :

$$U = \frac{E\varepsilon^2}{2} \quad (21)$$

Finally, with the linear proportionality between stress and strain $\sigma = E\varepsilon$, the strain energy per unit volume of stressed material results in:

$$U = \frac{\sigma^2}{2E} \quad (22)$$

By using a similar approach, Laugier derived the energy balance for the case of the scratch test stylus is acting on a film that experienced detachment as depicted by Figure 4 [62].

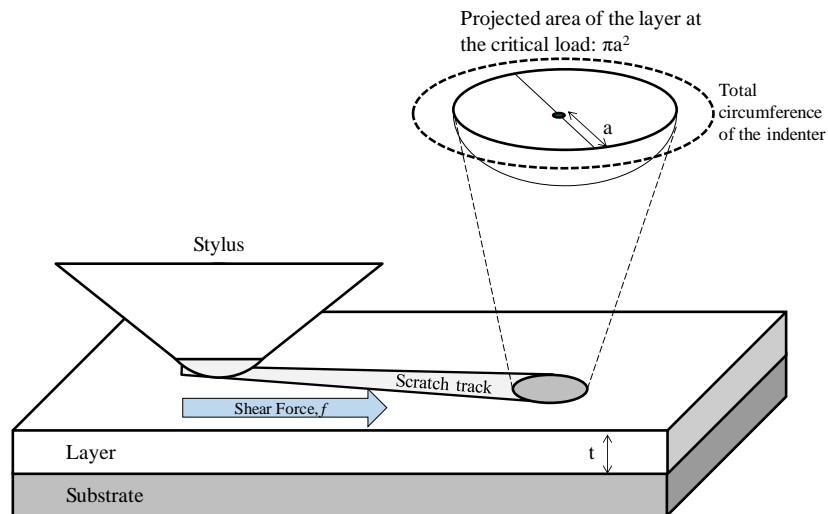


Figure 4. Shear force exerted by the scratch testing stylus on a layer until detachment. f is the shear force produced by the stylus, t is the thickness of the layer, πa^2 is the projected area of the detached layer at the critical shear force.

From Equation (22), and using the geometric parameters listed in Figure 4, Laugier obtained the released elastic energy (E_R):

$$E_R = \frac{\pi a^2 t}{2} \frac{\sigma^2}{E} \quad (23)$$

The released elastic energy can be interpreted as the surface energy available to produce a crack/detachment. Under this definition, Laugier related the detachment to the work of adhesion (W_{adh}). The work of adhesion is related to the surface energy of the substrate (γ_s), the surface energy of the layer (γ_l) and the interfacial energy between them (γ_{sl}), as shown in Equation (24).

$$W_{adh} = \gamma_s + \gamma_l - \gamma_{sl} \quad (24)$$

However, as recently discussed by Kappl, *et al.*, [56] Equation (24) was primarily intended to model the behavior of two immiscible liquids at their interface. In the case of solids, surface roughness usually has a dominating influence on the experimental adhesion force [56]. Therefore, the authors strongly suggested that their work on adhesion must be used only for liquids [56]. The role of the roughness in the adhesion force can explain the inconsistencies between the experimental adhesion forces and the forces calculated by the Laugier approach reported by Bull, *et al.* [49] Nonetheless, the contribution of Laugier must not be minimized. Burnett, Rickerby, and Bull utilized the same fundamental approach of Laugier (energy balance approach) to identify three main forces contributing to the layer detachment: elastic-plastic indentation stress, internal stresses, and tangential frictional stress as shown in Figure 5 [49].

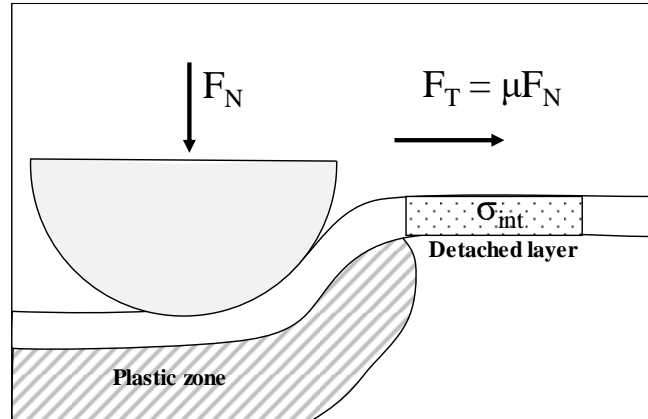


Figure 5. Three main contributors for the detachment of layers on a substrate: plowing component (a function of F_N), internal stress component (σ_{int}) and tangential force (F_T). μ is the friction coefficient of the layer. Adapted from [49].

Bull, *et al.*, also proposed that the tangential forces measured by the scratch adhesion test are a function of the plowing term, the friction coefficient, and the internal stresses that add an extra resistance tangential force [49].

The fundamental postulate from Tabor [55] (in the form of Equation (17)) can then be used to model the behavior of the friction forces from the scratch test: the plowing term accounts for the formation of the scratch track and the adhesion term for the critical shear stress to remove the layer. It is essential to mention that Bull, *et al.*, distinguished the adhesive failures produced by tensile forces and failures produced by compressive forces [46]. The type of failure depends on the nature of the interaction of the layer and the substrate and can be detected by microscopy [46], [53]. Therefore, a microscopic inspection must be performed before choosing the model equation to obtain the critical shear stress for failures. If the failure is governed by compressive stresses (τ_c), the model equation is given by:

$$\tau_c = \frac{F_T}{A} \quad (25)$$

Whereas if the tensile stress is causing the detachment of the layer, the model equation for the critical shear stress (τ_i) is given by:

$$\tau_i = \frac{\nu_i F_T}{A} \quad (26)$$

Where ν_i is the Poisson ratio of the layer.

2.11.2 *The Energy Criterion for Flexible Substrates and Brittle Coatings*

Ollivier and Matthews simplified the energy criterion proposed by Laugier and Bull to develop a mathematical model for hard thin films deposited in a flexible substrate [58]. Although simple, this model is in good agreement with the experimental observations of Laugier, Perry, and Weaver [59]–[61]. Ollivier and Matthews assumed that, at the critical load, the plastic deformation of the substrate is negligible for flexible substrates. There is also an implicit assumption that the scratch testing process is performed quasi-statically. In other words, quasi-static implies that the process occurs so slowly that the static analysis of the forces is valid. Moreover, it is also assumed that the plowing force exerted by the tip is significantly higher than the static/dynamic friction. Consequently, the tangential force is directly associated with the plowing term as a direct function of the normal force, independent from the substrate.

Figure 6 shows the geometrical parameters and forces involved in the determination of the tangential force to further transform it into shear stress.

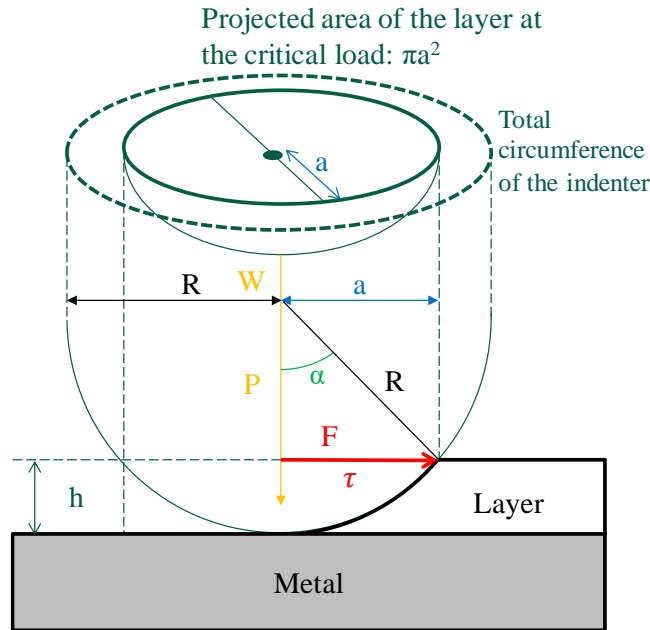


Figure 6. The principle of scratching to remove a layer (white) from a metal substrate (gray). Related physical magnitudes are color-related. W is the vertical load of the indenter, P is the vertical pressure exerted by the indenter, related to the load (orange-colored). F is the tangential force and τ the shear stress (red-colored). R is the total radius of the indenter; a is the radius at the critical load (when the indenter reached the metal substrate); h is the thickness of the layer.

The mathematical development of the formula is based upon the combination of geometrical parameters and the previously-mentioned forces, as discussed elsewhere [58]. The result is a formula that transforms the critical load into shear stress:

$$\tau = \frac{L_c}{\pi a \sqrt{R^2 - a^2}} \quad (27)$$

Where: W is the load, in N; a is the radius of the projected area, in m; P is the vertical load of indenter (Force/area), in Pa; R is the indenter radius, in m, L_c is the critical load, in N, and τ is the shear stress, in Pa

2.11.3 Estimation of Compressive Stresses via the Ollivier and Matthews Simplification

Although simplistic, the formulation of Ollivier and Matthews (O&M heretofore) has the implicit assumption that no intrinsic stresses are present in the layer. Consequently, if intrinsic stresses within the layer are dominating the delamination forces, the relationship underpredicts the frictional forces. If tensile stresses are dominating the delamination force, then O&M overpredicts the delamination force. However, far from being a drawback, this research proposed to utilize the O&M approximation to estimate the contribution of intrinsic stresses. Starting from Figure (7), the tangential force acting on the layer (in N) can be calculated as:

$$F_T = F_N \frac{a}{\sqrt{R^2 - a^2}} \quad (28)$$

Moreover, the friction coefficient can also be estimated as:

$$\mu = \frac{F_T}{F_N} = \frac{a}{\sqrt{R^2 - a^2}} \quad (29)$$

Equation (28) implies that the tangential force applied on the layer at the critical shear stress is solely a function of the normal force and the scratch track morphology. Regarding the coefficient of friction, caution is advised in the interpretation of Equation (29). Since the scratch test apparatus is designed to measure the lateral forces, the real coefficient of friction can only be determined in conditions where there is no plowing term (before the tip penetrates the layer).

In other words, the plowing term is assumed to cause the delamination and to be significantly higher than the friction forces. Therefore, the tangential forces are estimated from the scratch track geometrical measurements from microscopy, and the normal force

applied as per the right-hand-side of Equation (29). Then, the estimated tangential forces and the measured forces are compared. If compressive or tensile intrinsic stresses within the layer are significant in the forces associated with the delamination/detachment of the layer, the experimental tangential force and the estimated value will have a discrepancy. If the measured forces required to produce a failure are significantly higher than the estimated, compressive stresses are predominant in the layer since intrinsic compressive forces contribute to the resistance of the layer [38]. On the other hand, if the delamination forces are significantly lower than the O&M estimation, then tensile stresses are playing a role in the delamination of the layer.

2.11.4 Vickers Indentation Method

Another approach to determine the likelihood of detachment of a corrosion product layer/ scale is the determination of the fracture toughness (K) via Vickers nanoindentation [15], [16], [33], [65]. Fracture toughness is the mechanical property of a material that indicates how facile a crack can propagate in the substance[66]. Depending on the force that generates the crack propagation, the fracture toughness can be divided into three modes as shown in Figure 7.

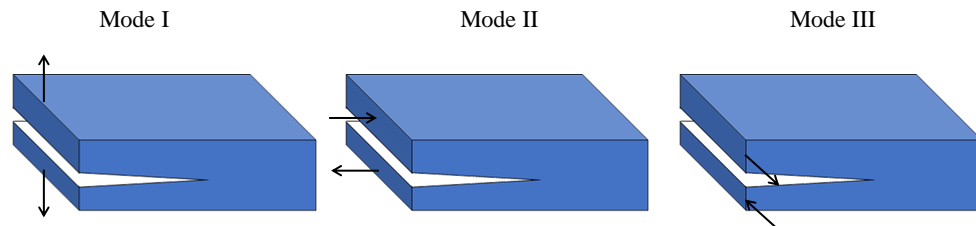


Figure 7. Types of applied force to generate crack propagation. Mode I corresponds to tensile forces normal to the crack, mode II corresponds to sliding forces (parallel to the crack). Mode III corresponds to the ‘tearing’ mode. The forces are parallel to the crack front. Adapted from [67]

For the case of brittle materials deposited on a flexible substrate, Mode I (K_{IC}) is the most commonly reported mode of failure [15], [16], [33], [65]. Given the similitudes, the crack propagation of corrosion product layers and scales is assumed to depend on the level of residual tensile stresses in the layer [68].

The fracture toughness in the layer can be estimated with the following semi-empirical relationship:

$$K_{IC} = \alpha \left(\frac{E}{H_V} \right)^m \left(\frac{F_N}{c^n} \right) \quad (30)$$

Where K_{IC} is the fracture toughness, in MPa m^{1/2}; α , m , n are constants of proportionality, E is the Young's modulus of the material, in Pa; H_V is the Vickers hardness of the material, in kg mm⁻², and c is the crack length as shown in Figure 8, in m, or μm , depending on the constant of proportionality.

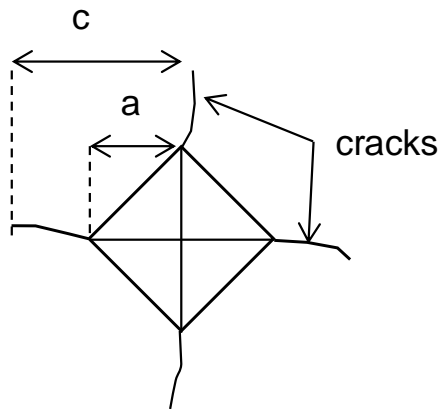


Figure 8. Vickers indentation mark on a brittle material. Cracks generated during the test are related to the fracture toughness. Adapted from [66]

In the case of corrosion product layers, many researchers have suggested values of α from 0.016 to 0.04, and values of 0.5 and 1.5 for m and n , respectively [15], [16], [33], [65].

Despite its simplicity, Vickers indentation fracture method has been criticized for requiring calibration constants [69]. Such constants require corroboration from other methods, such as chevron notch bar, double cantilever beam, and single-edge notched beam [48], [65]. However, those tests require specimens with a well-defined geometry, which result impractical for the purposes of studying corrosion product layers/scales. Therefore, the results Vickers indentation fracture method utilized in this thesis is for comparative purposes.

CHAPTER 3: RESEARCH OBJECTIVES AND HYPOTHESES

3.1 Objectives

This research is focused on accomplishing the following primary objectives:

- Apply microindentation, scratch testing, and atomic force microscopy (AFM), to assess the mechanical properties of thin polycrystalline layers [39], [41], [70], in order to determine the applicability of these techniques for the characterization of corrosion products on mild steel.
- Determine the relationship between substitutional atoms in a crystalline structure (specifically, calcium in an iron carbonate layer) and mechanical/adherence properties of the corrosion product layers.
- Establish whether there is a relationship between residual stresses and likelihood of spallation/buckling of corrosion product layers that grow under dewing conditions (iron carbonate and iron sulfide).

3.2 Hypotheses

As previously stated, the purpose of this research is to confirm that methodologies for mechanical characterization of thin films such as microhardness, scratching, and atomic force microscopy can be applied to the determination of corrosion product adherence and black powder formation. Consequently, the following hypotheses will be tested.

3.2.1 Intrinsic Stress Hypotheses:

- If the distribution of forces and internal stresses are influencing the adhesive and cohesive forces, then the delamination forces (cohesive and adhesive failure) of a

fully developed corrosion product layer will be higher than an inhomogeneous or a more porous corrosion product layer.

- The mechanical removal of iron sulfide on the steel substrate is governed by the cohesive failure between the inner and the outer layer of mackinawite. The mechanical shear stress to produce such failure is hypothesized to be in the order of magnitude of the shear stress produced in transportation pipelines.
- Substitutional calcium decreases the adhesive and cohesive properties of an iron carbonate layer. Therefore, the forces required for the cohesive and adhesive failure of a pure iron carbonate and a pure calcium carbonate layers are higher than for failure of iron carbonate layers with substitutional calcium.

3.2.2 *Extrinsic Stress Hypotheses:*

- The different coefficients of thermal expansion of the steel and the corrosion product layers generate stresses that produce buckling and spallation in corrosion product layers grown in dewing conditions. The spalled corrosion product layers are susceptible to removal due to the shear stress generated by the gas flow. Therefore, adhesive and cohesive failure plays a governing role in the formation of black powder.
- The critical shear stress to produce a cohesive failure of corrosion product layers grown in aqueous conditions is within the same order of magnitude of the shear stress generated by liquid flow and, therefore, cohesive failure plays a governing role on the partial detachment and generation of localized corrosion in aqueous environments and formation of black powder

The proposed experimental methodology was split into two steps: 1.- Obtain the mechanical properties of uniform corrosion product layers to validate the applied techniques and make comparisons with literature data; 2.- When a high level of confidence is attained, determine the mechanical properties of corrosion product layers generated in dewing conditions. The following chapters are dedicated to exploring the nature of the adherence and coherence forces of different corrosion product layers.

CHAPTER 4: MECHANICAL CHARACTERIZATION OF IRON CARBONATE LAYERS

4.1 Introduction

The first step to explore the adhesion of corrosion product layers is the mechanical characterization of corrosion product layers formed in aqueous conditions. The main objective of this chapter was to test the hypothesis related to the influence of internal stresses generated during the growth of the layer. Additionally, this chapter explored the potential application of different tribology science techniques to assess the mechanical integrity of corrosion product layers (namely a fully-developed and a discrete layer). The chapter is divided into two main parts: the first one corresponds to the mechanical assessment of iron carbonate formed in aqueous environments (both discrete and fully-developed) while the second one is focused in the mechanical characteristics of the iron carbonate formed under dewing conditions. At the end of the chapter, the mechanical integrity properties of iron carbonate formation in three environments were compared: a fully developed layer, a discrete layer formed in aqueous conditions and a discrete layer formed under dewing conditions.

4.1.1 Mechanical Assessment of Corrosion Product Layers (Iron Carbonate)

Some corrosion product layers formed under determined conditions can protect against corrosion [19]. However, the mechanical integrity of the layers can be compromised by factors such as flow, producing localized corrosion, as illustrated in

Figure 9 [15]. The mechanical strength of the layers is a critical parameter to prevent the partial removal of protective layers that might lead to localized corrosion as well as the formation of black powder [1], [15], [32], [71]

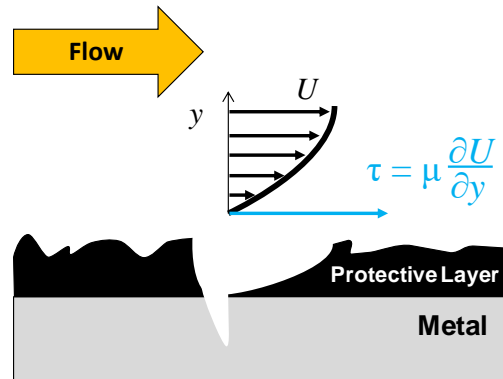


Figure 9. Localized corrosion produced by the flow. Adapted from Schmitt, *et al.*, [15]

In past research conducted on the forces required to remove iron carbonate product layers, Yang, *et al.*, utilized a moving stage to determine crystal removal forces from the metal surface. They reported values in the order of 10^7 Pa to remove the iron carbonate layer [32]. Xiong, *et al.*, reported similar values for the removal of a single crystal of iron carbonate with atomic force microscopy (AFM) [72].

4.2 Iron Carbonate Formed in Aqueous Environments

The goal of this step is to determine the adhesion forces between a layer and a substrate as well as to validate the use of some tribological techniques. The effort was made to develop two types of corrosion products under aqueous environments: a uniform protective layer of iron carbonate as described in other research [73], and a discrete layer of iron carbonate for further comparison with discrete layers formed under dewing

conditions. Such results were used to test the validation of the initial hypothesis that states that the mode of growing the iron carbonate influences its mechanical and adhesive characteristics. The conditions to develop an iron carbonate layer is described as follows.

4.2.1 Experimental Method

4.2.1.1 Test Matrix

Table 1 shows the experimental conditions to develop a uniform corrosion product layer.

Table 1

Experimental Conditions to Develop a Uniform Layer of Iron Carbonate (FeCO_3).

Parameter	Value
Temperature of solution / °C	80
Sparge gas	0.53 bar CO_2
Substrate material	API 5L X65 steel
Solution	1 wt.% NaCl, 50 ppm _w FeCl_2 (initial)
pH	8.0 ± 0.1 , 6.6 ± 0.1
Duration	3 days

The test apparatus is a three-electrode glass cell as shown in Figure 10. The characteristics of the API 5L X65 steel used for the experiments is given in Appendix A.

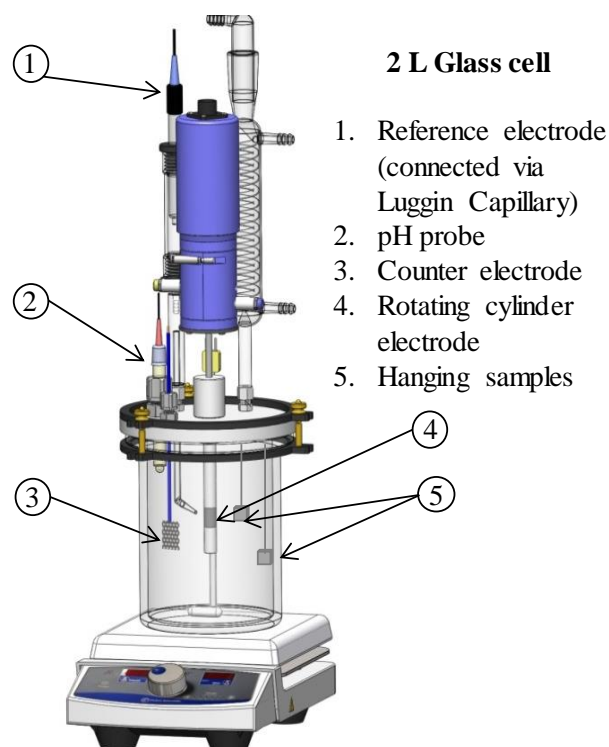


Figure 10. Three electrode glass cell apparatus.

4.2.1.2 Optical and Chemical Characterization of Corrosion Products

Scanning electron microscopy (SEM) and energy dispersive X-ray spectroscopy (EDS), in conjunction with X-ray diffraction, was used to determine the extent of steel coverage and composition of corrosion products. Other researchers have successfully applied these techniques to characterize corrosion product layers [13], [14], [74].

4.2.1.3 Mechanical Characterization of the Metal Substrate and the Corrosion Product

In order to follow the adhesion assessment proposed by Bull, *et al* [46] it is necessary to hypothesize the mode of failure of the layer starting from the hardness of the substrate and the layer. The relationship between both provided a qualitative assessment of the mode of failure. Nanoindentation at different loads with a Berkovich-type of indenter was used to determine the hardness of the layer. The hardness of the substrate

and the layer was measured with values within a 95% confidence interval with a sample of at least 10 nanoindentations at random places. The metallurgical characteristics and statistical analysis of the hardness of the substrate are provided in Appendix A and Appendix B, respectively.

4.2.1.4 Procedure to Determine the Adhesion Forces and Critical Shear Stress via AFM

AFM was used to determine the adhesion force of a single crystal with the methodology previously described by Xiong, *et al.*, as follows [75] and fully described in Appendix C:

1. Application of a low normal force for AFM imaging purposes.
2. When a crystal is found, the application of a high normal force for removing/scratching the grain.
3. Rescan with low normal force to determine if the crystal is removed.
4. If the crystal has not been removed, the normal force for removal is systematically increased until it is removed.

4.2.1.5 Procedure to Determine the Adhesion Forces and Critical Shear Stress via Scratch Testing

In order to determine the critical shear stress for iron carbonate removal, this research followed the methodology described by Bull, *et al.*[46]; therefore, the following steps were followed for the overall assessment of the adherence of an iron carbonate layer on the X65 steel:

1. Determine the hardness of the layer and the substrate to have a qualitative understanding of the mode of failure of the layer by using the qualitative failure map reported by Bull, *et al.*[46]
2. Based on the previous results, perform a progressive load scratch test to find the mode of failure of the layer on the substrate.
3. Estimate the critical load force from the progressive load scratch test. (Figure 11).

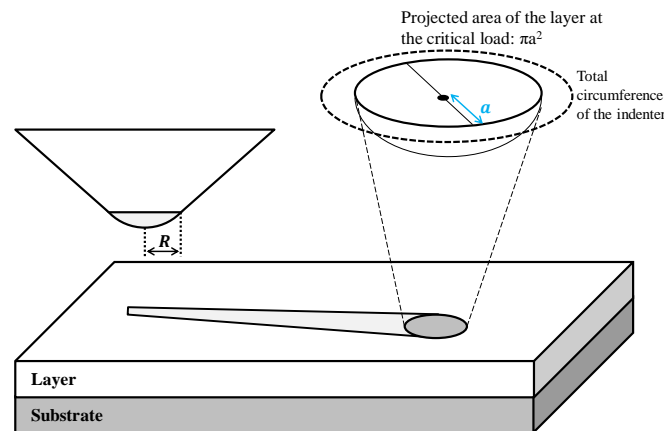


Figure 11. The principle of scratching to remove a layer (white) from a substrate (gray). The indenter cone has radius “R.” After the scratch, the projected area for the layer removal (πa^2) has a radius “a.” These geometrical parameters are used to calculate the critical shear stress [58].

4. By using the constant load scratch test, corroborate the previously estimated critical load.
5. Depending on the mode of failure, utilize the correct mathematical model to transform the critical load into the corresponding shear stress.

The steps are further discussed in the following sections.

4.2.2 Results and Discussion

4.2.2.1 Determination of the Substrate and Iron Carbonate Hardness

The hardness of the substrate and the iron carbonate layer were determined via nanoindentation. The results are summarized in Table 2.

Table 2

Summary of Hardness Measurements

Material	Hardness/GPa
X65 Steel	1.8 ± 0.21
Iron carbonate	0.35 ± 0.05

From the previous hardness values, and according to Ohring [76], the X65 steel can be considered a “medium hardness substrate” while the iron carbonate can be considered as a “hard film.” Therefore, the mode of failure can be estimated with the map failure mode proposed by Bull *et al.*[46]. Figure 12 depicts the hypothesized failure mode. If the x-axis is set at the middle of the scale, and the hardness in a high point, then the expected mode of failure for the iron carbonate precipitated onto X65 steel is buckling. It must be noted that this failure map is for qualitative purposes and thereby, this postulate will be corroborated with the constant load scratch test.

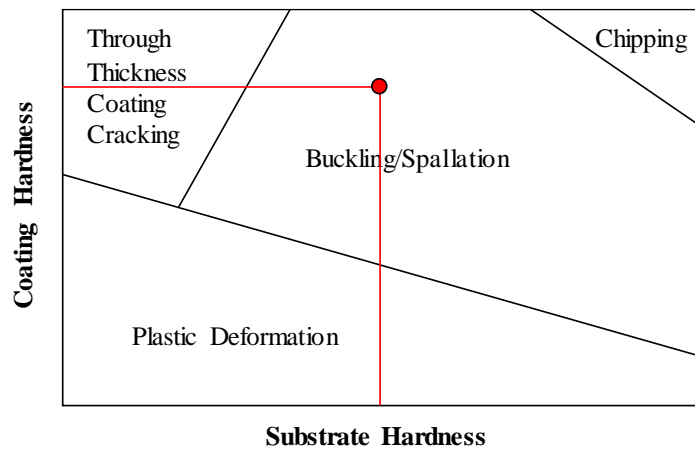


Figure 12. Failure map for iron carbonate precipitated on steel. Buckling is the most likely mode of failure for this system.

4.2.2.2 Microscopical Characterization of Iron Carbonate

Figure 13 shows an SEM image of the developed iron carbonate layer. The thickness and the chemical signature of iron carbonate were determined by cross-section analysis and EDS, respectively (Figure 14).

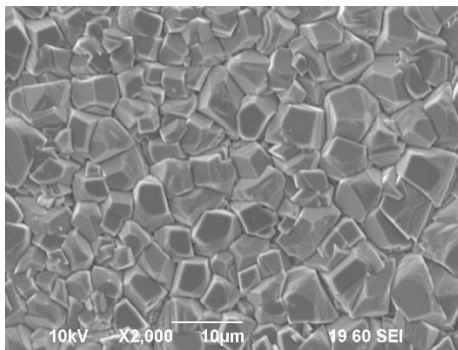


Figure 13. Iron carbonate layer formed.

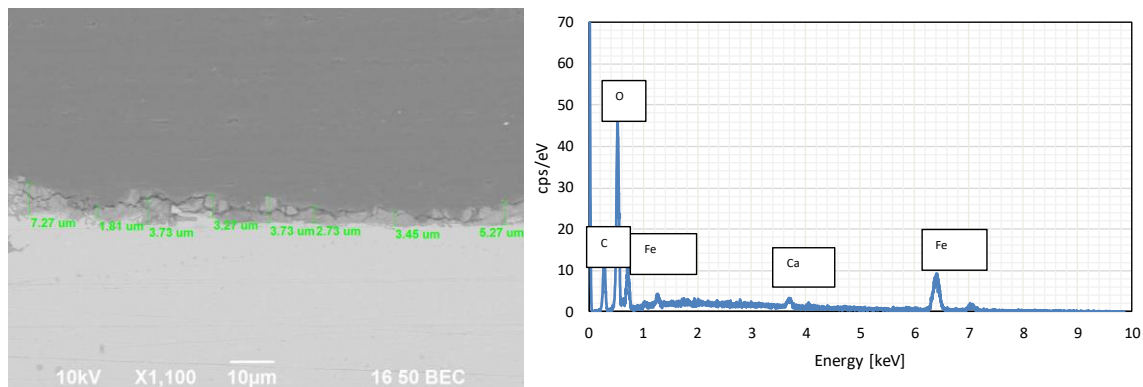


Figure 14. The cross-section area of the iron carbonate layer. EDS confirmed the formation of iron carbonate.

4.2.2.3 Determination of Adhesion Forces via Atomic Force Microscopy¹

The evaluated iron carbonate layer was formed using the experimental parameters shown in Table 6, yielding a scattered distribution of iron carbonate crystals on the steel surface as shown in Figure 15.

¹ Special acknowledgement to Dr. Alain Pailleret from Laboratoire Interfaces et Systèmes Electrochimiques, Université Pierre et Marie Curie, Paris, France. Experiments presented in this proposal must be credited to him. Dr. Zineb Belarbi (ICMT, Ohio University) is also thanked for assisting with AFM work. The contribution of the author of this thesis is specimen preparation and analysis of the data obtained from the experiments.

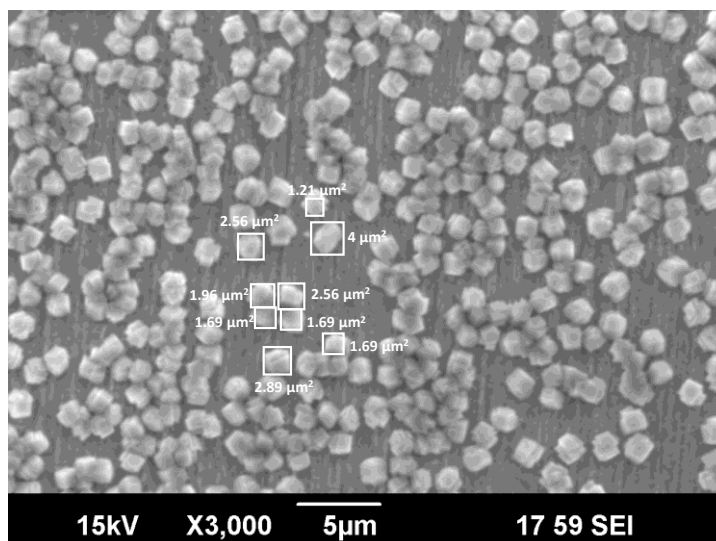


Figure 15. Scattered iron carbonate crystals on steel (conditions listed in Table 1). Areas of select crystals marked; the lowest and highest values measured are 1.21 and $4 \mu\text{m}^2$; average crystal area: $2.25 \pm 0.85 \mu\text{m}^2$.

The average and the standard deviation for crystal size and the surface area occupied were $1.48 \pm 0.27 \mu\text{m}$ and $2.25 \pm 0.85 \mu\text{m}^2$, respectively. Once the iron carbonate layer was obtained, the methodology previously described to remove a single crystal was followed. Figure 16 depicts the crystal removal process by AFM topographic imaging. The light zones correspond to iron carbonate crystals. In step a) a zone with a single crystal was imaged, b) depicts the image obtained when a high normal force is used in lateral force mode, and c) shows the zone after the crystal was removed.

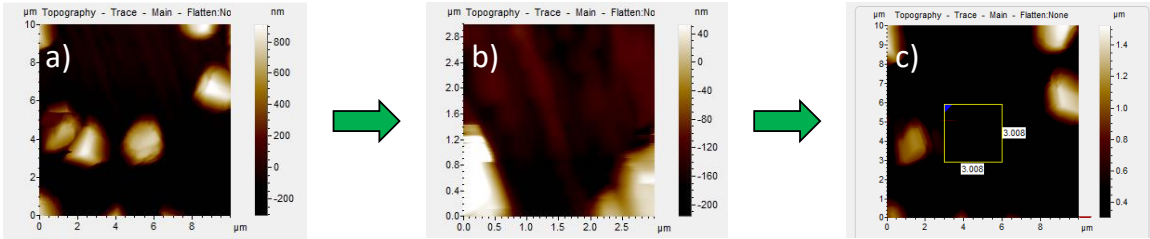


Figure 16. Removal process for a single crystal of iron carbonate by AFM: a) zone with single crystals; b) image obtained when a high normal force is applied; c) zone after crystal removal.

The topography of the scratch zone can be seen in Figure 17 .in the form of voltage. The image indicates the presence of a single crystal due to the dimensions recorded. In the case of a single crystal, the voltage peak was set to *ca.* 8 V. Using Equation (31), this voltage is converted to normal force applied by the AFM tip [77], [78]:

$$F = k\alpha V \quad (31)$$

Where: F is the normal force in N, k is the AFM cantilever vertical tip spring constant in N/m, α is the deflection sensitivity in m/V, and V is the measured voltage.

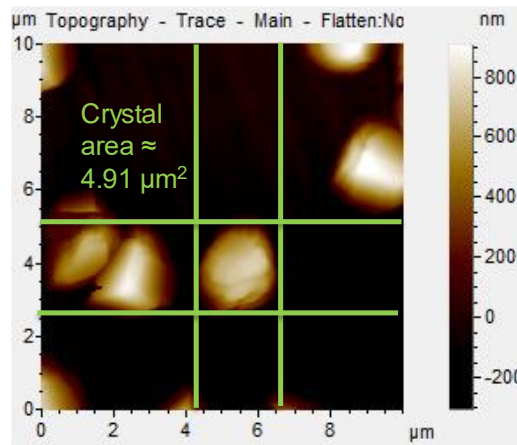


Figure 17. Topography image of the trace force corresponding to the forward movement of the AFM tip (trace).

The voltage is then converted into a penetration force of 52 μN . The scratch area (assuming a circular geometry) obtained from topography mapping (Figure 17) is 4.91 μm^2 . Following the methodology thoroughly explained in Appendix C, the lateral current-displacement curve (friction loop [79]) is obtained from the lateral force microscopy and is shown in Figure 18. The curve showed that the ideal friction loop suggested by Schwarz, *et al.* [79] is not fully attained. The process of the lateral force scanning and the interpretation of the curve behavior are explained in Figure 18. This behavior can be attributed to the low torsion produced on the probe cantilever when the AFM tip scans the iron (horizontal parts of the graphs) and the high torsion produced when the AFM tip scans the iron carbonate crystal (the substantial change in slope). The differences between the start and end of the trace and retrace scan on the crystal (*i.e.*, the start of step 2 does not match with the end of step 5 and *vice versa* in Figure 18) are attributed to the electronic controller (PID) of the AFM apparatus, which was set to have a lower gain than the value recommended by the instruction manual in order to ensure that the tip is maintained at the substrate level during the measurements. The low gain produced a lag between the voltage sensed by the tip and the voltage recorded by the software for data acquisition.

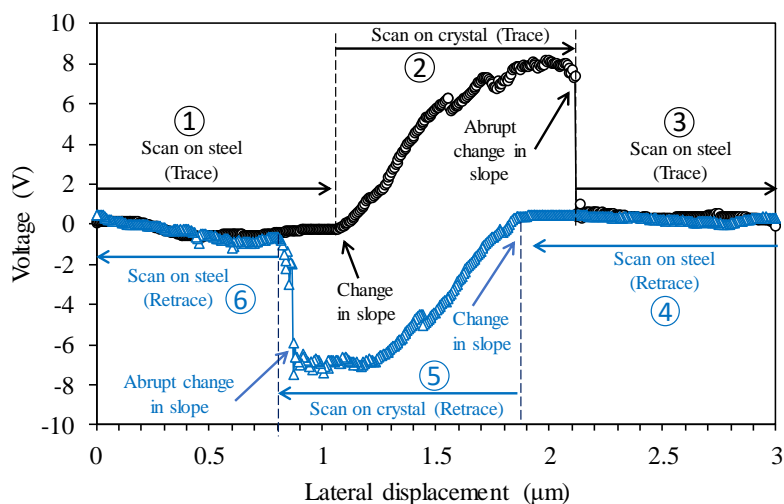


Figure 18. Lateral force microscopy scan process. Horizontal arrows indicate the direction of the scan. 1) The AFM probe scans the steel in the trace movement. 2) A sudden change in the slope indicated a high torsion of the tip. It is assumed that the tip has reached the crystal. 3) An abrupt change in slope shown that the tip was scanning the steel surface again. 4) The retrace scan started on the steel surface. 5) The crystal was reached when a sudden change in slope was recorded. 6) The abrupt change in slope indicated that the steel surface was reached again by the tip.

Finally, the variation of voltage was obtained from different friction loops measured at different stages of the scratched area as shown in Figure 19. By using the average of the absolute values of the voltage as suggested by Schwarz, *et al.* [79], the lateral forces shown in Figure 19 were calculated using the methodology given in Appendix C. The average of the lateral forces was used to calculate shear stress to produce the removal of a single crystal of iron carbonate by dividing the average lateral force by the area of the scratched crystal. Thereby, the resulting shear stress is 43 ± 18 MPa, which is significantly higher than the values reported by Xiong, *et al.*, [75] who reported a value of 11.2 ± 6 MPa for single crystal removal of iron carbonate. The results obtained are summarized in Table 3.

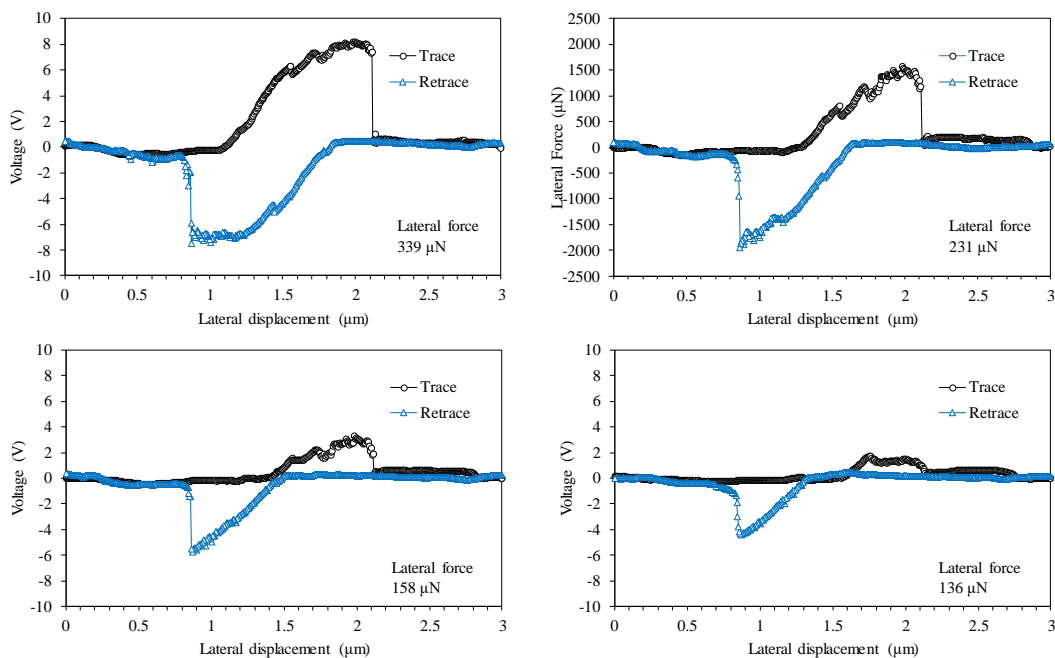


Figure 19. Friction loops at different stages of the AFM scratch test. Black circular markers represent the trace, and blue triangular markers represent the retrace. Lateral forces calculated, as shown in Appendix C.

Table 3

Summary of Measurements

Parameter	Value
Area of the single crystal scratched (μm^2)	4.91
Removal normal force of single crystal (μN)	52
Removal lateral force of single crystal (μN)	216 ± 91
Removal shear stress of single crystal (MPa)	43 ± 18

The differences in stress values between those reported by Xiong, *et al.*, [75] and the research reported herein can potentially be attributed to inconsistencies in the calculations of the lateral spring constant was calculated using the methodology proposed by Liu, *et al.* [80]. In Xiong's work, the tip height (denoted as "t" in Figure 20) was not correctly measured according to the aforementioned methodology.

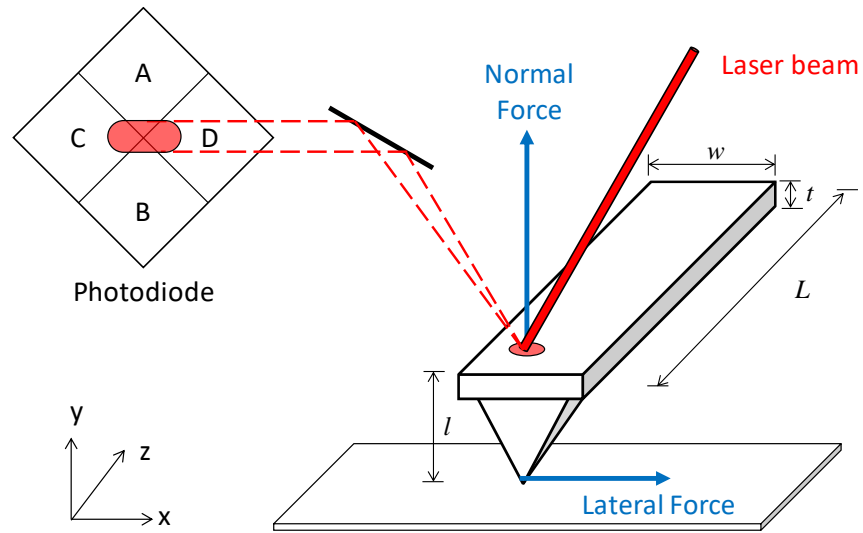


Figure 20. Schematic illustration of the geometric parameters required for the lateral spring constant calibration. In the figure: t is the height from the point of the tip to the bottom part of the cantilever. Adapted from [80].

As Figure 21 shows, the height of the tip was measured including the thickness of the cantilever, while Figure 20 indicates that the thickness of the cantilever is not included in the height of the tip. The argument that the height of the tip must be measured excluding the cantilever thickness is also supported by other researches [81]–[83]. By reperforming the calculations for the lateral spring constant as proposed by Liu, *et al.* [80] (the methodology followed by Xiong *et al.* [75]), the lateral spring constant increased from 980 N/m (value reported [75]) to 1700 N/m (a factor of 1.7). As shown by the Equation (38) in Appendix C, the lateral force is directly proportional to the lateral spring constant. Thus, the calculations of the reported lateral force, as well as the shear stress, must be increased by a factor of 1.7. After being increased, the value of shear stress to produce the removal of a single crystal of iron carbonate changes from 11 to 19

± 10 MPa. The corrected values and the values obtained in this research effort are well within the same order of magnitude.

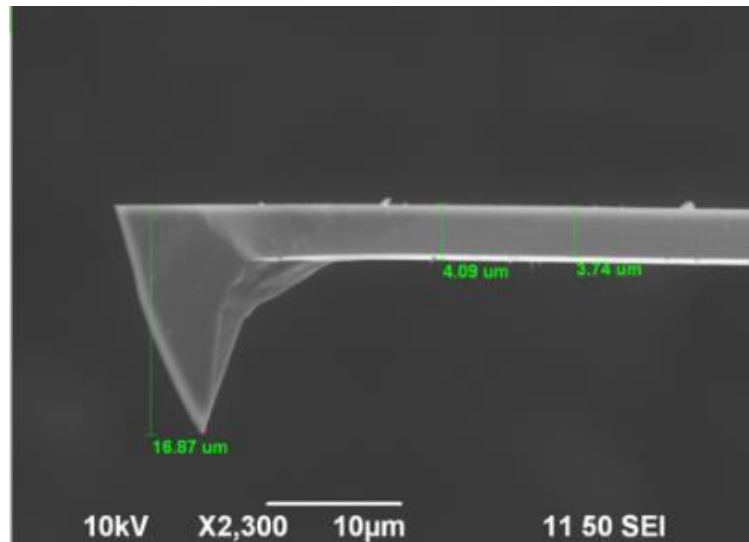


Figure 21. Tip measurements reported by Xiong *et al.* [75]. The tip height was measured including the thickness of the cantilever. Such a difference can impact the shear stress calculations by a factor of 1.7.

The methodology to remove a single crystal of iron carbonate was followed for a compact layer of iron carbonate. Such a layer was developed using the conditions given in Table 1 (solution pH 8.0). A compact iron carbonate layer was formed, as can be seen in Figure 22.

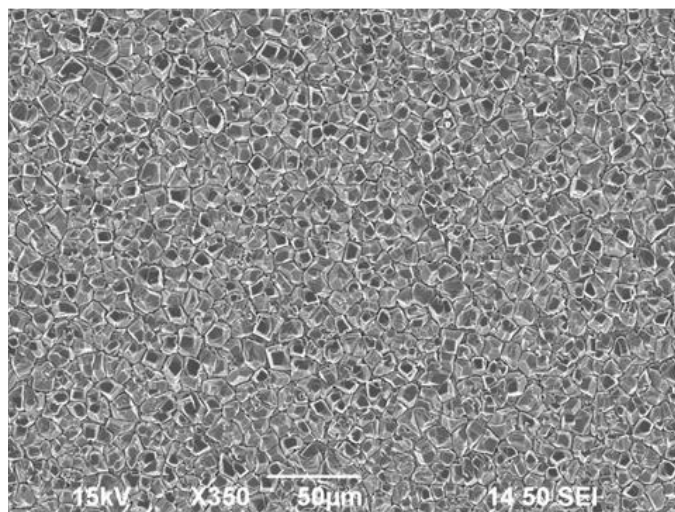


Figure 22. SEM image of a compact iron carbonate layer (3 days, pH 8 ± 0.1 , $80\text{ }^\circ\text{C}$, initial $[\text{Fe}^{2+}] = 50\text{ ppm}$, stagnant conditions).

However, when the AFM scratch test was performed, many difficulties arose. At the maximum capacity of the apparatus, the penetration of the tip was about $0.25\text{ }\mu\text{m}$, which is likely insufficient to reach the steel substrate (Figure 23).

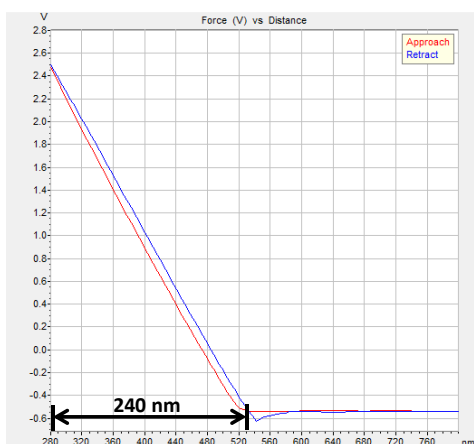


Figure 23. Penetration depth of the AFM tip. Reading from right to left: a change in force (V) indicates the distance (nm) at which the sample was reached by the tip (moving downwards). An increase in the force indicates that the tip is applying more force to move further. The double-headed arrow indicates the penetration distance into the iron carbonate layer.

Besides, the tip broke during the process as shown in Figure 24. The fact that the AFM tip broke during the test can be explained by an increase in the normal force or an increase in the lateral force of the iron carbonate layer concerning a single crystal. These two possible explanations were further explored using microindentation and micro scratch techniques.

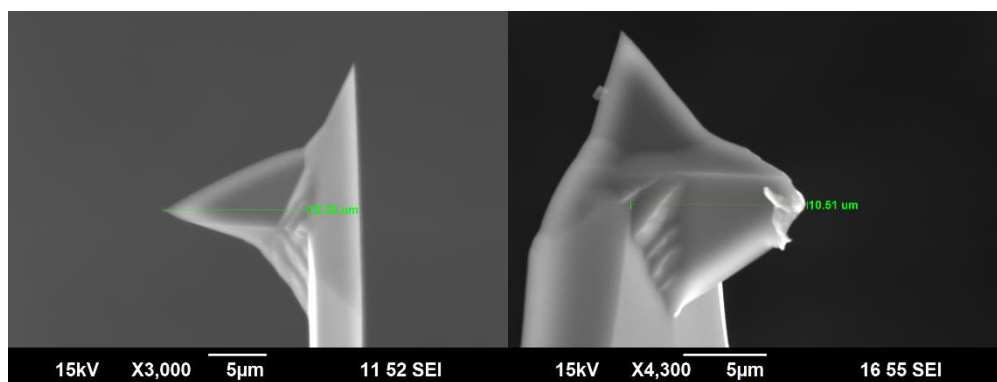


Figure 24. SEM image of AFM tip before the test (left) and after scratching the compact iron carbonate layer, the tip was broken (right).

As the lateral force microscopy was insufficient to assess the mechanical integrity of an iron carbonate layer formed under aqueous conditions (fully developed) the next step was to utilize the scratch test to determine the adhesion forces.

4.2.2.4 Determination of Adhesion Forces via Progressive Load Scratch Test

A progressive load scratch test was performed as per parameters listed in Table 4.

Figure 25 shows the result of the test.

Table 4

Parameters for Progressive Load Scratch Test on Iron Carbonate (FeCO_3)

Parameter	Value
Type of load	Progressive
Initial load (N)	0.01
Final load (N)	0.8
Loading rate (N/min)	1.6
Scratch length (mm)	3
Scratching speed (mm/min)	3
Indenter geometry	120° Cone



Figure 25. Progressive scratch test from 0.1 to 800 mN.

The analysis started by determining the minimum force to produce noticeable damage to the iron carbonate layer at approximately 35 mN, as shown in Figure 26 a). As the load increased, more damage was noticed in the layer, until the detachment of the iron carbonate layer was observed at a load range of 405 ± 15 mN.

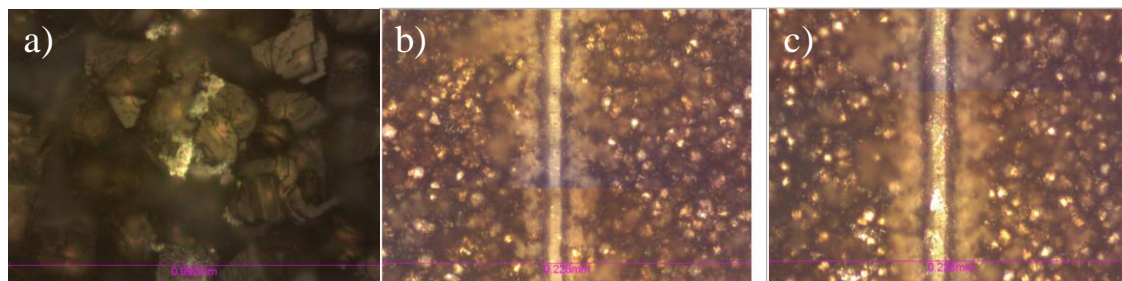


Figure 26. Progressive scratch test results from Figure 25: a) Minimum damage detected force: 35 ± 5 mN; b) Damage of the layer with no detachment (approximately 365 mN); c) removal of the iron carbonate layer at a force of 405 ± 15 mN.

Constant load scratch tests around 400 mN of load were performed to corroborate this finding (force for detaching the iron carbonate layer).

4.2.2.5 Constant Low-Load Scratch Test

Constant load scratch tests were performed to corroborate that at low loads there was no detachment of the iron carbonate layer. Figure 27 shows the constant load test images for 10 and 30 mN.

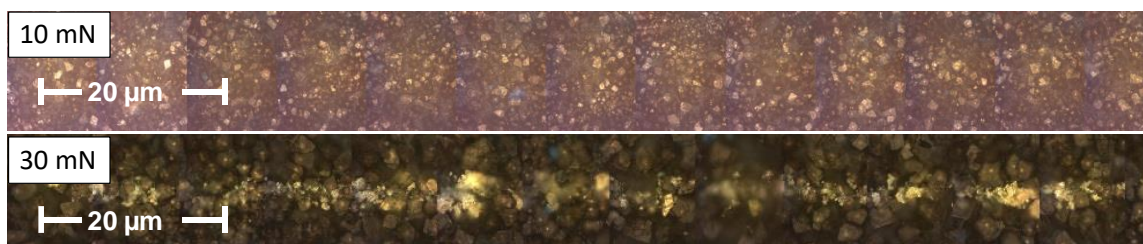


Figure 27. Constant load scratch test at low penetration forces.

It is noteworthy that there is no detachment of the layer at these loads, only superficial damages at 30 mN. Moreover, SEM images corroborated this finding, as shown in Figure 28.

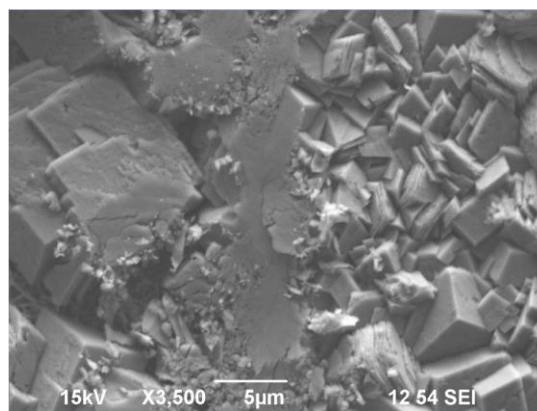


Figure 28. Constant load scratch test at 30 mN. There is superficial damage, but no detachment of the iron carbonate layer.

4.2.2.6 Constant High-Load Scratch Test

Constant load forces at 400, 390, 380 and 370 mN were used to perform the constant load tests. Figure 29 shows the profilometry data for the test specimen.

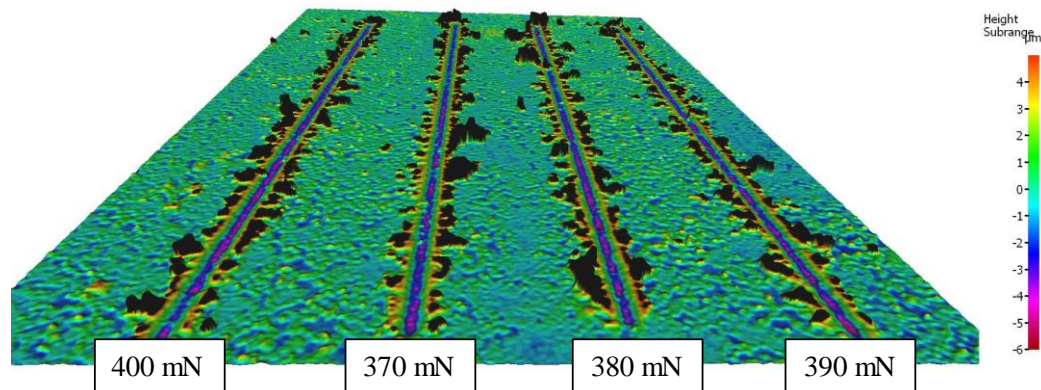


Figure 29. Profilometry data for different constant load scratch tests.

Figure 30 shows the depth analysis of the scratch tracks left by the test.

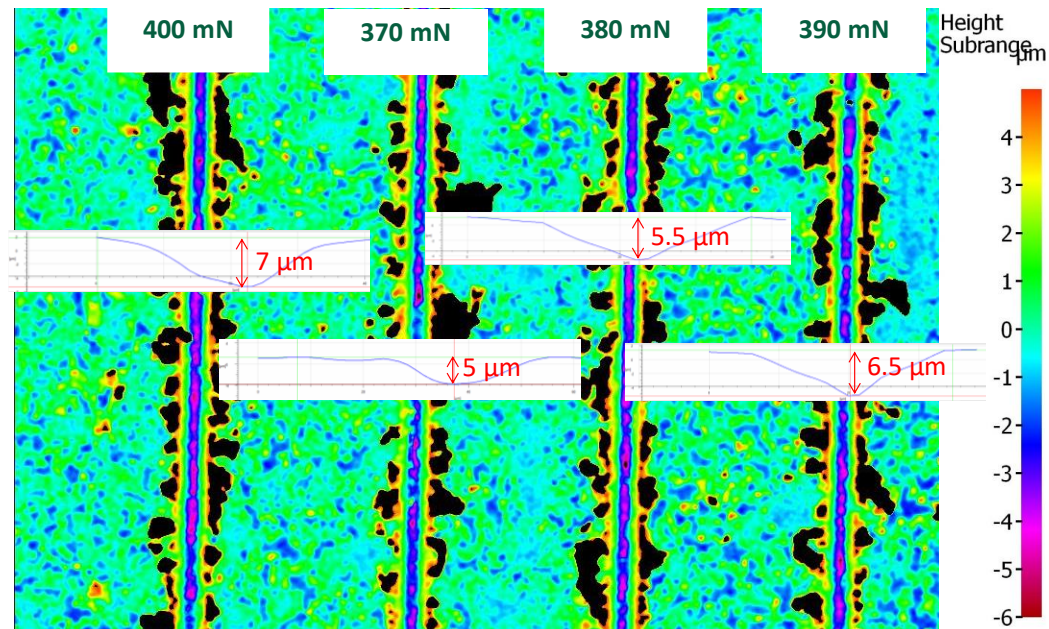


Figure 30. Depth analysis for different constant load scratch tests.

The thickness of the layer was of the order of 5 µm. However, the mark left by the load at 390 mN showed a deeper track than this value (a depth of 6.5 µm). This can be interpreted as the minimum force to completely penetrate the iron carbonate layer. However, the depth of the scratch being significantly larger than the average thickness of the layer is not conclusive evidence of iron carbonate detachment, since the possibility of plastic deformation of the layer and the substrate can be present. Therefore, EDS was used as a complementary technique to assess such a detachment.

4.2.2.7 EDS Analysis of Scratch Tests

The corroboration of the previous postulate was done by a progressive load scratch test (from a load of 0.1 to 800 mN) and microscopy. Figure 31 shows the mode of failure at the critical load. Buckling was detected *via* microscopy (optical and SEM). Given the mode of failure of the layer, the adhesive properties can be estimated by the

model proposed by Olivier & Matthews [58]. Such a model assumes that the scratch test is performed quasi-statically (very slow in order to avoid high values of friction). For now, attention will be focused on the determination of the critical load (an important parameter for the shear stress determination) *via* microscopy and EDS analysis.

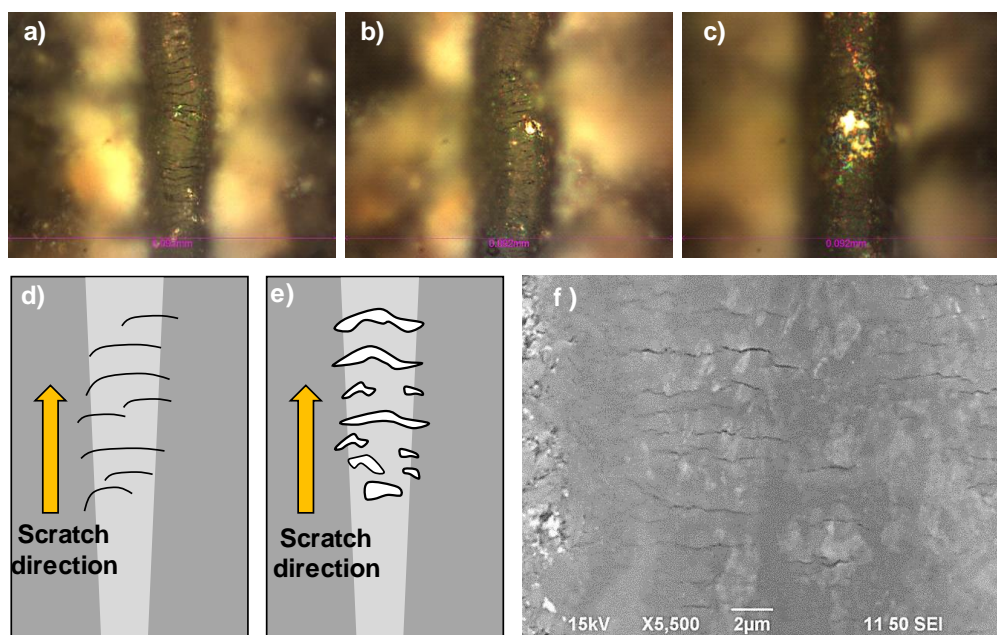


Figure 31. Buckling detection in the iron carbonate layer around the point of failure: a) optical microscope image before the failure; b) and c) failure point; d) and e) standard mapping for buckling failure [46], [84]; f) buckling images of the iron carbonate layer with SEM.

In order to find the detachment force of the iron carbonate layer, EDS was utilized to establish the local chemical composition within the scratch tracks. If the chemical signature shows a presence of Fe, C, and O, then this would be a sign that the iron carbonate layer has not been fully removed. On the other hand, if the chemical

composition shows a high content of iron (and minimal oxygen/carbon), then it can be assumed that the iron carbonate layer has been completely removed.

Three different loads were used to corroborate the detachment of the iron carbonate layer *via* the EDS analysis. Figure 32 and Figure 33 show the three tests performed and the resulting scratch tracks. Results from optical microscopy suggest that the iron carbonate layer is partially removed at 250 mN and totally removed at 390 mN.

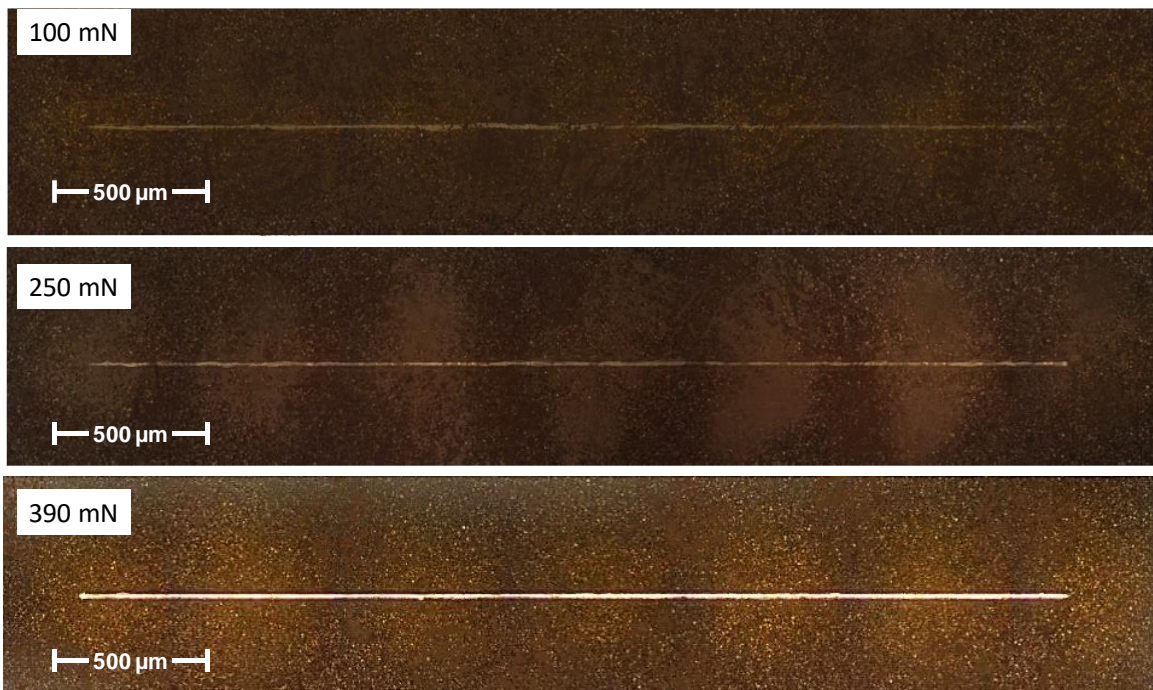


Figure 32. Constant load scratch tests at different forces.

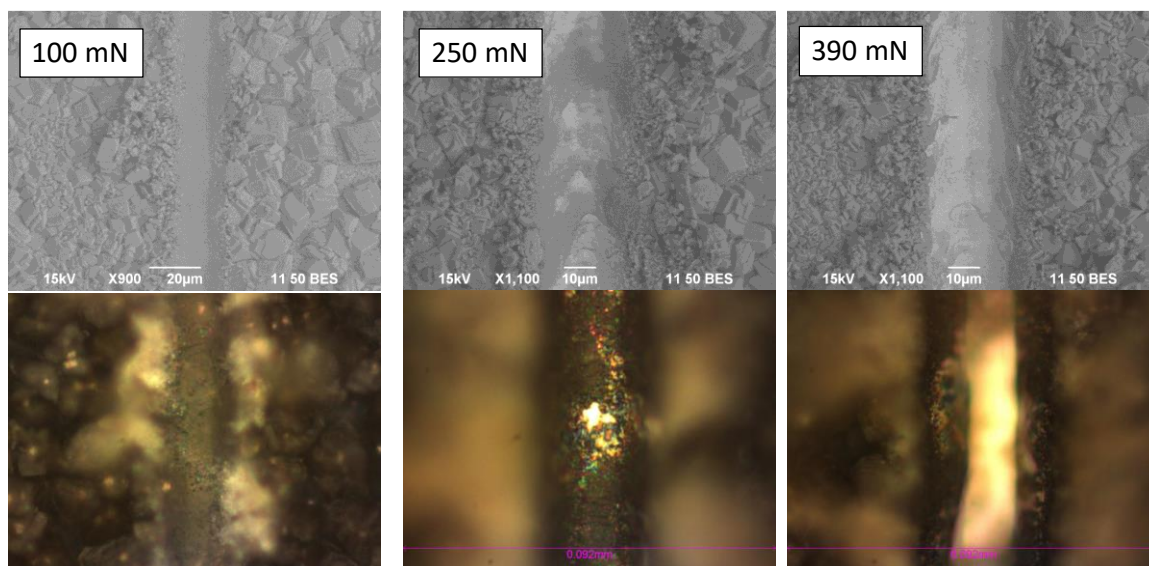


Figure 33. Zoomed images of constant load scratch tests at different forces.

The scratch tracks were then analyzed with EDS as shown in Figure 34. In the scratch test performed at a constant load of 100 mN, the local chemistry of the mark was very similar to its surroundings. This unchanged local chemistry indicated that the iron carbonate layer had not been removed. When the force was increased to 250 mN, there was partial removal of the layer as indicated by the pink pattern (representing the presence of iron). Finally, at 390 mN, the iron carbonate was totally removed as corroborated by the pink pattern in the mark of the scratch (representing the chemical signature of iron), which unequivocally proved that the steel surface was exposed.



Figure 34. EDS mapping analysis of constant load scratch tests at different forces.

Figure 35 shows the atomic mapping analysis for carbon, oxygen, and iron in the grooves. Again, the chemical signatures are consistent with the previous claim of total removal of iron carbonate at 390 mN of load force in the scratch test.

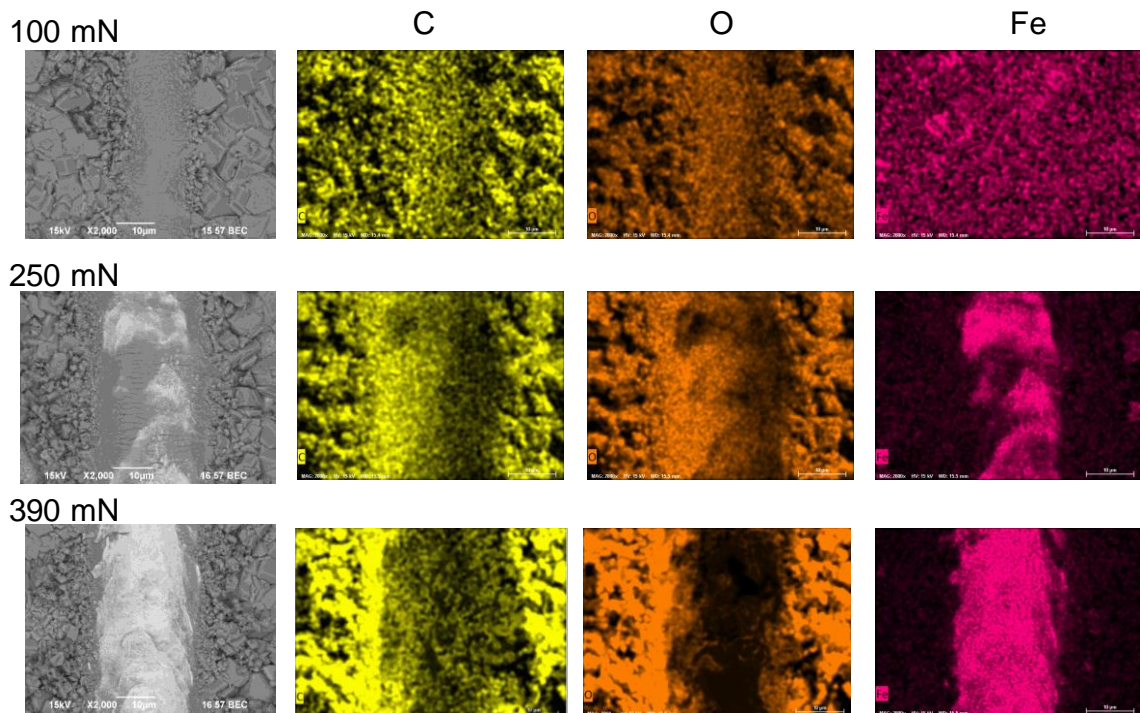


Figure 35. EDS analysis for constant load scratch tests at different forces.

4.2.2.8 Shear Stress Determination

Since evidence indicated that the model of failure was buckling, it was presumably originated by compressive stresses. Equation (25) was then utilized to calculate the shear stress in function of the experimental lateral force.

The lateral force was recorded during scratch tests as a first step to estimate the associated shear stress. The next step was to determine and compare the shear stress as a

function of both frictional forces: experimental and calculated. Figure 36 shows a comparison of the results from Equation (25) and Equation (27).

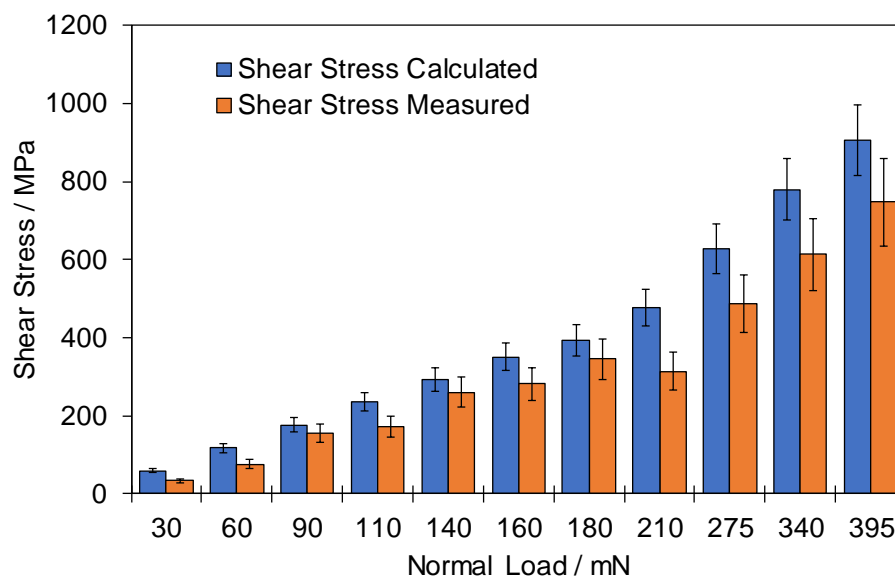


Figure 36. Comparison of calculated shear stresses at selected normal load forces for scratch tests. Blue bars: shear stress calculated by the Ollivier and Matthews formula, per Equation (27). Orange bars: shear stress calculated from experimental frictional forces per Equation (25). Error bars: standard deviation calculated from 5 individual experiments. Critical load determined at 390 mN.

Finally, critical forces for cohesively and adhesively damaged iron carbonate layers were determined. Table 5 shows a summary of the critical loads and shear stresses involved. The values reported in the table correspond to the values obtained *via* Equation (25).

Table 5

Summary of Critical Loads and Shear Stresses

Parameter	Load / mN	Shear Stress/ MPa
Minimum force to create noticeable damage (cohesive failure)	36	135 ± 5
Load to partially remove the layer (adhesive failure critical load)	250	396 ± 8
Load t		
Load to totally remove the layer	390	630 ± 15

Results were compared with data available in the open literature for the removal of iron carbonate layers from a steel substrate [32], [71]. The comparison is given in Figure 37 which shows that the values obtained in this study are one order of magnitude higher than those obtained from the literature. One possible explanation for the disagreement can be the formation conditions of the layers: in the other studies, the mechanical integrity of an iron carbonate layer formed in a bulk pH of 6.6 was assessed. Consequently, different bulk chemical conditions might lead to different adherence forces of the layers. Therefore, at lower pH (*i.e.* 4-6) the unprotective nature of the corrosion product layers can be attributed to potentially low adhesion forces. However, as it relates to applications within the oil and gas industry where shear stresses generated by a fluid flow are of the order of hundreds or thousands of Pa, the mechanical integrity of iron carbonate layer formed at high bulk pH cannot be easily challenged.

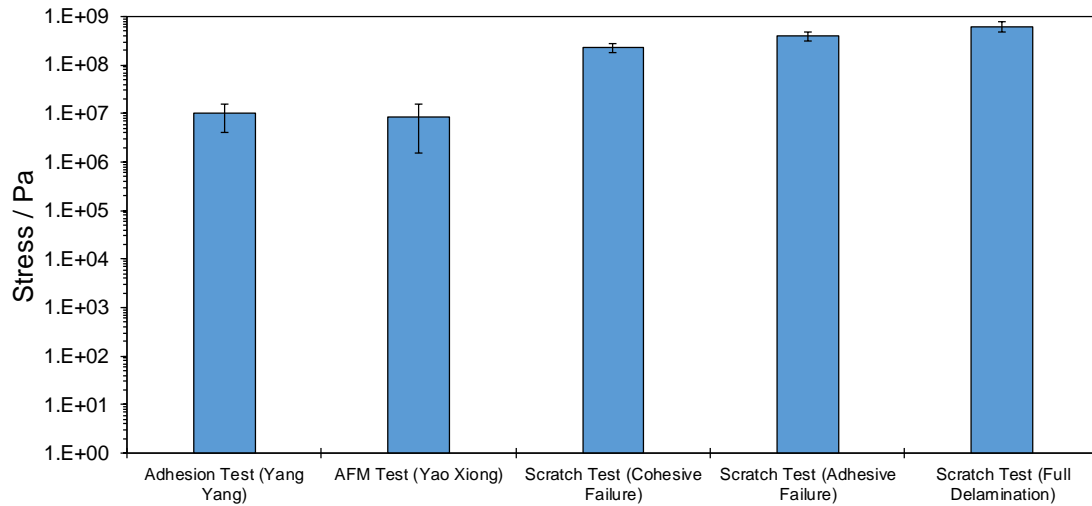


Figure 37. Comparison of shear stresses obtained by different techniques [32], [71]. The estimated shear stress to produce cohesive and adhesive failure is of the order of 10^8 Pa.

4.2.2.9 Determination of Intrinsic Stresses

As a way to estimate the contribution of internal stresses to the mechanical integrity of the layer, the Ollivier and Matthews approach was utilized to calculate the shear stress as a function of the normal force.

Figure 38 shows the experimental lateral force and the coefficient of friction recorded during a progressive load scratch test, and the estimated tangential force and the coefficient of friction at selected normal forces. Such estimations were computed with Equation (28) and Equation (29).

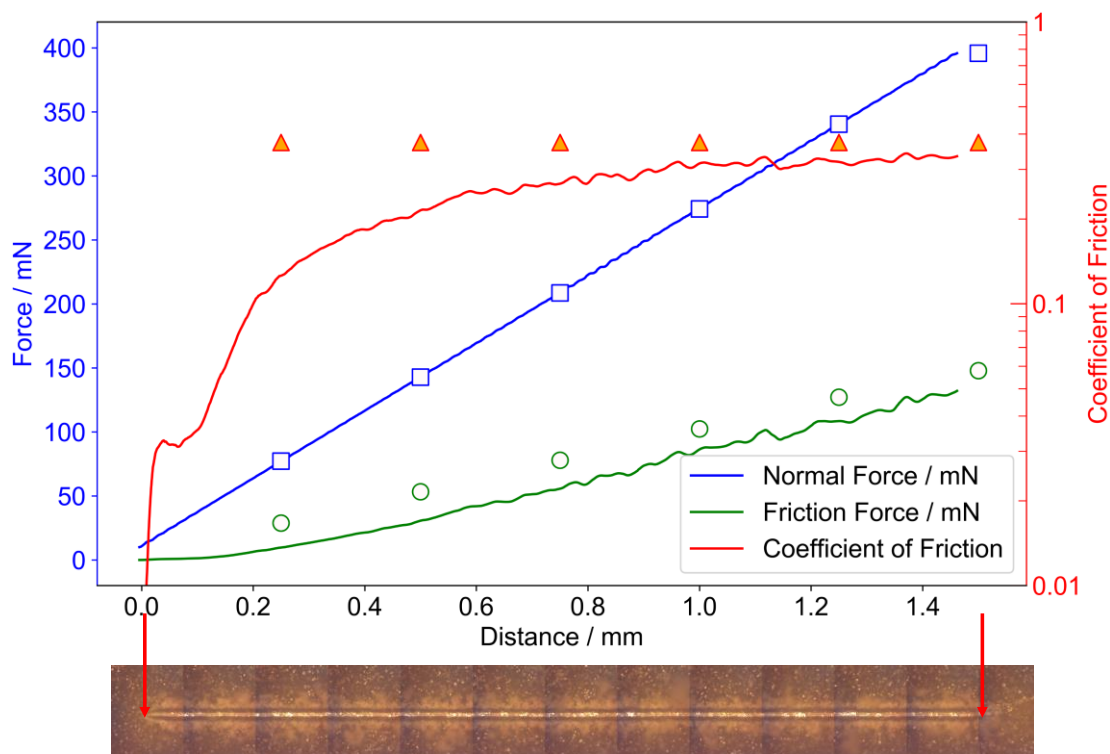


Figure 38. Progressive load scratch test of the iron carbonate in aqueous environments. Solid lines: experimental values. Markers: calculated values by the Olliver and Matthews formulae -as per Equation (28) and Equation (29)- as a function of selected normal forces.

A good agreement between the Ollivier and Matthews formulae and the experimental values was attained. Therefore, intrinsic stresses associated with the formation of iron carbonate do not significantly contribute to the mechanical integrity of the layer.

The same procedure was done for the cohesive, adhesive and full delamination failures to compare the calculated and measured friction forces at those points. Figure 39 shows that there is no significant difference between the measured and the experimental values for the fully-developed iron carbonate layer. These results suggest that the level of

intrinsic stresses within the layer are negligible in terms of the contribution to the failure of the layer.

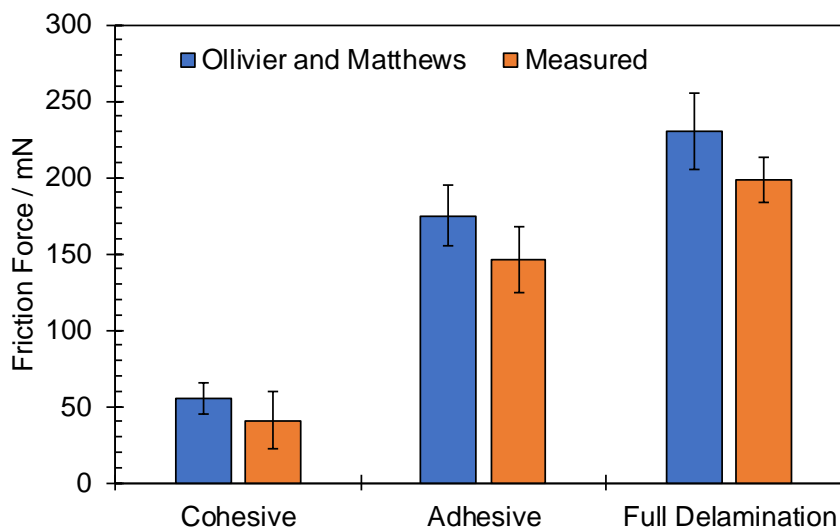


Figure 39. Comparison of the tangential forces obtained at cohesive, adhesive and full delamination with the Ollivier and Matthews approach per Equation (28) and measured experimentally.

The fact that the experimental and calculated tangential forces were similar, even for the full delamination test, implies that the possible epitaxial stresses at the interface between the iron carbonate layer and the steel are negligible. Consequently, the substrate must also obey the O&M estimation if there are no stresses on the surface. This postulate was corroborated by running a progressive load scratch test on bare steel at the same conditions as for the iron carbonate. Figure 40 shows the comparison between the steel and the iron carbonate layer. It is observed that the frictional force and the coefficient of friction are similar.

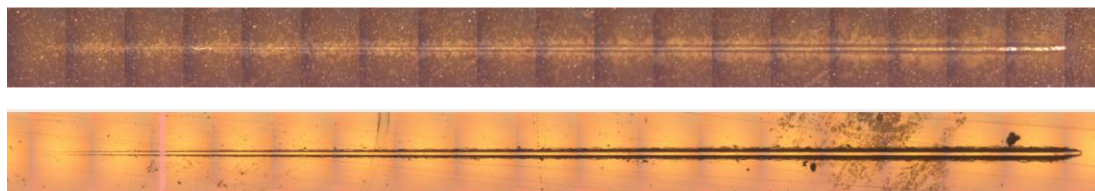
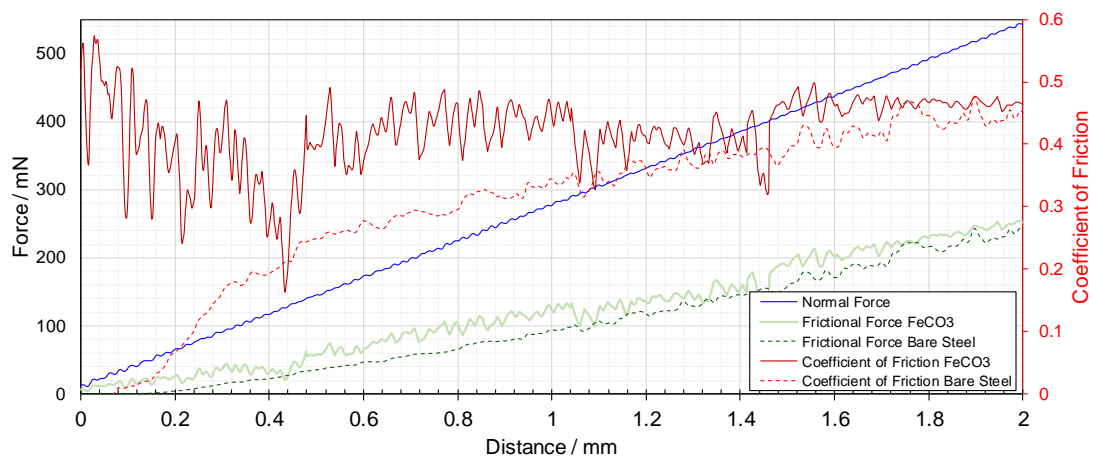


Figure 40. Comparison of a progressive load test on bare X65 steel and on a FeCO_3 layer.

These results suggest that, in the case of bare X65 steel and iron carbonate layers, the friction force is a direct function of the normal force applied, independent from the substrate.

4.2.2.10 Vickers Indentation Fracture Tests

Figure 41 shows the mark left by the Vickers indenter during the test. Fracture toughness was estimated by using Equation (30). The value was $1.7 \pm 0.1 \text{ MPa m}^{-1/2}$. This value is in good agreement with Gao, *et al.*[65] that reported the fracture toughness of $1.5 \pm 0.25 \text{ MPa m}^{-1/2}$ for iron carbonate as a product of CO_2 corrosion

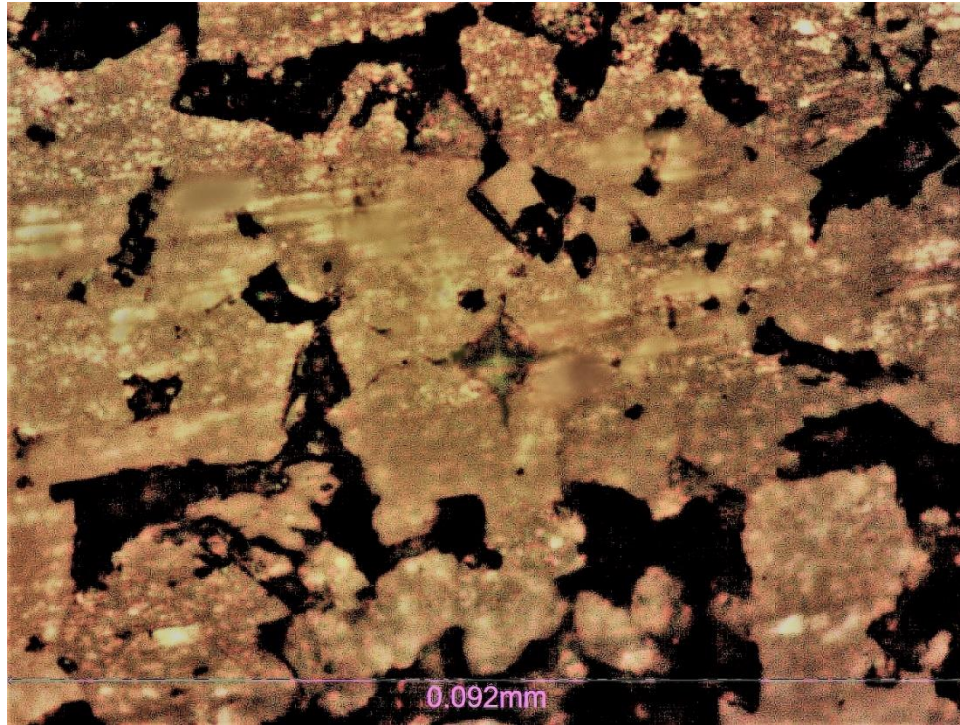


Figure 41. Vickers hardness mark and crack propagation on iron carbonate.

4.3 Iron Carbonate in Dewing Conditions

4.3.1 *Experimental Method*

This section mainly discusses how the corrosion product layers are obtained in dewing conditions. The mechanical characterization methodology was previously discussed in section 4.2.1.5.

4.3.1.1 *Test Matrices*

In order to obtain corrosion products similarly to how they are formed associated with dewing in field conditions [1], [5], experiments were conducted at test conditions as outlined in Table 6. Since it was not possible to measure the pH *in situ*, an in-house software package, MULTICORP™, was used to calculate the pH in condensed water.

Table 6

Experimental Conditions to Develop Iron Carbonate (FeCO_3) and Mackinawite (FeS) Corrosion Products.

Parameter	Value
Gas temperature / °C	75
Temperature of solution / °C	60
Sparge gas	0.62 bar CO_2 / 100 ppm _v H_2S
Substrate material	API 5L X65 Steel
Solution	Deionized (DI) water
Condensed water calculated pH	4.13
Temperature of steel / °C	25
Duration	3 days

The gas and solution temperature were chosen based upon the scaling tendency of iron carbonate. Previous work has shown that such conditions result in the formation of an iron carbonate layer [85], X-ray diffraction (XRD) was used to corroborate its formation. The test apparatus is a glass cell setup, with a Peltier thermoelectric system utilized to control the temperature of the steel through a PID controller as developed by Colahan, *et al.* [85]. A layout of the glass cell is shown in Figure 42.

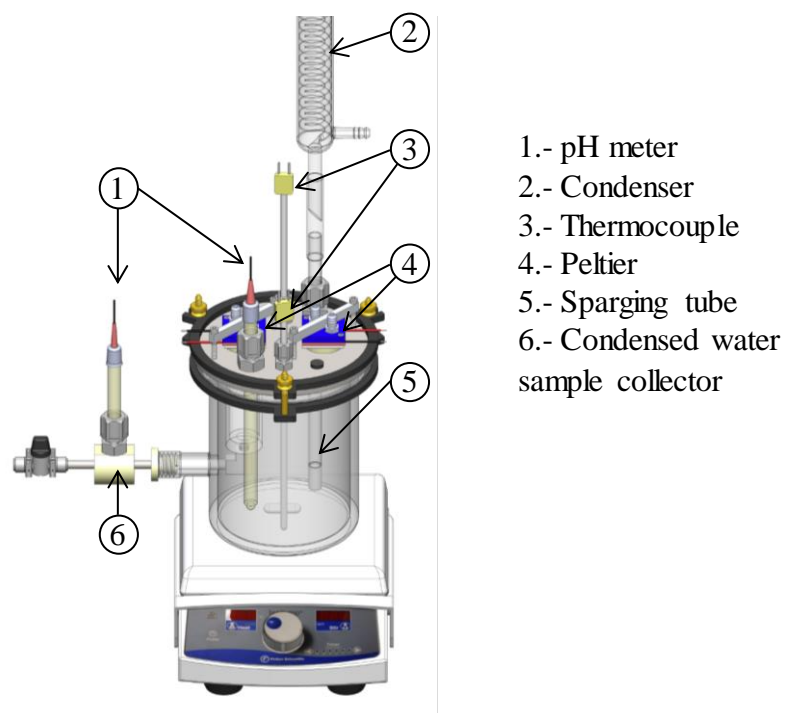


Figure 42. Glass cell apparatus to obtain corrosion product layers under dewing conditions.

4.3.2 Results and Discussion

Even though in section 4.2.2, a distinction was made between cohesive and adhesive failures produced by low load and high load scratch tests, the scattered nature of the corrosion product layers in dewing conditions did not allow a distinction to be made; the reported forces are associated with adhesion only.

4.3.2.1 Microscopical Characterization of Iron Carbonate

Figure 43 shows the SEM image of the corrosion product obtained after the experiment described in the methodology section. Some cube-like crystals formed. Under the conditions given, iron carbonate (FeCO_3) is expected to be the corrosion product layer. The area of each oblong crystal formed was determined by individually measuring one side of the crystals (a sample of 50). The area was then calculated by squaring the side

(under the assumption that the crystals were a perfect cube). The average and standard deviation were obtained for the area of the crystals. The area occupied by a crystal area was determined to be $17 \pm 10 \mu\text{m}^2$.

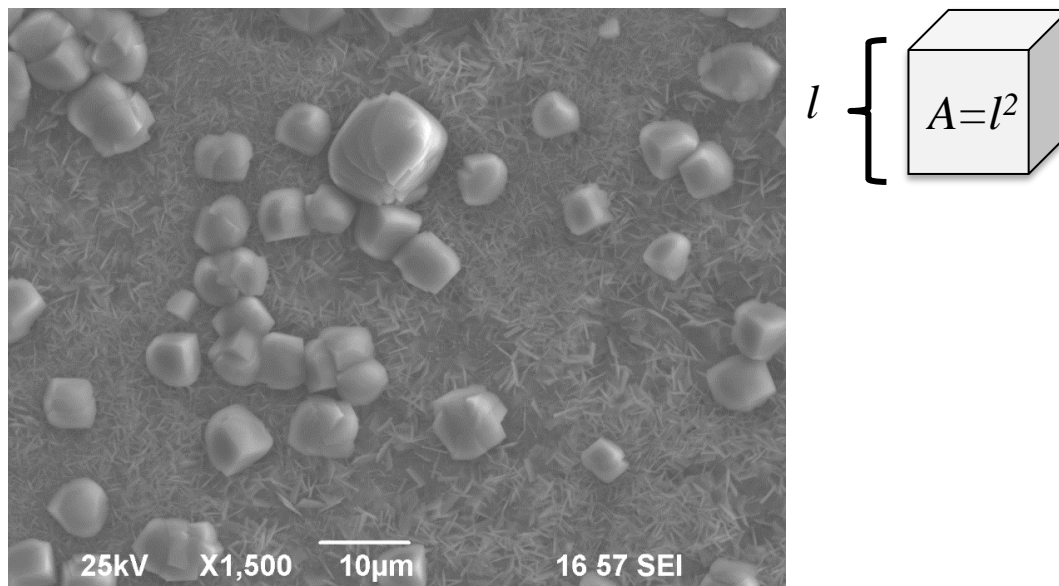


Figure 43. SEM image of iron carbonate crystals obtained under dewing conditions. The area of the crystals was calculated assuming a perfect cube. Crystal area: $17 \pm 10 \mu\text{m}^2$.

Figure 44 shows the EDS quantitative analysis of the crystals. The main elements detected during the analysis are iron, carbon, and oxygen; consistent with the formation of iron carbonate.

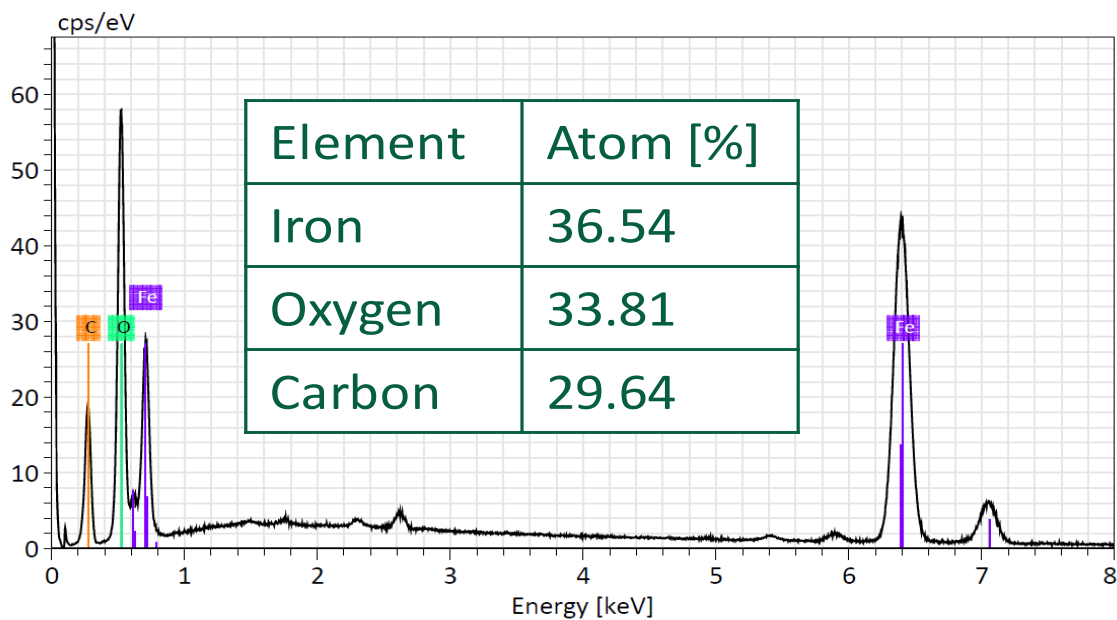


Figure 44. EDS Spectra and quantitative analysis of the crystals developed under CO₂ dewing conditions.

4.3.2.2 Constant Load Scratch Test

Since the resulting layer in dewing conditions is comprised of discrete crystal, the Ollivier and Matthews model could not be applied. Instead, Equation (25) was utilized to calculate the critical shear stress to induce crystal removal. Figure 45 shows that, at 2 mN of normal force, the iron carbonate crystals are removed from the substrate. The associated critical shear stress was determined to be 150 ± 20 kPa.

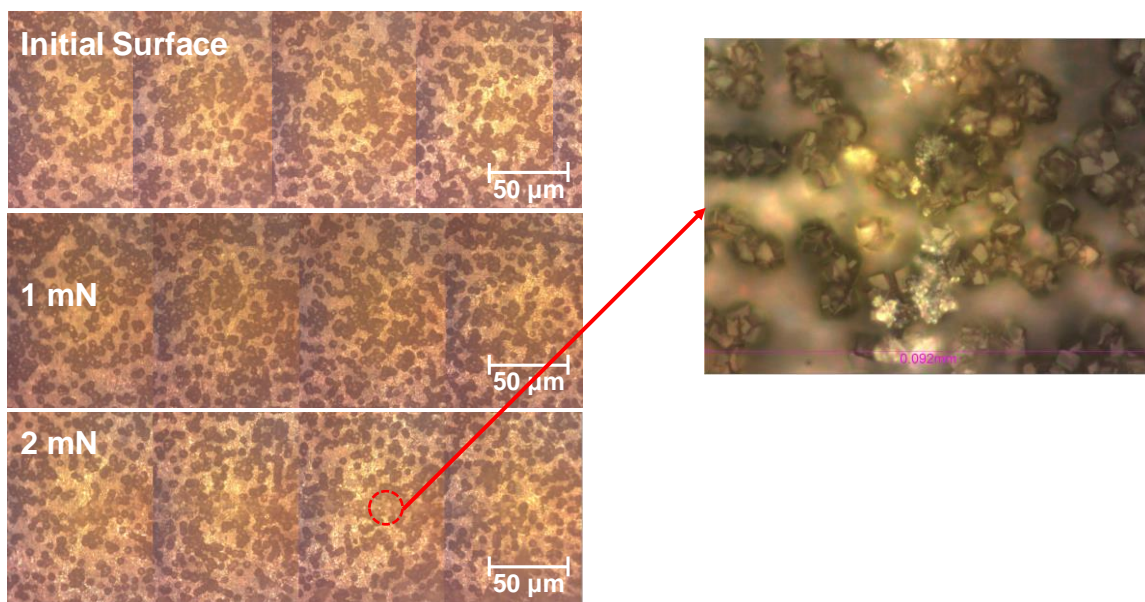


Figure 45. Constant load scratch test to determine the minimum value that produces damage to the crystals.

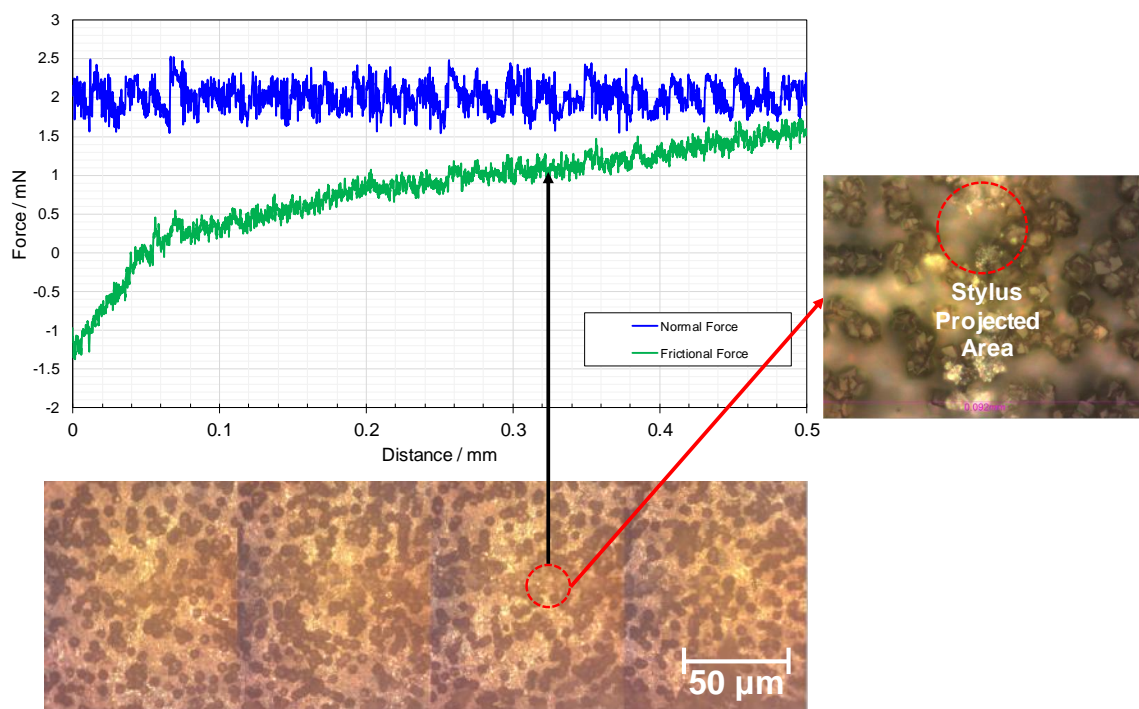


Figure 46. Determination of frictional forces associated with cohesive failure of the iron carbonate crystals.

4.3.2.3 Shear Stress Determination

Shear stress determination was done with the Ollivier & Matthews model, similarly to the fully developed layer. Figure 47 shows the progressive load scratch test of the iron carbonate in dewing conditions as well as the forces and coefficient of friction calculated at selected normal forces with the Ollivier and Matthews formulae, Equation (28) and Equation (29), respectively.

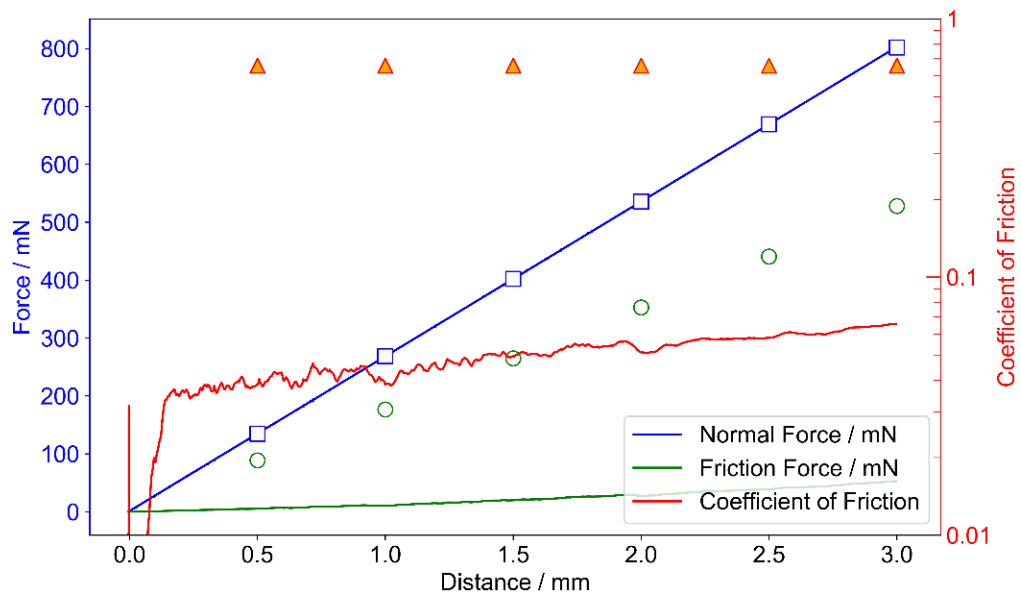


Figure 47. Progressive load scratch test of the iron carbonate in dewing conditions. Solid lines: experimental values. Markers: calculated values by the Ollivier and Matthews formulae per Equation (28) and Equation (29) as a function of selected normal forces.

The shear stress was also calculated with the Ollivier and Matthews formula using Equation (27). Experimental tangential forces as well as calculated tangential forces from Figure 47 were used for the calculations. Figure 48 shows the comparison between the shear stress values obtained. The difference at any point is an order of magnitude or higher.

The data suggest that the delamination behavior of the iron carbonate layer formed under dewing conditions does not obey the Ollivier and Matthews model.

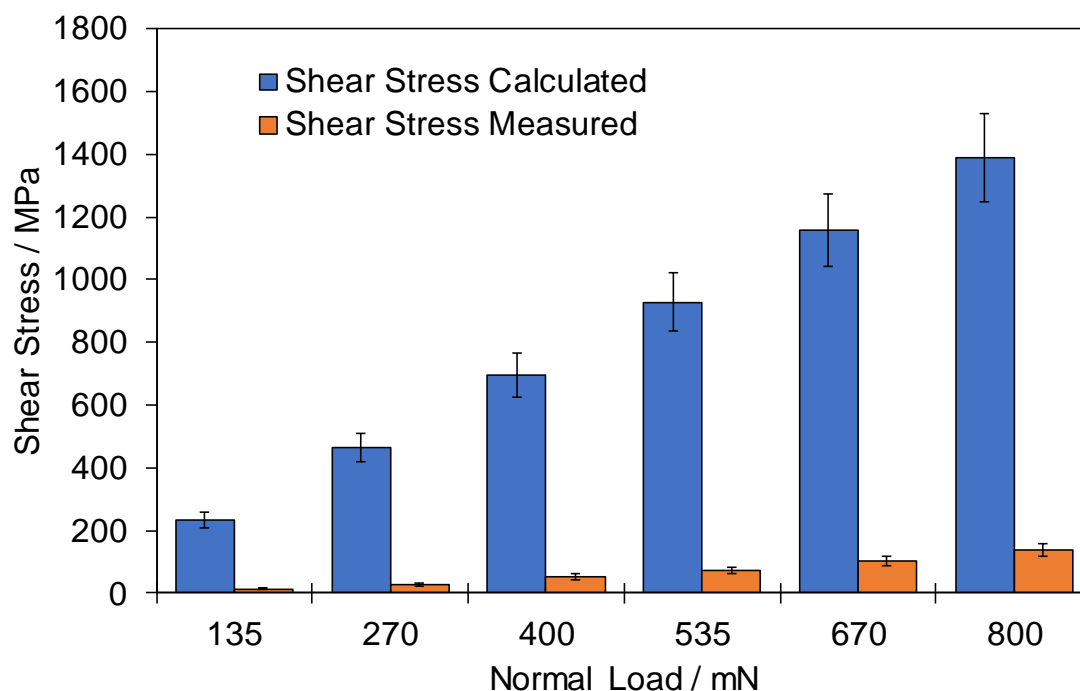


Figure 48. Comparison of the tangential forces obtained at cohesive, adhesive and full delamination with the Ollivier and Matthews approach per Equation (28) and measured experimentally.

4.3.2.4 Critical Shear Stress

Since the Ollivier and Matthews model is not valid to describe the behavior of the tangential force of the iron carbonate grown under dewing conditions, the shear stresses were calculated by using experimental values in conjunction with Equation (25). By using microscopy, the associated delamination failure was found at a normal force of *ca.* 400 mN. The shear stress was then estimated with the experimental lateral force as 125 kPa, a value almost three orders of magnitude below the critical shear stress of a fully

developed iron carbonate layer. Such a difference can be attributed to the potential tensile stresses that the crystals experienced in dewing conditions, and the compressive stresses in the fully developed layer. As mentioned in the scratch testing theory section, compressive stresses can increase the tangential force required to produce a failure.

4.4 Summary

- Lateral force microscopy (LFM) was barely adequate to assess the adherent properties of a discrete iron carbonate layer and totally insufficient for the fully-developed iron carbonate layers. Such results can be explained with the size of the tip. The thickness of the fully developed iron carbonate layer is larger than the AFM tip by a factor of 2-3.
- Scratch test and nanoindentation was proven as a good technique to obtain repeatable results in terms of cohesive and adhesive shear stresses for fully developed iron carbonate layers. The values obtained are in good agreement with values reported in the literature.
- Regarding the comparison between the critical shear stress of the iron carbonate layers grown in aqueous and dewing conditions, Figure 49 shows the comparison of critical shear stresses for layers grown at different conditions utilizing the frictional force and the indentation area.

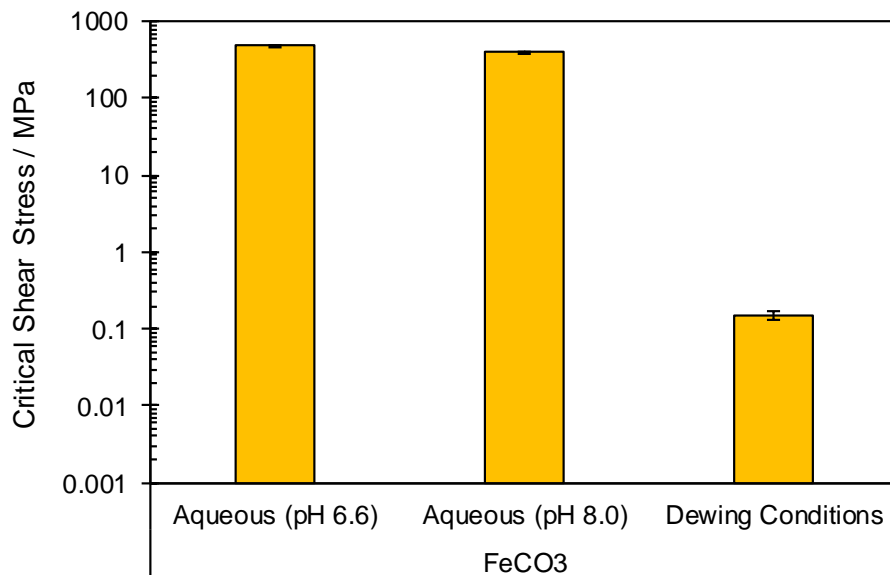


Figure 49. Comparison of critical shear stresses to produce an adhesive failure of iron carbonate layers grown in different conditions.

- The initial hypothesis is accepted: Iron carbonate crystals grown in dewing conditions have a critical shear stress three orders of magnitude lower than those grown in aqueous environments. Such a difference can be attributed to potential tensile stresses of the crystals, as the O&M approach overpredicted the critical shear stress for delamination.

CHAPTER 5: MECHANICAL CHARACTERIZATION OF IRON SULFIDE LAYERS

5.1 Introduction

After the validation of the scratch test and nanoindentation methods as reliable techniques to assess the adhesive and cohesive properties of iron carbonate layers, for discrete crystals and fully-developed layers, the focus of this chapter was to extend the use of those techniques on iron sulfide layers. Special attention is paid to this type of layer due to its morphological nature relating to the conditions under which it forms, specifically, the layer is composed of a “fluffy” mackinawite outer layer and a more adherent inner layer. As pointed out in the previous chapter, one of the caveats of the techniques previously utilized in the open literature to assess the adherence forces of corrosion product layers was that a distinction cannot be readily made between adhesive and cohesive failure. Determining this an essential characteristic for the iron sulfide layer relating to corrosion and black powder formation. Consequently, the scratch test was utilized to provide meaningful information about the mechanical characteristics of this layer. With this advantage, the initial hypothesis regarding the cohesive failure of an iron sulfide layer was tested.

5.2 Iron Sulfide Formed in Aqueous Environments

All the work associated with the formation and mechanical characterization of iron sulfide in aqueous environments must be credited to Dr. Ezechukwu Anyanwu. Dr. Anyanwu performed scratch testing to determine the cohesive and adhesive failures of mackinawite layers formed in aqueous conditions (involving a bulk electrolyte) [86]. This

section outlines the key results of his studies in order to make a comparison with iron sulfide layers developed under dewing conditions (condensed water).

5.2.1 Experimental Method

An iron sulfide layer was grown using the experimental conditions listed in Table 7 and mechanically characterized as shown in Table 8 [86].

Table 7

Experimental Conditions to Develop a Uniform Layer of Iron Sulfide (FeS)

Parameter	Value
Temperature of solution / °C	30
Sparge gas	N ₂ + 10% H ₂ S
Substrate material	API 5L X65 Steel
Solution	1 wt.% NaCl
Solution pH	6.0
Duration	3 day

Table 8

Scratch Testing Parameters for Iron Sulfide (FeS) Testing

Parameter	Value
Type of load	Progressive, Constant
Initial load (N)	0.01
Final load (N)	0.3
Loading rate (N/min)	0.075
Scratch length (mm)	1
Scratching speed (mm/min)	0.25
Indenter geometry	120° cone

5.2.2 Results and Discussion

5.2.2.1 Microscopical Characterization of Iron Sulfide

Figure 50 shows the SEM image of the corrosion product layer formed.

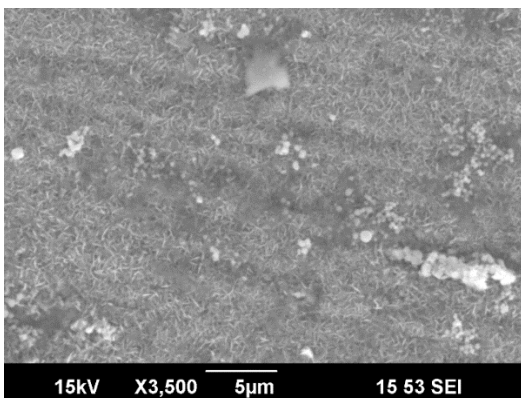


Figure 50. Iron sulfide layer obtained after the 3-day experiment listed in Table 7.

It can be seen from Figure 51 that the product is mackinawite, according to the XRD pattern.

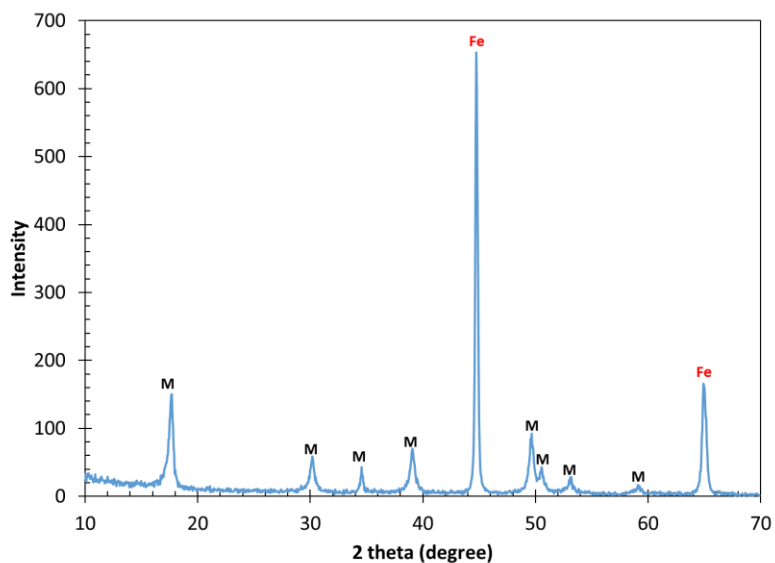


Figure 51. XRD pattern showing the presence of mackinawite (M) [87]

5.2.2.2 Progressive Load Scratch Test

Figure 52 shows the progressive load scratch test. The critical failures associated with mackinawite formed in aqueous conditions.

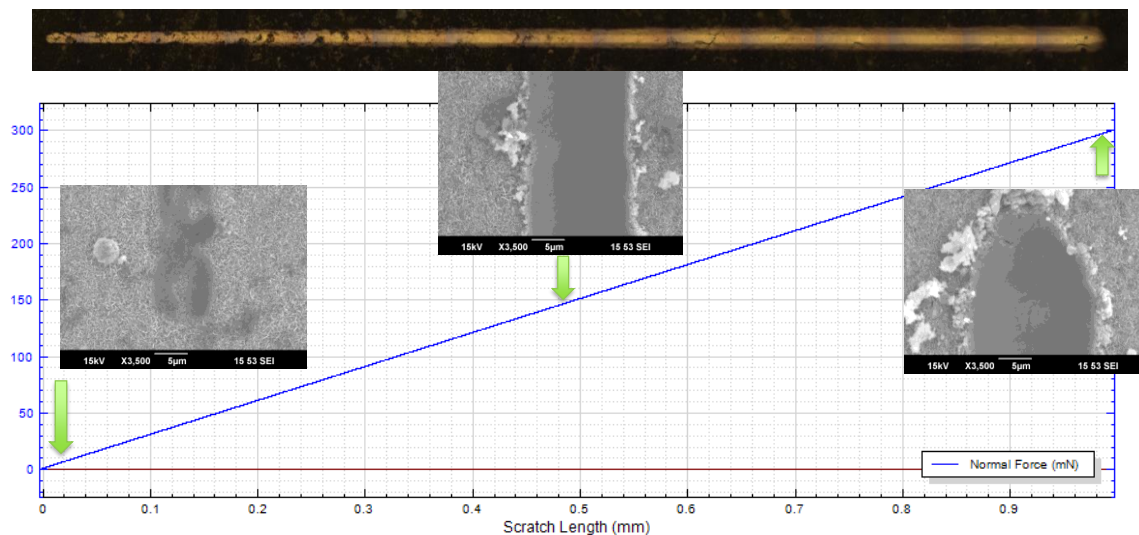


Figure 52. Progressive load scratch test on mackinawite. SEM images shows a cohesive failure at low forces (*ca.* 20 mN) and adhesive failure at the range of 150-300 mN of normal force.

Figure 53 shows the EDS analysis at the failures. The analysis showed that the failure was found at 300 mN of normal force.

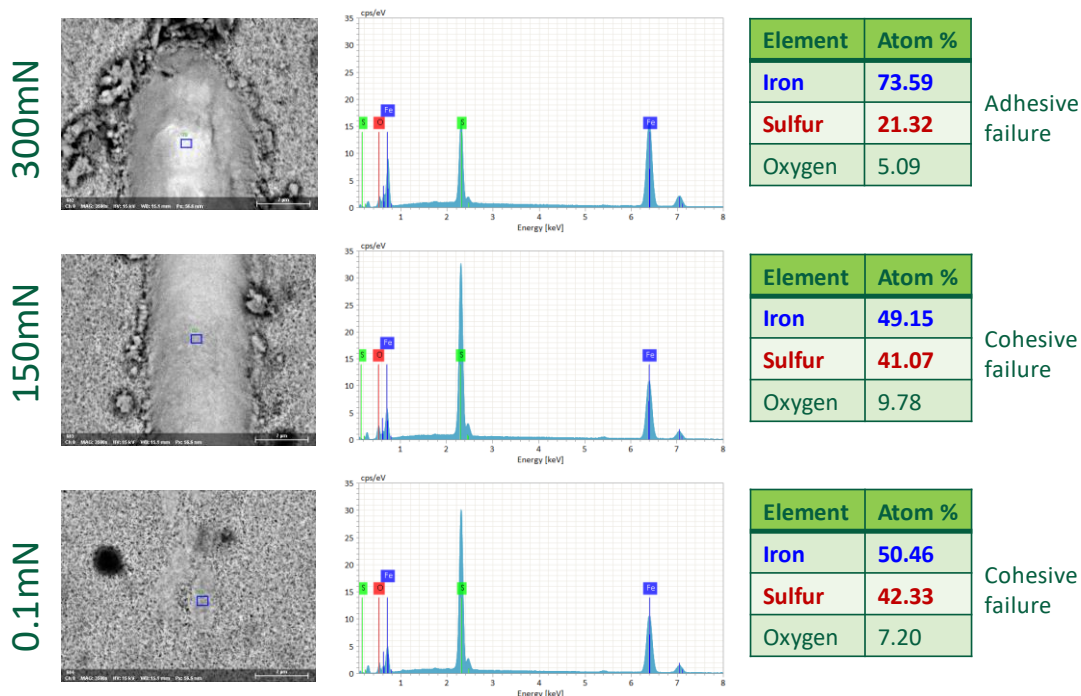


Figure 53. EDS analysis of forces indicated in Figure 52. SEM images in backscatter mode. Elemental analysis indicates adhesive failure at 300 mN of force.

5.3 Iron Sulfide in Dewing Conditions

5.3.1 Experimental Method

Table 9 shows the experimental conditions to develop a layer of iron sulfide under dewing conditions. The goal for this step is to simulate operational conditions present in transporting gas pipelines. Since the *in situ* pH of the condensed water on the steel is challenging to measure, MULTICORP™ was used to calculate the pH of the condensed water. The working apparatus is similar to the one depicted in Figure 42. The concentration of hydrogen sulfide (H₂S) was chosen from previous black powder formation studies [85], [88].

Table 9

Experimental Conditions to Develop an Iron Sulfide Layer under Dewing Conditions

Parameter	Value
Gas temperature / °C	30
Temperature of solution / °C	35
Sparge gas	N ₂ + 100 ppm _v H ₂ S
Substrate material	API 5L X65 Steel
Solution	Deionized (DI) water
Calculated initial pH (condensed water)	3.92
Temperature of steel / °C	25
Duration	3 day

5.3.2 Results and Discussion

5.3.2.1 Microscopical Characterization of Iron Sulfide

Figure 54 shows the SEM images of the corrosion product layers after three days of exposure to the corrosive environment. The corrosion product was then analyzed by EDS to obtain the chemical composition.

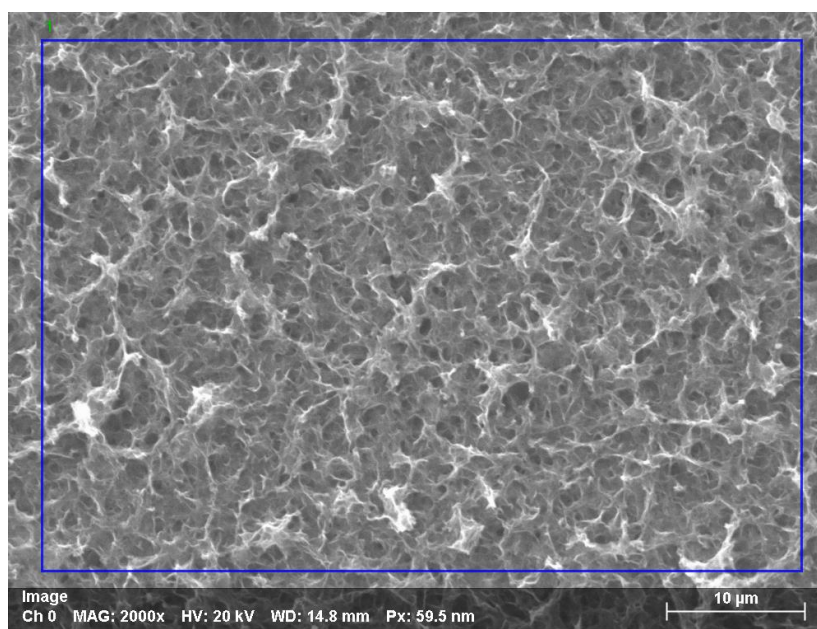


Figure 54. Iron sulfide layer developed in dewing conditions.

Figure 55 shows the spectra and the atom percent composition of the layer. The analysis revealed that the stoichiometric composition of the layer is close to a 1:1 molar ratio of iron (Fe) and sulfur (S).

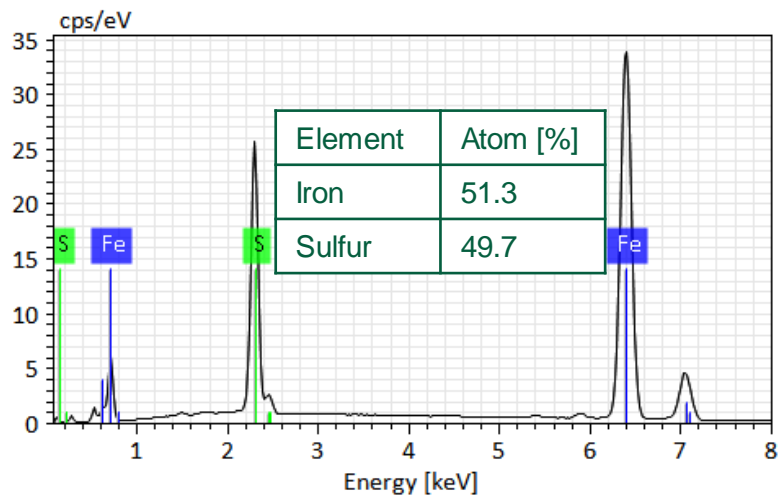


Figure 55. EDS analysis of the iron sulfide developed in dewing conditions. Quantitative chemical analysis indicated an even presence of iron and sulfur.

Continuing with the analysis, Figure 56 shows that the XRD pattern is consistent with the formation of a poorly crystalline mackinawite layer.

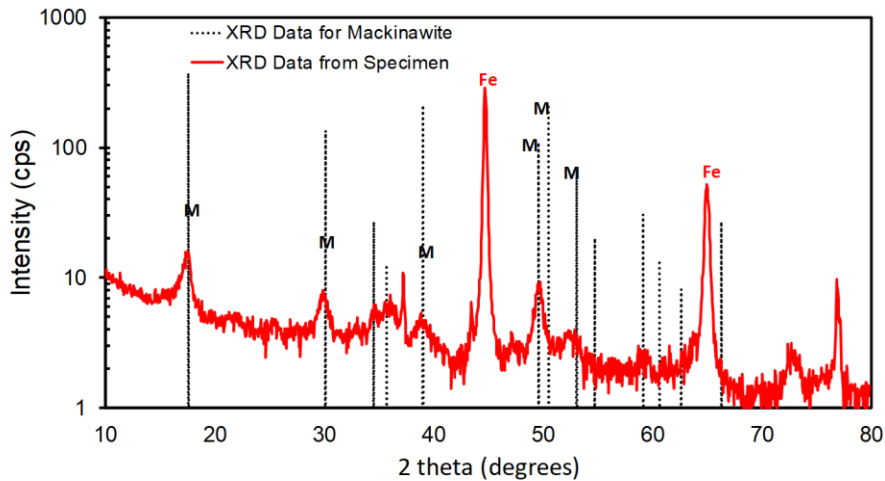


Figure 56. XRD pattern of the iron sulfide layer. Broad peaks revealed the presence of a poorly crystalline mackinawite layer.

5.3.2.2 Determination of Critical Shear Stresses

The determination of the critical shear stress to produce adhesive failure in FeS was determined by the Ollivier and Matthews (O&M) approach and by direct measurement of the friction forces. The two methods were compared in terms of the coefficient of friction. Figure 57 shows a constant load scratch test at 240 mN of normal force. The experimental coefficient of friction is almost five times lower than that predicted by the O&M approach. The difference can be explained in terms of the nature of the outer FeS layer. The “fluffy” layer requires less shear force to be damaged/detached.

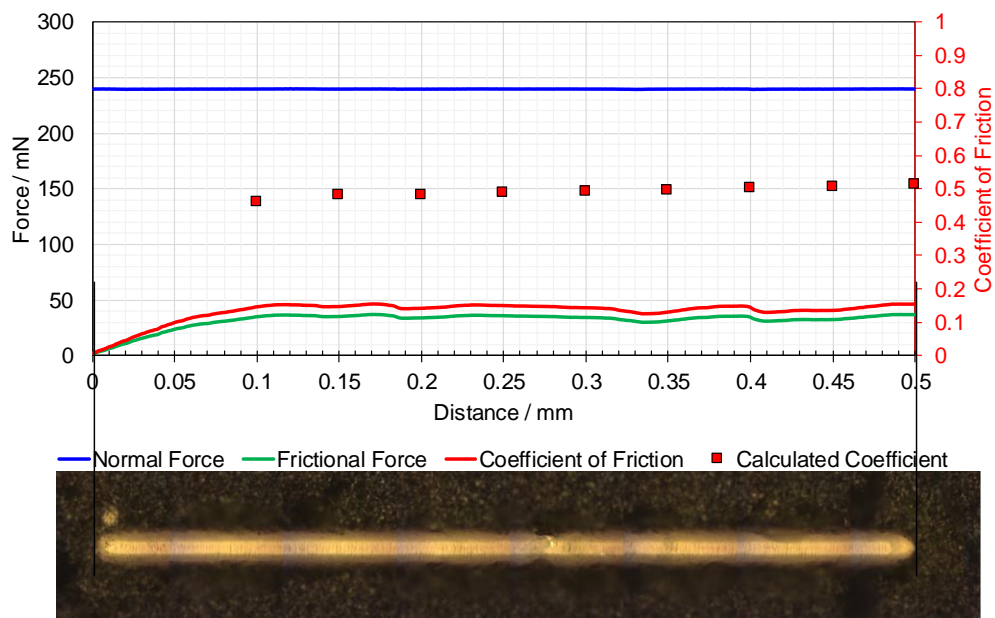


Figure 57. Comparison of O&M approach with experimental friction coefficients.

The discrepancy in terms of frictional forces between the O&M approach and the frictional force can be seen in shear stress calculations at delamination. Figure 58 shows an adhesive failure produced at the 240 mN constant-load scratch test. The critical shear stress with the O&M formula was 297 MPa, whereas the experimental was determined to be 44.2 MPa.

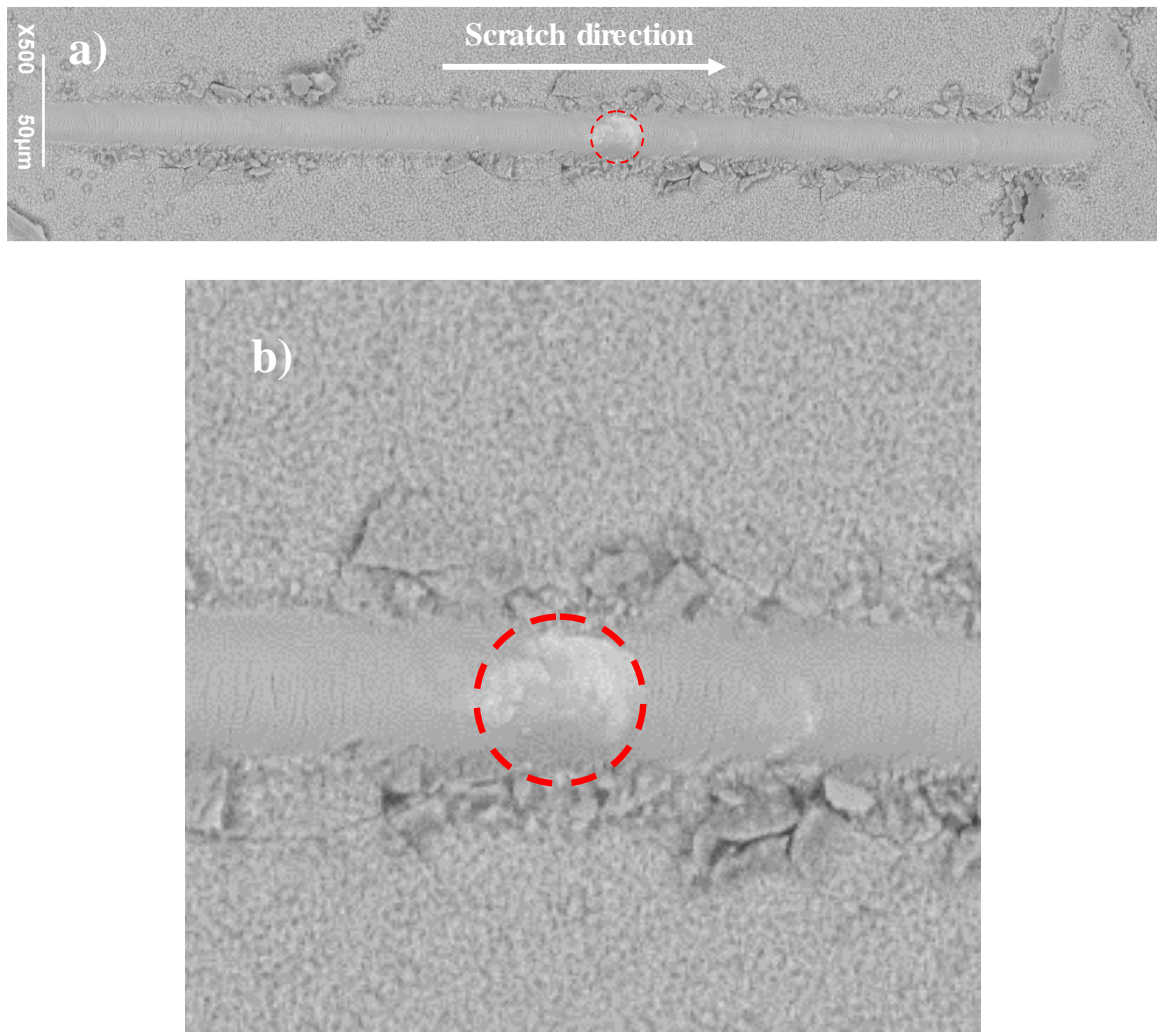


Figure 58. a) Constant load scratch test at 240 mN on an FeS layer grown under dewing conditions. b) zoom into the delamination zone during the test.

Figure 59 shows that delamination also occurred in the 300 mN constant load scratch test. Results showed a discrepancy again in the calculated coefficient of friction (as a solely function of the applied normal force) and the measured one. However, this time the discrepancy was within a factor of two.

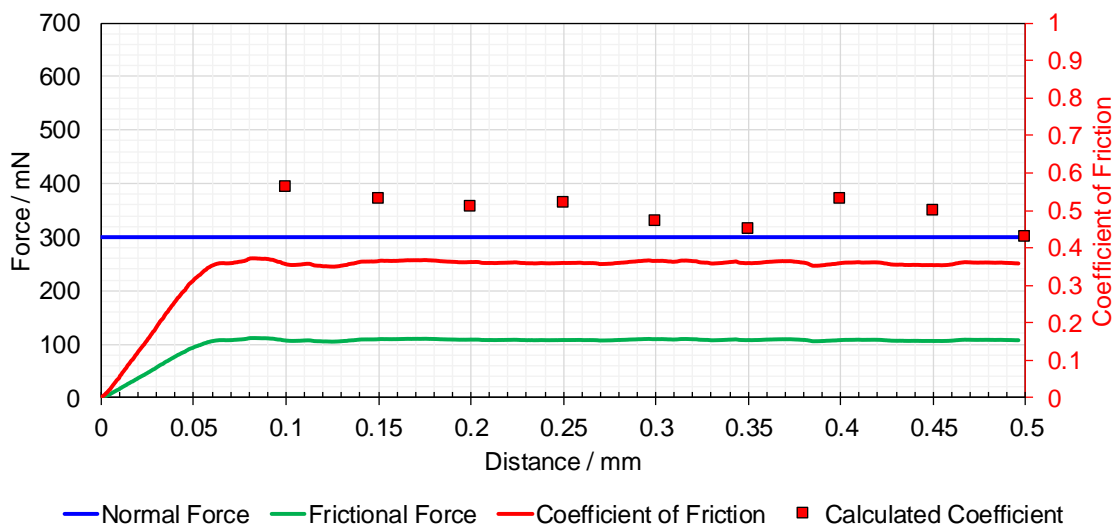


Figure 59. Experimental forces and coefficient of friction (lines) and estimated coefficient of friction (square marker) for a 300 mN constant load scratch test.

Figure 60 shows the scratch test on the layer and the delamination that occurred.

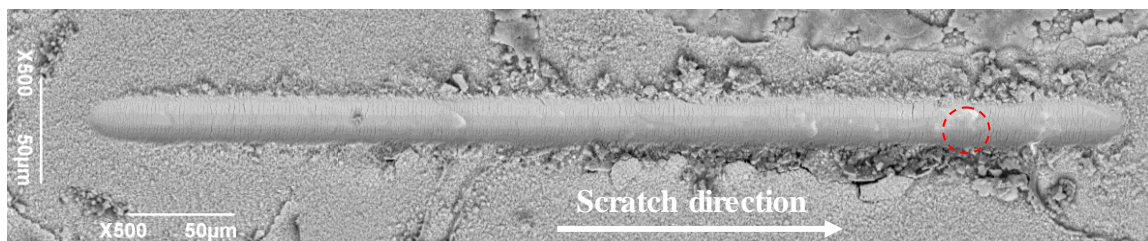


Figure 60. 300 mN constant load scratch test. Red circle: adhesive failure detected.

By using the Ollivier and Matthews formula, as well as the experimental frictional forces, the critical shear stress values were determined to be 551 and 334 MPa, respectively. Following the experimentation, the coefficient of friction was obtained for different constant load scratch tests. The comparison is shown in Figure 61. The parity plot indicated that at forces higher than 300 mN, the Ollivier and Matthews formula is

applicable since the results lie within a factor of two with respect to the experimental coefficients. Such tendency can be explained by postulating that the friction coefficient at higher force is more influenced by the substrate (X65 steel) whose friction coefficient was between 0.4 and 0.6.

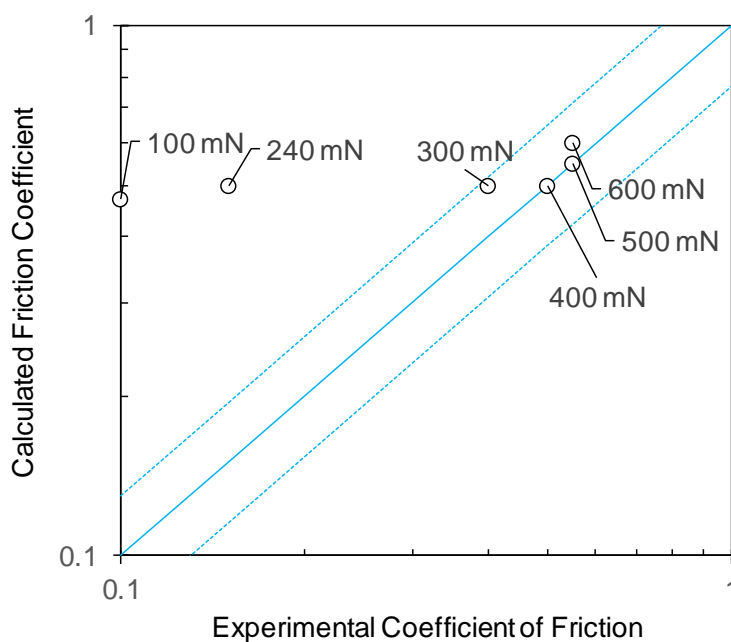


Figure 61. Parity plot showing the comparison between the calculated friction coefficient (y-axis) vs. the experimental coefficient of friction (x-axis) for different constant load scratch tests.

Since there was a discrepancy between the estimated and measured values of frictional forces the thickness of the layer was measured, as it is reported that the thickness of the layer might act as a source of error in the calculations if it surpasses the radius of the indenter.

5.3.2.3 Cross-section Analysis of the Iron Sulfide Layer

Figure 62 shows the cross-section analysis of the iron sulfide layer. As reported in previous research [86], [89], its thickness comprised of an outer “fluffy” layer and a more compact inner layer.

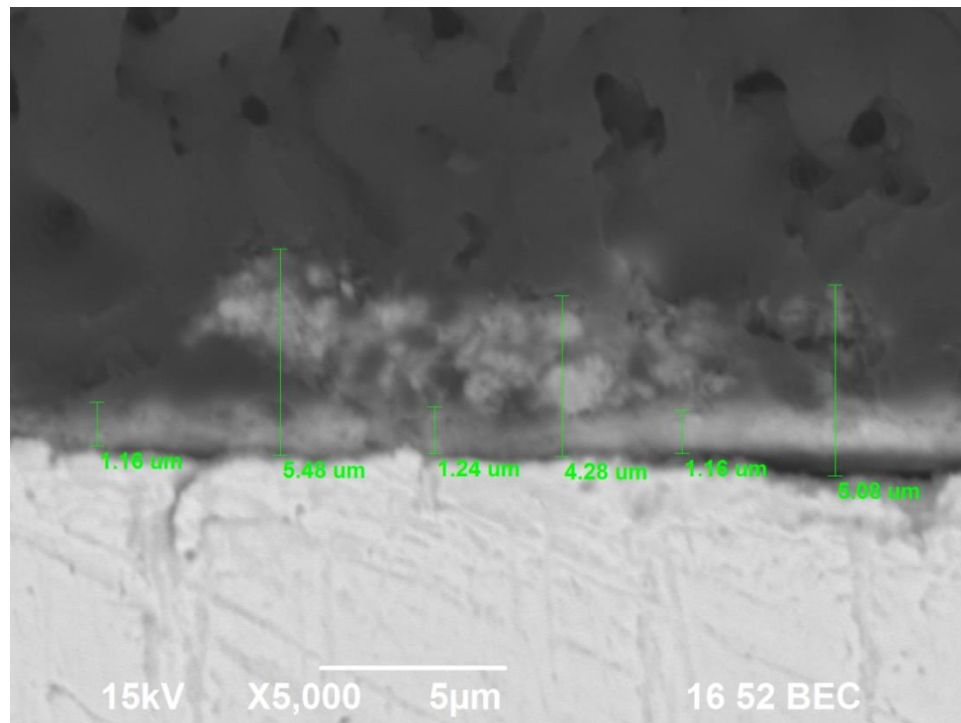


Figure 62. Cross-section analysis of the iron sulfide layer formed under dewing conditions. The thickness of the layer (combining outer and inner layer was $3 \pm 2 \mu\text{m}$).

Compositionally speaking, the outer and inner layer are similar; as determined by EDS mapping analysis as shown in Figure 63. However, the outer layer has been qualitatively reported to have low adherence properties [86], [89]. The thickness of both layers combined is of the order of $5 \mu\text{m}$, four times smaller than the radius of the indenter tip ($20 \mu\text{m}$). Consequently, the discrepancy between the calculated and measured

frictional force can be related to the low adherence properties of the outer layer as it comprises about 60% of the total thickness of the layer. Profilometry analysis was utilized to explore this postulate.

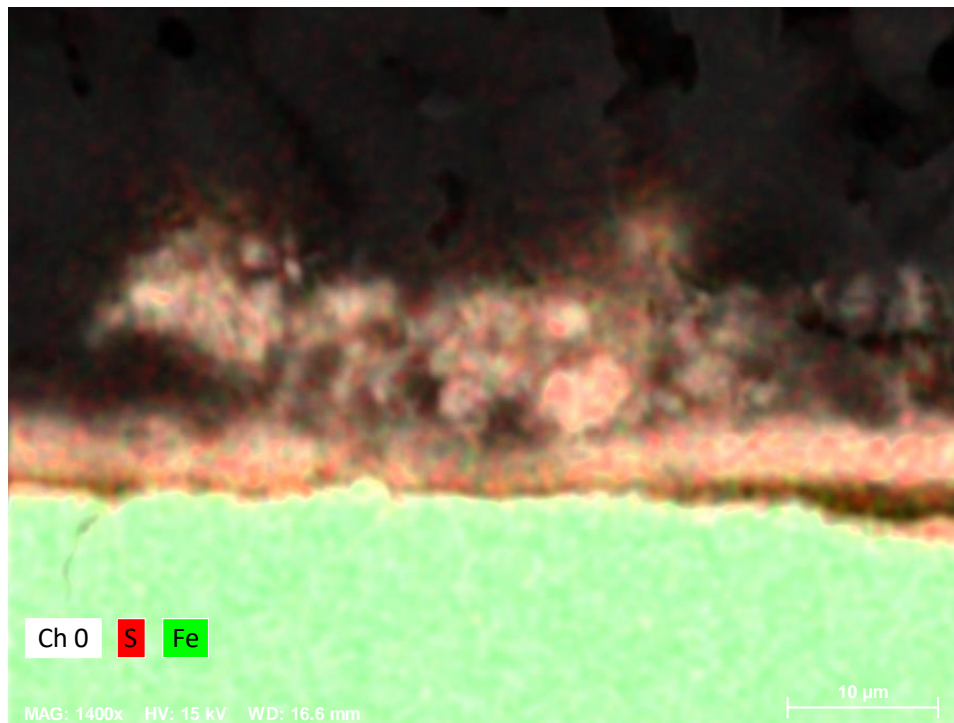


Figure 63. EDS mapping on cross-section analysis of the iron sulfide layer formed under dewing conditions. The analysis revealed that the outer “fluffy” layer is compositionally similar to the inner, compact layer.

5.3.2.4 Profilometry Analysis of the Iron Sulfide Layer

The profilometry analysis for the constant load scratch tests showed the penetration of the indenter during the test. Figure 64 shows the profilometry analysis of the 240 mN constant load scratch test on iron sulfide. The penetration during the test is *ca.* 2 μm, which is likely insufficient to reach the inner layer as the outer layer thickness is of the order of 3 to 4 μm.

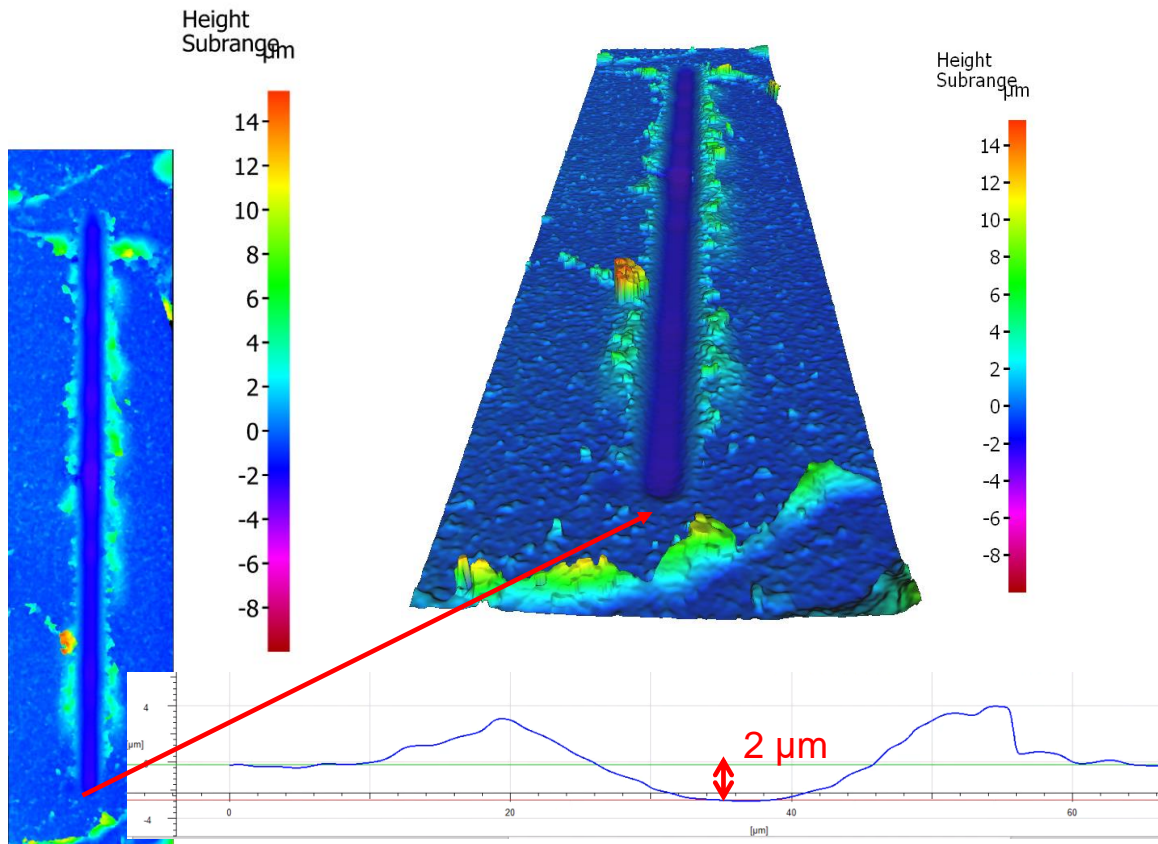


Figure 64. Specimen profilometry of a 240 mN constant load scratch test. Penetration by the scratch tester tip: $\sim 2 \mu\text{m}$.

On the other hand, the estimated and calculated friction forces for a scratch test with 300 mN of normal load lied within a factor of 2, according to the parity plot in Figure 61. Exploring the profilometry of the constant load test, as per Figure 65, the indenter penetrated 3-4 μm , which is likely to reach the inner layer and the metal. Consequently, the measured forces are governed by such a layer, which obeys the Ollivier and Matthews postulate.

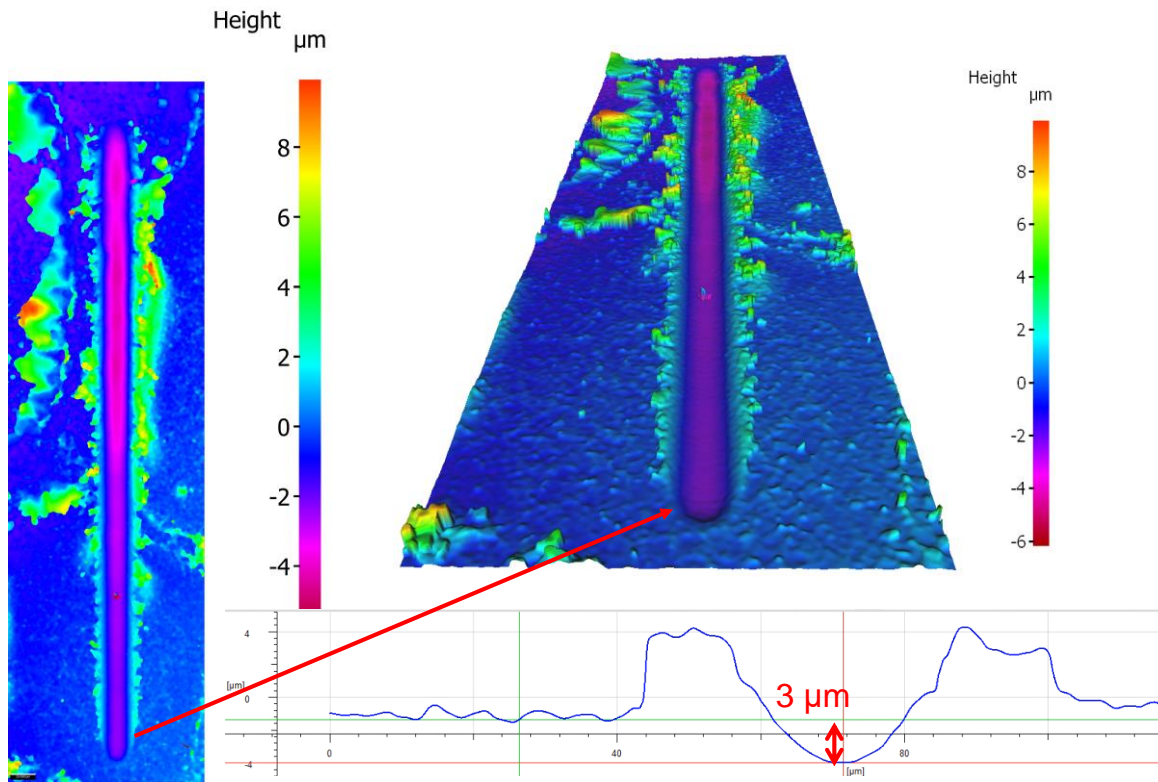


Figure 65. Specimen profilometry of a 300 mN constant load scratch test. Penetration by the scratch tester tip: $\sim 3 \mu\text{m}$.

5.3.2.5 EDS Mapping Analysis of Adhesive Failures

As a final step, in order to corroborate that the aforementioned delaminations were actually exposing the metal substrate, EDS mapping analysis was performed at selected delamination spots. Figure 66 shows that at the point of delamination, the substrate was exposed.

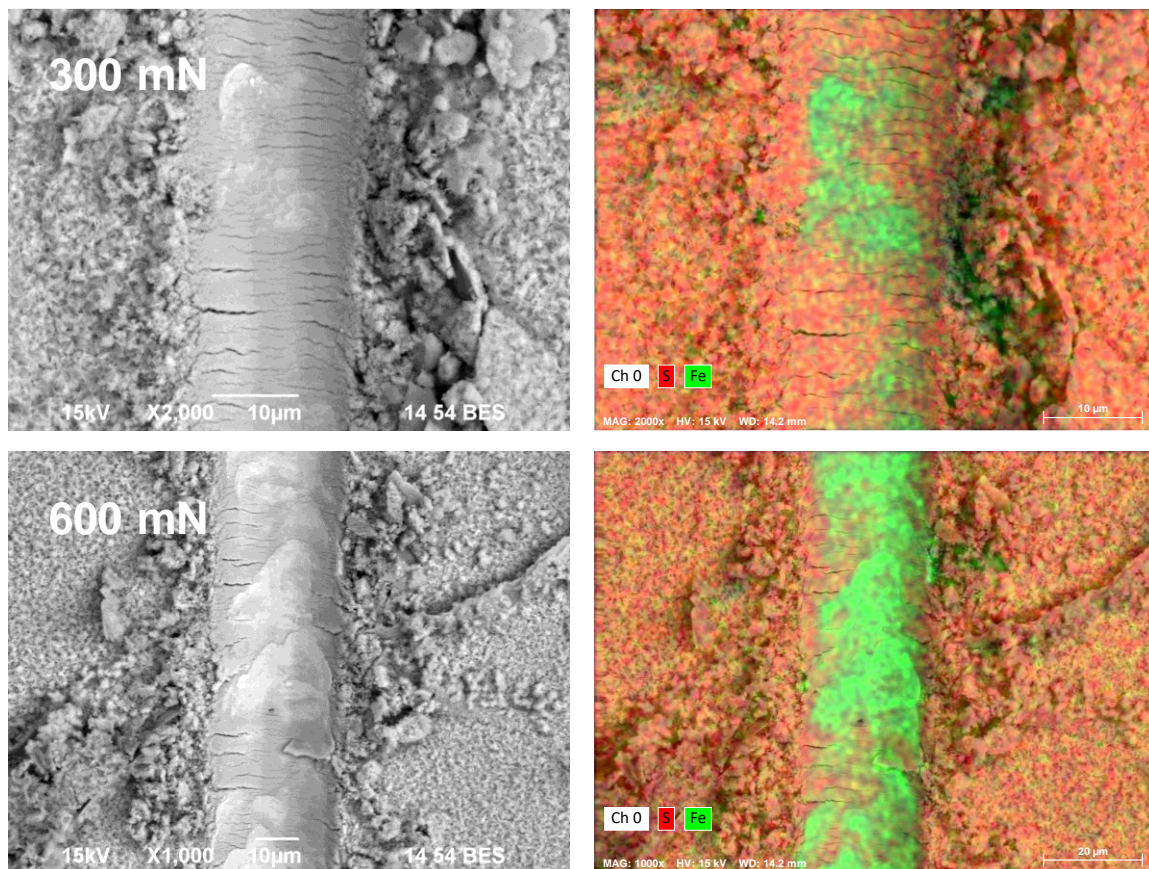


Figure 66. EDS mapping analysis of delamination points of the 300 mN and 600 mN constant load scratch test. Red: sulfur-dominating zones. Green: iron-dominating zones.

5.4 Comparison of Critical Stresses of Layers Grown under Aqueous vs. Dewing Conditions

Figure 67 shows the comparison of the critical shear stresses between the iron sulfide and the iron carbonate grown under aqueous and dewing conditions obtained by the experimental friction force measurements. It is noteworthy that the forces required to produce an adhesive failure are considerably diminished when the layers are grown under dewing conditions. Stress relaxation theory in thin films [10], [12], [38] can explain the observed behavior. In the case of iron carbonate, it is postulated that the tensile stress

experienced by small “islands” of iron carbonate crystals in dewing conditions does not undergo relaxation as in the fully developed layers. For the iron sulfide, the behavior can be explained by the presence of a “fluffy” mackinawite layer, which predominantly forms under dewing conditions over the denser, more adherent iron sulfide layer.

These speculations require to be corroboration. However, the testing of this postulate is outwith the scope of the present thesis. However, in the future work section some methodologies are proposed to test the aforementioned postulate as a hypothesis.

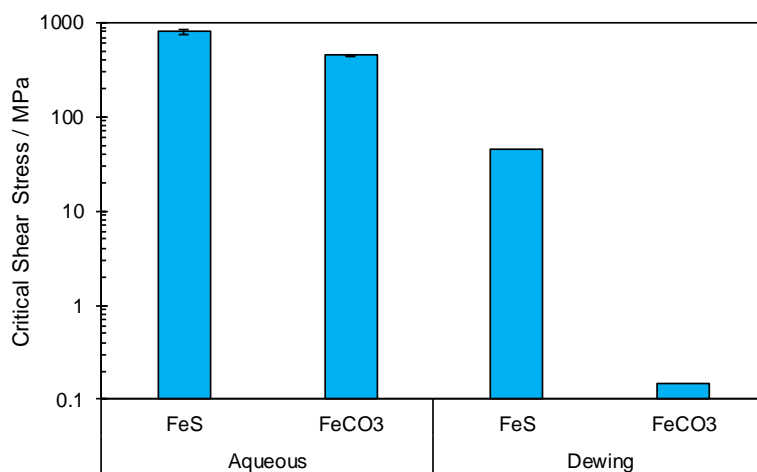


Figure 67. Comparison of critical shear stresses associated with adhesive failure between iron carbonate layers and iron sulfide layers grown in aqueous and dewing conditions.

CHAPTER 6: MECHANICAL CHARACTERIZATION OF CALCIUM CARBONATE SCALES

6.1 Introduction

After exploring the nature of adhesive and cohesive properties of chemically homogeneous corrosion product layers, the attention of this thesis is turned into the other type of products present in the corrosion of oil and gas industry assets: scales. Scales are different from corrosion products layers because their precursors are derived from the bulk aqueous environment rather than the corrosion process itself. From the adherence assessment perspective, the scale layers are different from the corrosion product layers since the metal substrate does not necessarily need to corrode to form the scale. Consequently, the substrate undergoes less undermining, and the layer is “deposited” onto the metal substrate by precipitation. One of the scales most commonly found in oil and gas transportation pipelines, as well as in municipal water lines, is calcium carbonate. Calcium carbonate is isostructural to iron carbonate. This makes possible that iron carbonate layers possess substitutional calcium in their lattice, and vice versa. Keeping that in mind, the last proposed hypothesis related to substitutional elements on lattices influencing the mechanical removal of corrosion product layers was tested by first assessing the adhesive and cohesive forces of a pure calcium carbonate layer precipitated onto X65 steel. This information was further utilized to make a comparison when calcium carbonate grows along with iron carbonate. The following sections describe the experimental procedure followed to assess the adherence of the abovementioned layers.

6.2 Pure CaCO₃ layer

6.2.1 *Experimental Method*

In order to obtain a pure calcium carbonate scale on the metal substrate, a special procedure proposed by Mansoori [27] was followed. The method consists of the following steps:

1. Prepare a CO₂-sparged solution with 1 wt.% NaCl, set to a pH 6.2 with the addition of sodium bicarbonate (NaHCO₃).
2. Immerse a steel specimen and cathodically protect it by polarizing the specimen - 300 mV to -500 mV with respect to the open circuit potential in order to avoid corrosion.
3. Injection of 400 ppm of calcium ions (Ca²⁺) in the form of calcium chloride (CaCl₂) to promote supersaturation of calcium carbonate (CaCO₃).
4. Monitor the current until diminished to almost zero. This indicates the precipitation of calcium carbonate as the formation of the scale blocks the associated electrochemical reactions from happening.
5. Finally, the second injection of 400 ppm of calcium ions was done in order to ensure the formation of a blocking, thick scale.

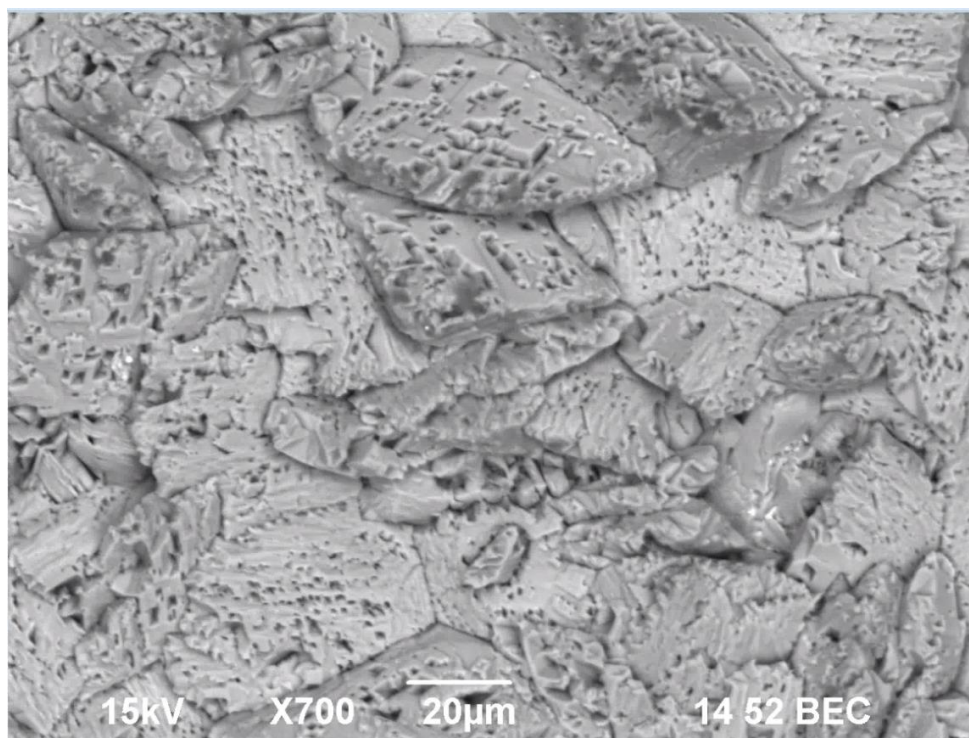
Table 10

Experimental Conditions to Develop a Calcium Carbonate Layer

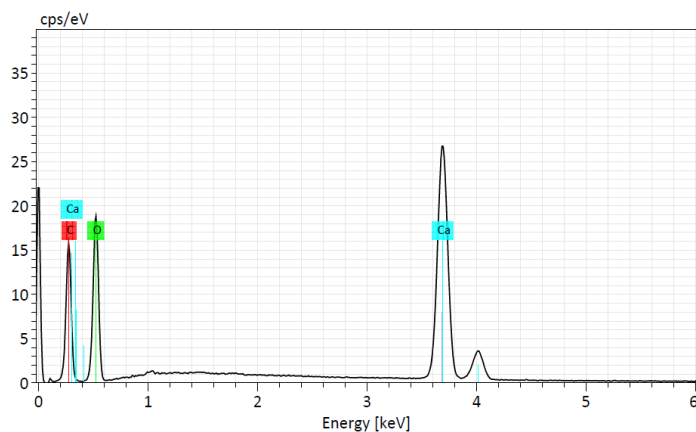
Parameter	Value
Temperature of solution / °C	80
Spurge gas	0.53 bar CO ₂
Substrate material	API 5L X65 Steel
Solution	1 wt.% NaCl + 800 ppm _w Ca ²⁺
pH	6.2 ± 0.1
Duration	1 day

*6.2.2 Results and Discussion**6.2.2.1 Microscopic and Chemical Characterization*

An SEM image of the scale formed is shown in Figure 68. Note the large, intergrown and porous crystals.

Figure 68. SEM image of the CaCO₃ scale

EDS analysis, as shown in Figure 69, revealed the presence of oxygen, calcium, and carbon as the main elements present in the scale.



Element	At. No.	Netto	Mass [%]	Mass Norm. [%]	Atom [%]	abs. error [%] (1 sigma)	rel. error [%] (1 sigma)
Oxygen	8	37819	40.30	46.49	54.17	4.86	12.06
Carbon	6	28523	16.71	19.28	29.91	2.07	12.37
Calcium	20	118805	29.67	34.23	15.92	0.89	2.99
Sum		86.67	100.00	100.00	100.00		

Figure 69. EDS analysis of the corrosion product formed. Oxygen, carbon and calcium are the predominant elements in the chemical composition analysis.

Moreover, Figure 70 shows the XRD pattern of the scale and its comparison with a literature pattern of calcite (CaCO_3).

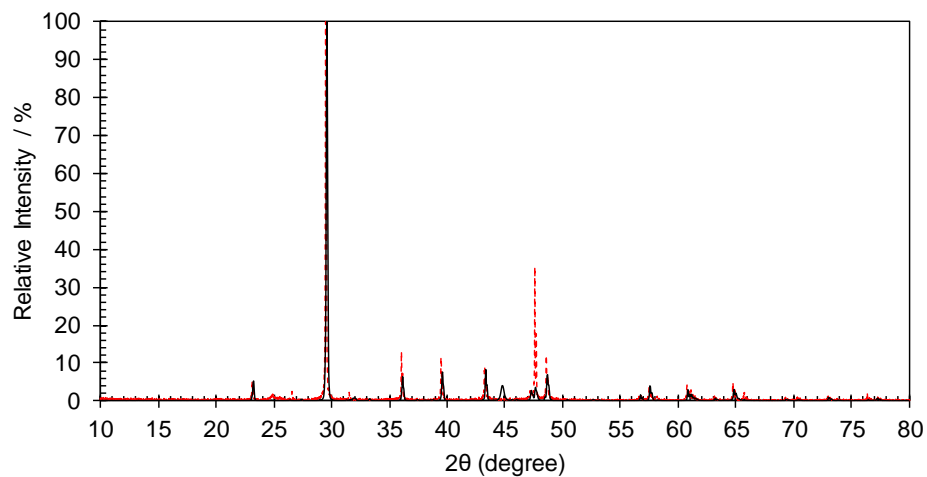


Figure 70. XRD pattern of the generated scale (black) compared with the pattern of calcite, CaCO_3 , (red) [87].

6.2.2.2 Progressive Load Scratch Test

Progressive load scratch tests from 0.1 mN to 800 mN were performed to determine the cohesive and adhesive failure of the calcium carbonate layer. Figure 71 shows the experimental tangential forces and coefficient of friction as well as the calculated frictional forces and the coefficient of friction by the Ollivier and Matthews formulae (Equation (28) and Equation (29), respectively). A good agreement was attained between the experimental and the calculated values.

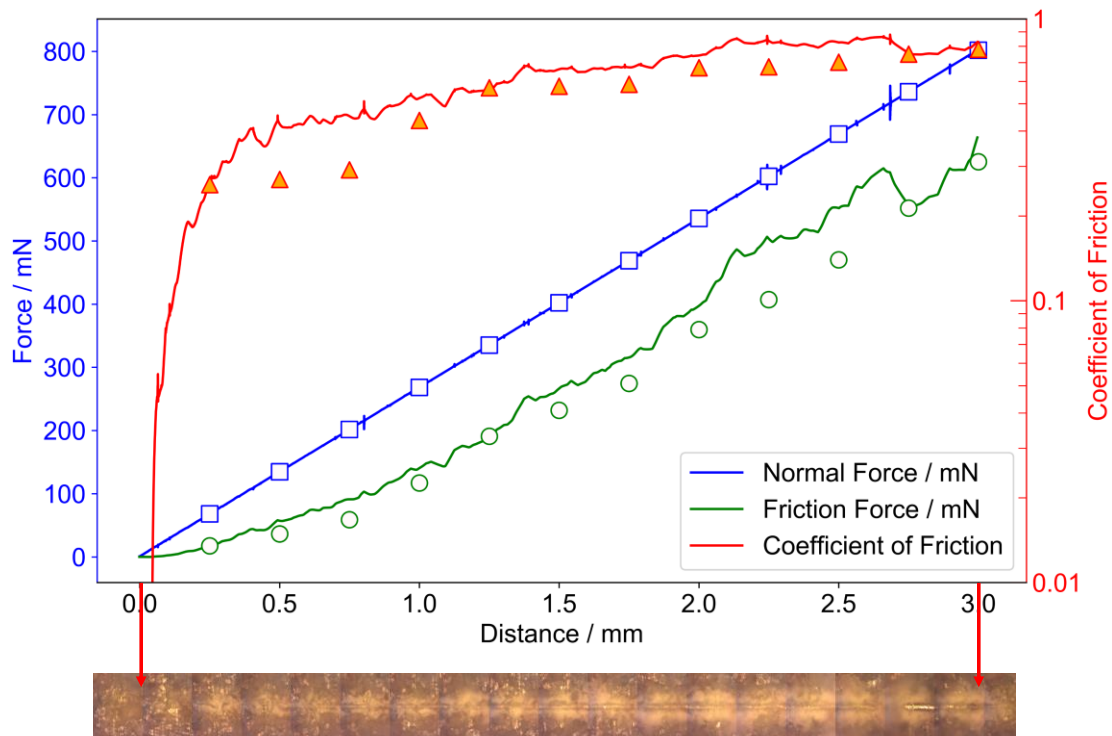


Figure 71. Progressive load scratch test of the calcite as a scale. Solid lines: experimental values. Markers: calculated values by the Ollivier and Matthews formulae as a function of selected normal forces.

As can be seen in Figure 72, the Ollivier and Matthews formula for shear stress also predicted with reasonable accuracy the shear stress at different normal loads in the progressive load scratch test.

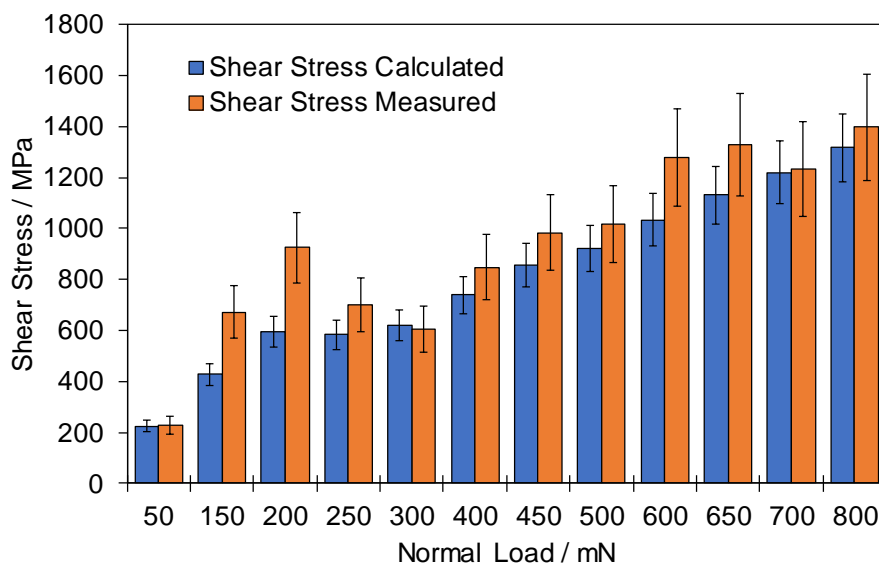


Figure 72. Comparison of calculated shear stresses at selected normal load forces for progressive load scratch test. Blue bars: shear stress calculated by the Ollivier and Matthews formula, per Equation (27). Orange bars: shear stress calculated from experimental frictional forces per Equation (25). Error bars: standard deviation calculated from 5 individual experiments. Critical load determined at 600 mN.

Regarding the adhesive failure, the critical shear stress was determined to be 1.2 ± 0.2 GPa by the experimental frictional force, and 1 ± 0.12 GPa by the Ollivier and Matthews formula, a value that almost doubles the critical shear stress for adhesive failure in the case of iron carbonate (630 MPa).

6.2.2.3 EDS Analysis of the Adhesive Failure

Figure 73 shows the SEM image in backscatter mode of the calcium carbonate failure.



Figure 73. Adhesive failure of calcium carbonate at 700 mN of normal force. Bright zones are associated with the exposure of the metal substrate.

Brighter zones were confirmed to be the substrate by EDS mapping analysis, as shown in Figure 74.



Figure 74. EDS mapping analysis confirming the adhesive failure of calcium carbonate. The iron substrate (in blue) was predominant in the scratch track at the failure.

Finally, it is noteworthy that even at 0.1 mN cohesive failure was detected; the outer part of the scale was pulverized by this force. Figure 75 shows the cohesive failure detected, with an associated shear stress of 160 kPa, determined by the Olliver and Matthews formula, and 155 kPa with the experimental friction forces.

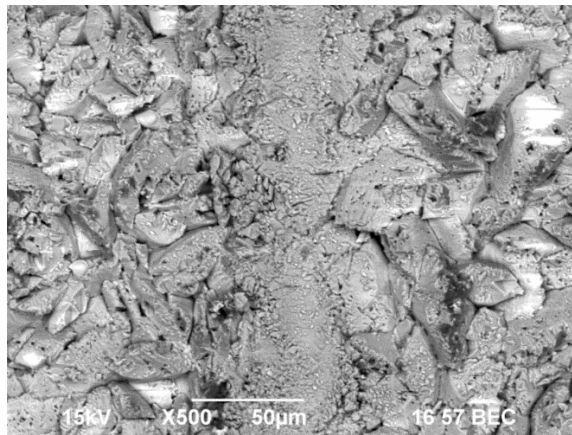


Figure 75. 0.1 mN constant load. Adhesive failure detected.

6.2.2.4 Profilometry Analysis

In order to corroborate that the Ollivier and Matthews analysis holds for calcium carbonate, the profilometry of the specimen at the adhesive failure was performed. Figure 76 indicated that the indenter tip penetrated around 19 μm , which is in the edge of the validity of the analysis (since the indenter has a tip radius of 20 μm).

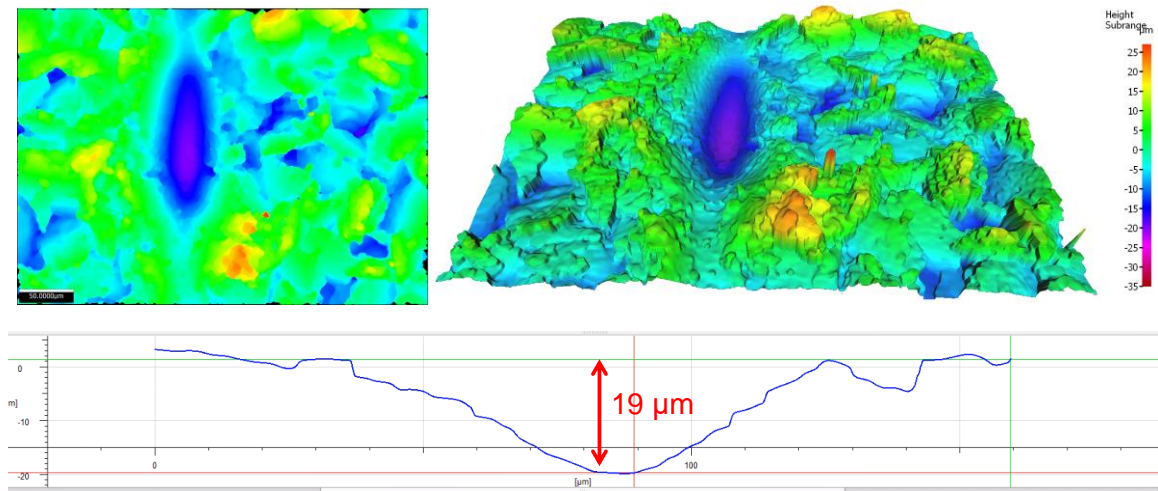


Figure 76. Specimen profilometry of the constant load test at 700 mN. Detected penetration by the scratch tester tip: $\sim 19 \mu\text{m}$.

6.2.2.5 Vickers Indentation Fracture Tests

Figure 77 shows the mark left by the Vickers indenter after the nanoindentation test on calcium carbonate. Fracture toughness was estimated by using Equation (30) as $1 \pm 0.2 \text{ MPa m}^{1/2}$. Compare to pure iron carbonate, the value is lower by a factor of 2. A more detailed comparison is presented in a later section.

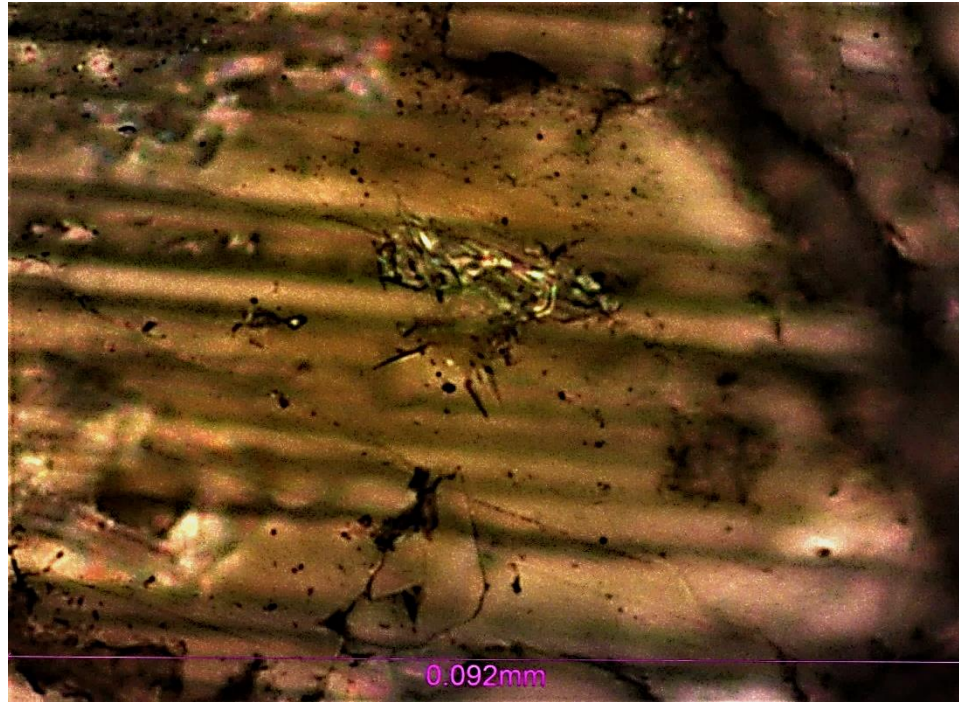


Figure 77. Vickers hardness mark and crack propagation on calcium carbonate.

6.2.2.6 Cross-section Analysis

Cross-section analysis was utilized to determine the thickness of the calcium carbonate layer. Figure 78 shows that the thickness of the layer is $18.5 \pm 1.3 \mu\text{m}$. Figure 79 shows that the layer is compositionally homogeneous (*via* EDS mapping analysis), corresponding to calcium carbonate.

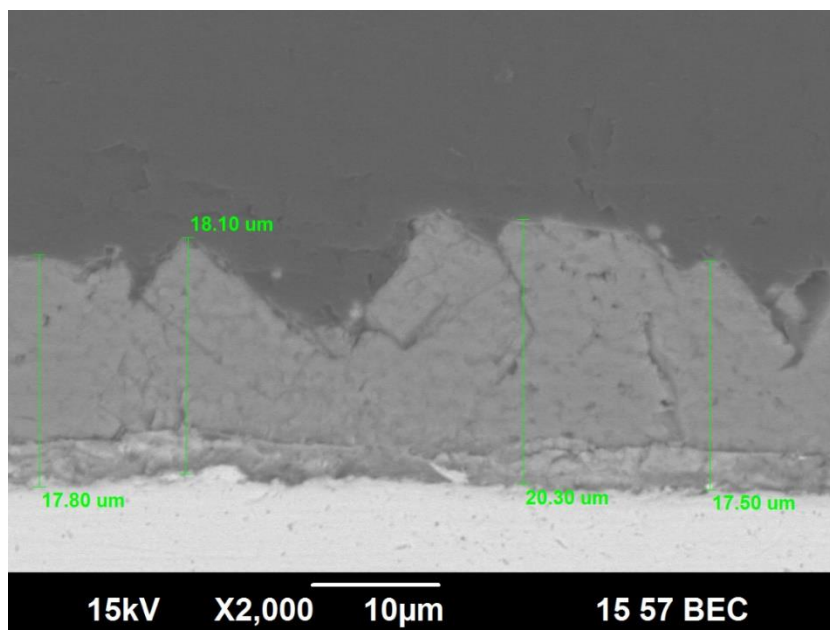


Figure 78. Cross-section analysis of the iron sulfide layer formed under dewing conditions. The thickness of the layer (combining outer and inner layer was $3 \pm 2 \mu\text{m}$).



Figure 79. EDS mapping cross-section analysis of the calcium carbonate layer formed as a scale.

6.3 Calcium Carbonate Layers with Substitutional Iron Atoms ($\text{Fe}_x\text{Ca}_y\text{CO}_3$)

6.3.1 Experimental Method

The objective for this step is to obtain an iron carbonate layer with substitutional cations that have the potential to create internal stresses. In order to achieve a short-term supersaturation with respect to calcite, the solution pH was temporarily increased up to 10.5 by injection of calcium hydroxide ($\text{Ca}(\text{OH})_2$). The experiment was conducted over different numbers of days in order to have a variation in the substitutional calcium along with the formed layer.

Table 11

Experimental Conditions to Develop an Iron Carbonate Layer with Substitutional calcium.

Parameter	Value
Temperature of solution / °C	80
Sparge gas	0.53 bar CO_2
Substrate material	API 5L X65 Steel
Solution	1 wt.% NaCl + $\text{Ca}(\text{OH})_2$
pH	6.2 ± 0.1
Duration	1, 2, 4, and 7 days

6.3.2 Results and Discussion

6.3.2.1 Layer Morphology

SEM images (Figure 80 and Figure 81) showed that the average thickness of the iron/calcium carbonate ($\text{Fe}_x\text{Ca}_y\text{CO}_3$; $x+y=1$) layer increased up to 25 μm .

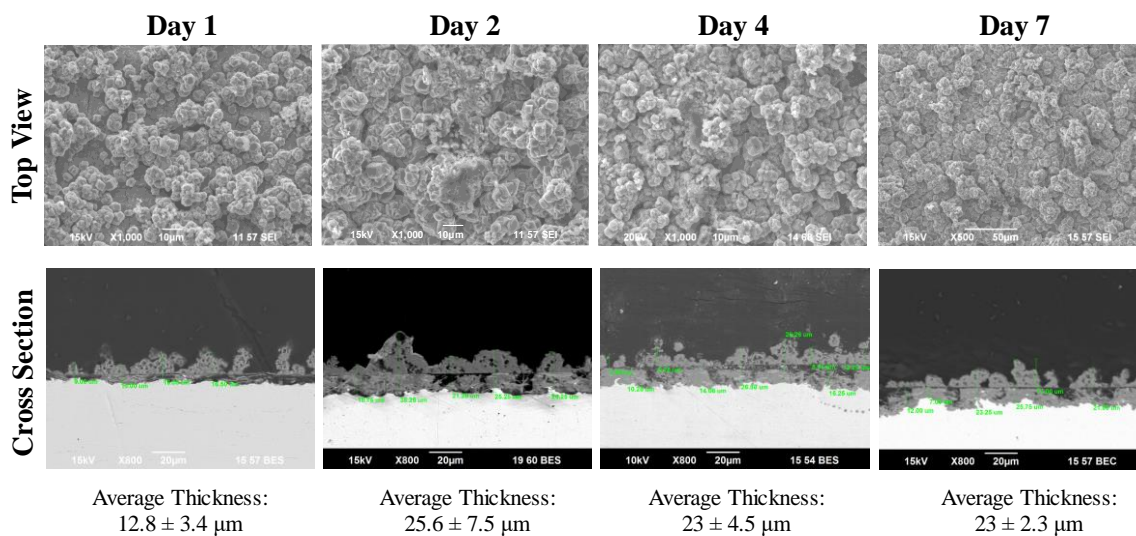


Figure 80. Top view and cross-section analysis of the iron/calcium carbonate layers developed after different times (days). The thickness of the layer increased up to 25 μm .

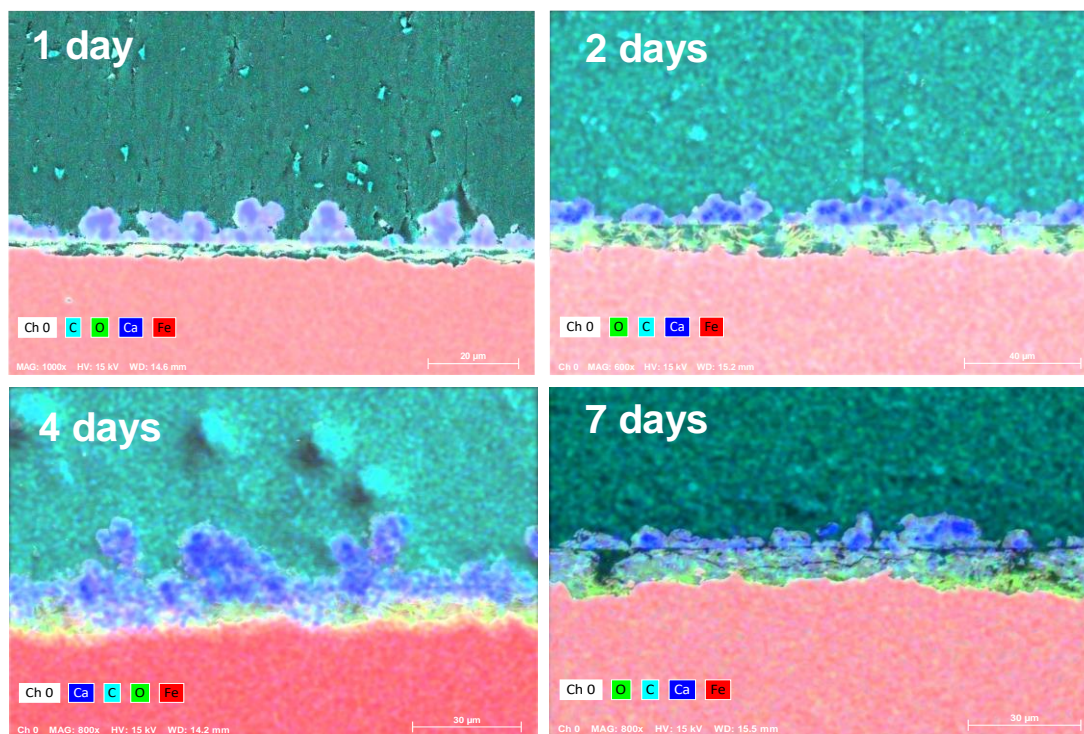


Figure 81. EDS mapping analysis of the cross section of the iron/calcium carbonate layer developed after different times (days).

6.3.3 Day 1 Specimen

6.3.3.1 Progressive Load Scratch Test

The progressive load scratch test was performed on the 1-day specimen to determine forces required for their cohesive and adhesive failure. Figure 82 shows the SEM images of the layer after the scratch test. The results indicated that the contact force of the apparatus (in the order of 0.1 mN) caused damage to the layer (the crystals were shattered, as shown by Figure 82a). As seen in Figure 82b, a groove was detected when the force reached *ca.* 12 mN. This value was related to the cohesive failure of the layer since there were no cracks detected. Continuing with the progressive increase in the loading force, at values close to 37 mN, the first detachment of the layer was detected, as shown by Figure 82c. Gross spallation of the adjacent scratch track resulted because of such failure. Figure 82d shows a continuous detachment of the layer, which was detected at values close to 170 mN of the normal force. Finally, the total removal of the layer was found at values in the order of 420 mN, as shown in Figure 82e. All detected forces are summarized in Table 12

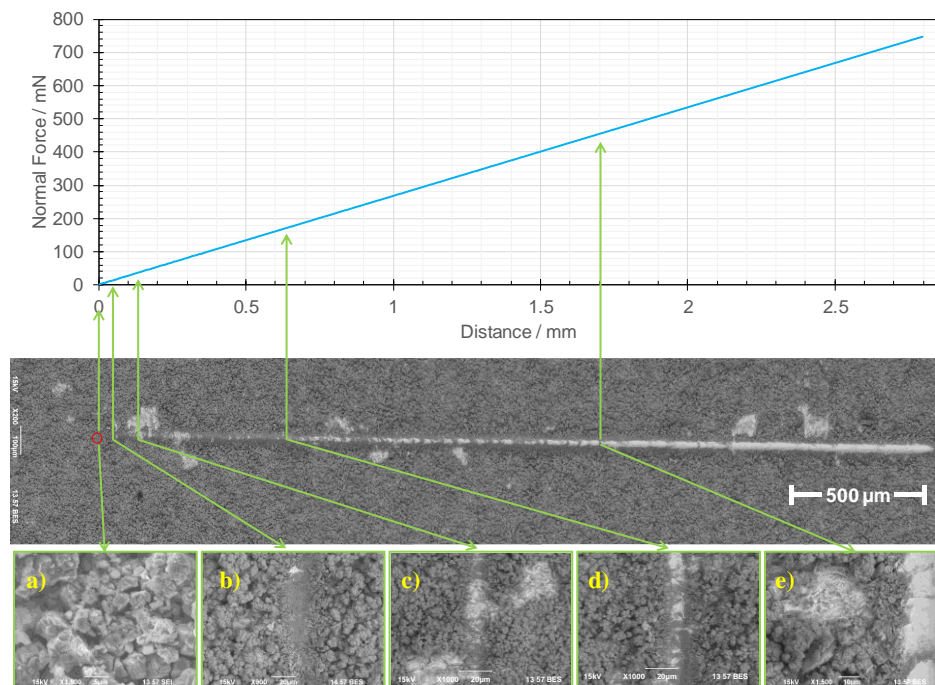


Figure 82. Progressive load scratch test on a $\text{Fe}_x\text{Ca}_y\text{CO}_3$ layer. Red circle: contact point of the scratch tester. Each arrow indicates the load and the zoomed image of the damage. Zoomed images: a) contact point of the scratch tester tip; b) cohesive failure; c) adhesive failure (first detachment); d) adhesive failure (continuous detachment); e) total removal of the layer.

Table 12

Failures Detected in the Progressive Load Scratch Test

Parameter	Value
Minimal force to produce damage	<0.1 mN
Cohesive failure (groove formation, no cracks detected)	12.2 ± 2 mN
Adhesive failure (first detachment)	36.5 ± 1.5 mN
Adhesive failure (continuous detachment)	172 ± 15 mN
Total removal	425 ± 25 mN

6.3.3.2 Profilometry

The profilometry on the scratch tested specimens was performed to corroborate the values obtained by the SEM analysis. Results of the depth left by the scratch tracks were compared with the average thickness of the sample to determine if the metal substrate was reached. For the day 1 sample, the average thickness was found to be $12.8 \pm 3.4 \mu\text{m}$, as shown in the cross-section analysis in Figure 80.

The cohesive failure point was analyzed first. The profilometry for this point is shown in Figure 83. Results indicate that the penetration of the scratch tester tip was of the order of $7 \mu\text{m}$. Since this value is smaller than the average thickness of the layer by a factor of two, it can be safely assumed that the substrate was not reached by the tip.

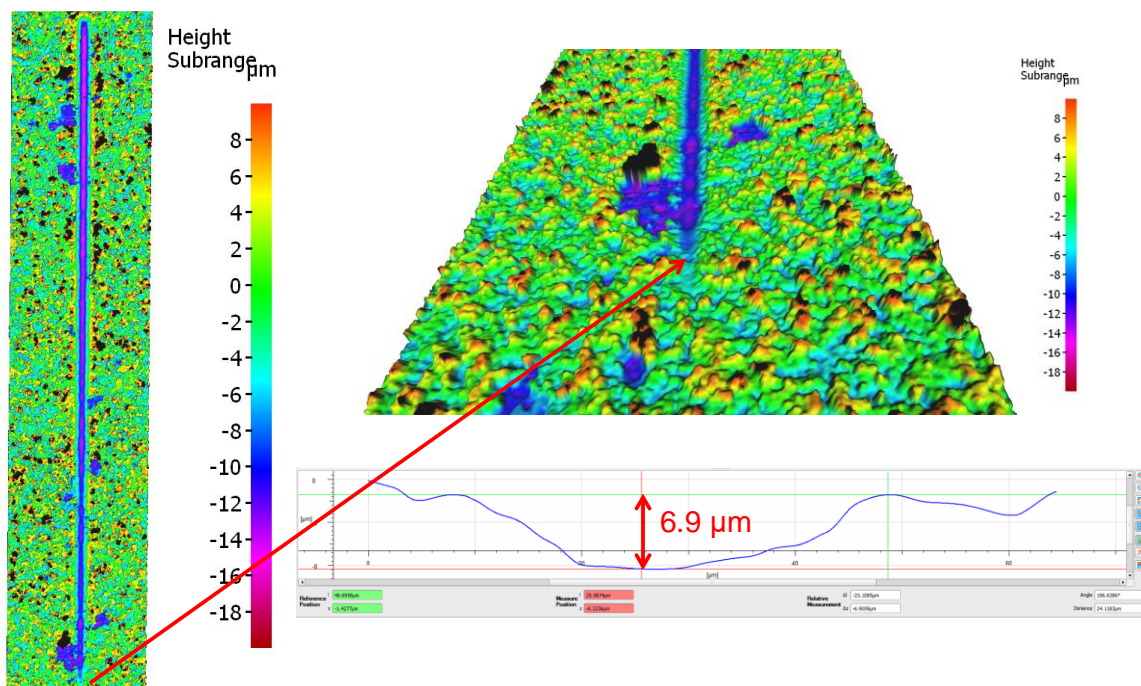


Figure 83. Specimen profilometry of the progressive load test for a range close to 12 mN. Detected penetration by the scratch tester tip: $\sim 7 \mu\text{m}$.

Following from the profilometry analysis, the next value explored was the first detachment of the layer (*ca.* 170 mN). Figure 84 shows that the indenter tip penetrated approximately 10 μm . This value overlaps the range of the measured thickness. Consequently, the metal substrate was likely reached at this stage.

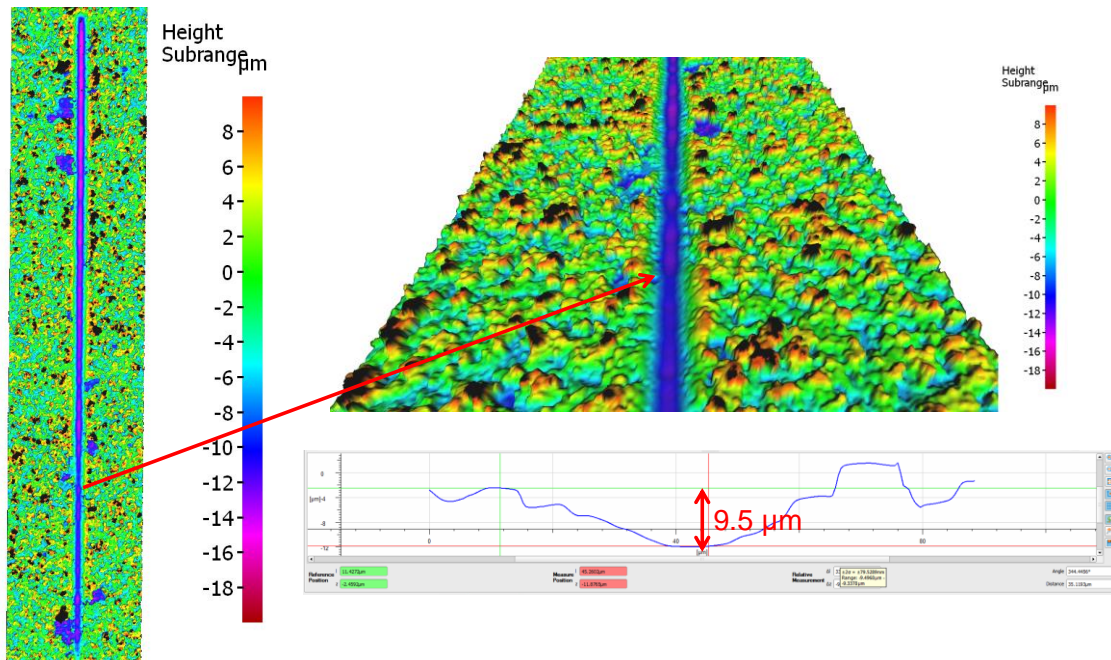


Figure 84. Specimen profilometry of the progressive load test for a range close to 170 mN. Detected penetration by the scratch tester tip: $\sim 10 \mu\text{m}$.

Finally, Figure 85 shows the the profilometry analysis performed in the scratch track where the normal force exceeded 420 mN (associated with the total removal of the layer). Results indicated that the penetration depth by the tip indenter was close to 14 μm . This value indicates that the metal substrate was reached by the scratch tip.

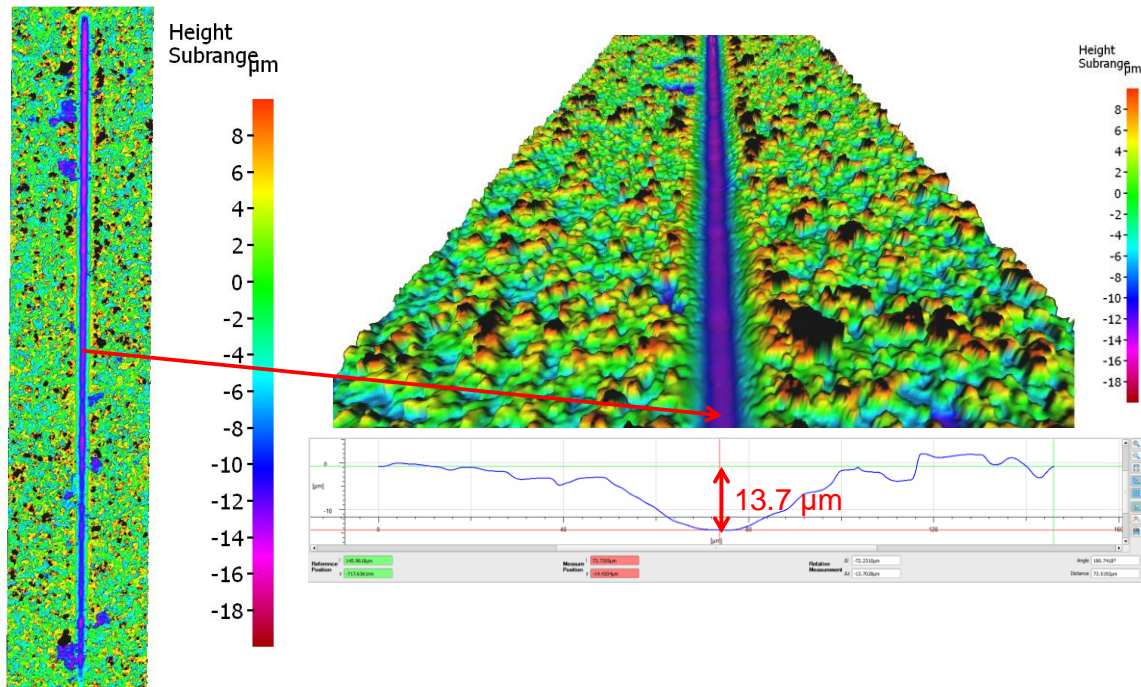


Figure 85. Specimen profilometry of the progressive load test for a range close to 420 mN. Detected penetration by the scratch tester tip: $\sim 14 \mu\text{m}$.

Once the forces associated with the cohesive and adhesive failure were confirmed by the profilometry test, the proposed mode of failure is presented.

6.3.3.3 Mode of Failure

According to ASTM C1624 [90], the comparative mode of failure can be related to gross spallation. Such a failure can be attributed to coatings that exhibit low adhesion strength or high residual stresses [90]. Therefore, the presence of calcium carbonate either decreases the adhesion strength of the iron carbonate layer, or there are more residual stresses induced by the presence of calcium as a substitutional element in the iron carbonate layer as shown in Figure 86.

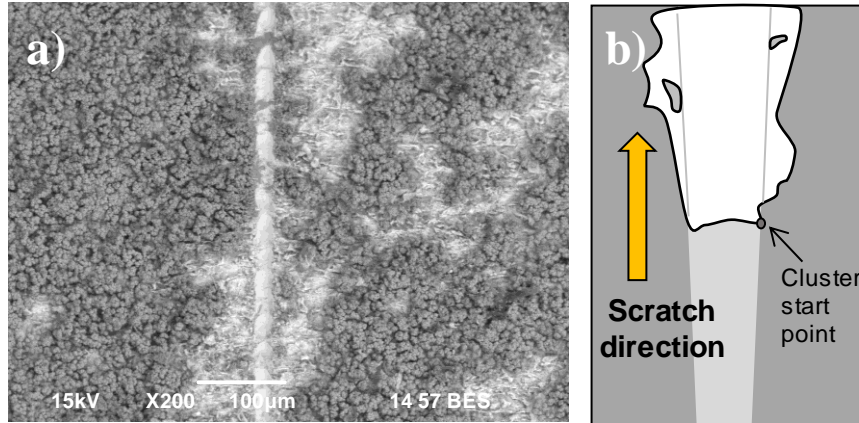


Figure 86. Gross spallation of the calcium/iron carbonate layer: a) SEM in backscatter mode of the calcium/iron carbonate layer; b) adaptation of the ASTM C1624 standard for gross spallation failure mode in ceramics coatings.

6.3.3.4 Constant Load Scratch Test

Constant load scratch tests were conducted to obtain cohesive and adhesive failure values at different normal loads close to the suspected failure values. Efforts conducted to determine the cohesive and adhesive values are presented in the next sections.

6.3.3.5 Cohesive Failure

Figure 87 shows the scratch tracks for different constant load tests. It was determined that cohesive failure values lie between 100 and 200 mN of normal load.

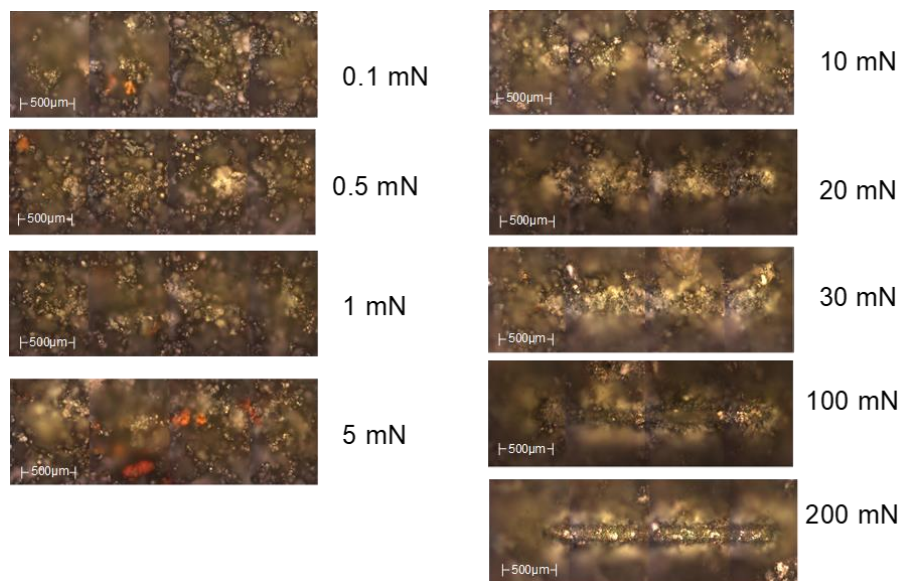


Figure 87. Constant load scratch test to corroborate cohesive failure.

Figure 88 shows the enlarged images of the 100 and 200 mN constant load scratch tracks. These images show that a buckling failure is detected. Such failure was corroborated by SEM, EDS and profilometry analysis.

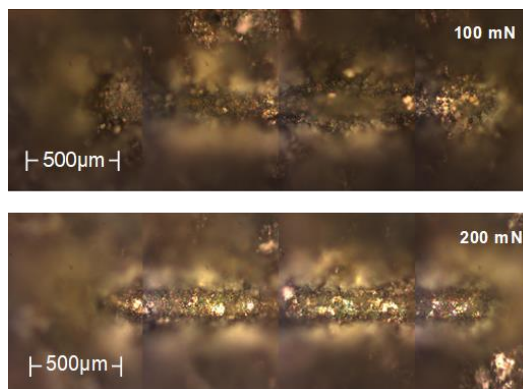


Figure 88. 100 and 200 mN constant load scratch test to corroborate cohesive failure.

6.3.3.6 SEM Analysis

Figure 89 shows the scratch track left by the 200 mN constant load scratch test. A zoom into the scratch track showed that the metal substrate was reached. Therefore, the adhesive failure was confirmed to be produced at this load.

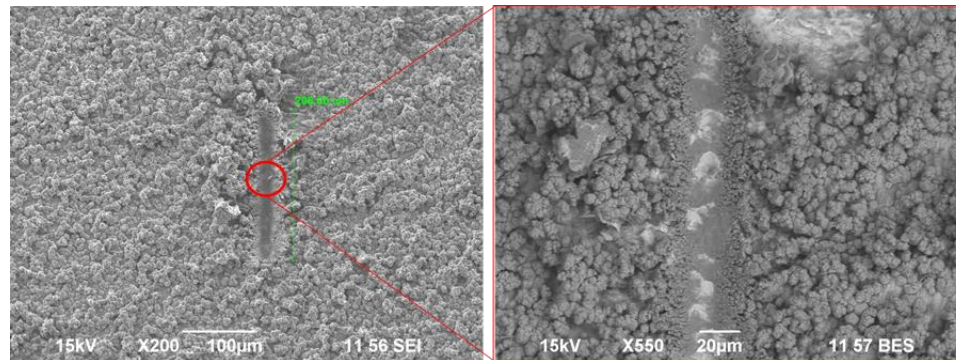


Figure 89. SEM image of the scratch track after the 200 mN constant load scratch test. The zoom of the image (right picture) shows the adhesive failure of the layer.

6.3.3.7 Profilometry

As secondary evidence of adhesive failure, profilometry showed that the penetration of the indenter was about 13 μm (Figure 90). Since the thickness of the layer was determined to be $12.8 \pm 3.4 \mu\text{m}$, it can be inferred that the substrate was reached in some parts of the specimen. This result is consistent with the profilometry analysis of the progressive load test.

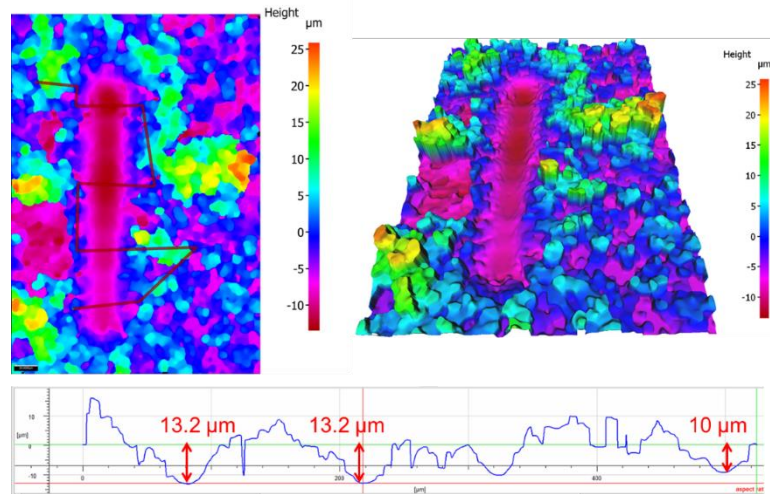


Figure 90. Profilometry of the scratch track after 200 mN constant load scratch test.

6.3.3.8 Cross-Section Analysis

Finally, a cross-section analysis by using SEM and EDS was conducted to corroborate the profilometry as shown in Figure 91. Results indicated that, at the point of the cross-section, the substrate was not reached. This result indicates that the inhomogeneity in the thickness of the corrosion product layer might play a factor in the interpretation of the results of progressive load scratch testing, arising from the importance of the constant load test since a bigger portion of the specimen is tested at a single force, reducing the impact of an inhomogeneous thickness [91].

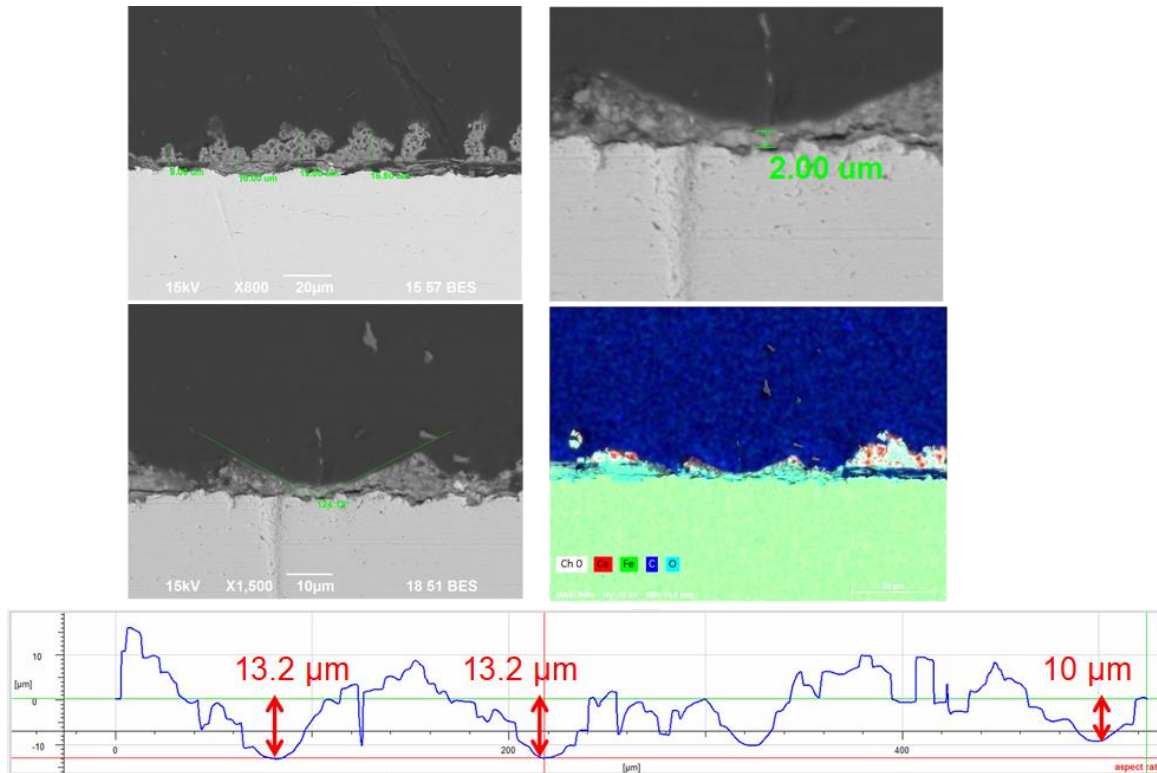


Figure 91. Cross-section analysis of the scratch track after the 200 mN constant load scratch test compared with the profilometry graph.

6.3.3.9 Adhesive Failure

The adhesive failure is associated with the total delamination of the layer was tested at high load forces where the failure was suspected to occur (between 300 and 600 mN). Figure 92 shows the tracks left by the constant load tests at different loading forces. It was observed that the delamination was at a point beyond 500 mN. Consequently, the efforts were focused on forces close to 600 mN.

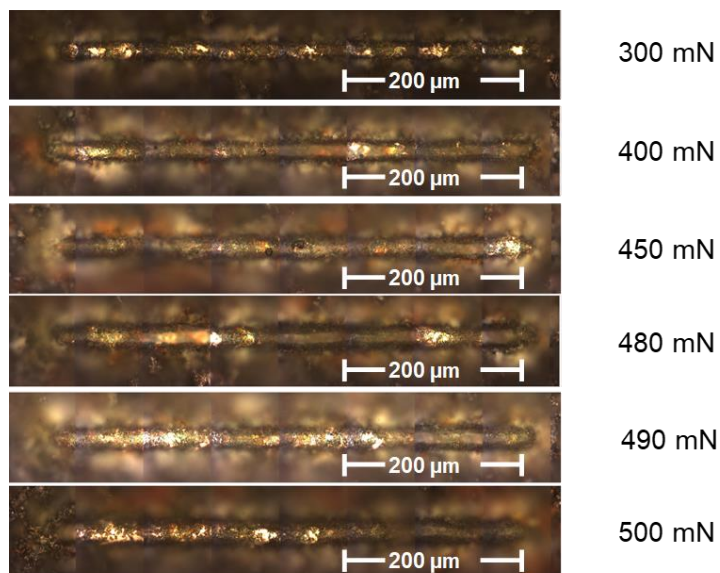


Figure 92. Scratch tracks of constant load test. Load forces from 300 to 500 mN.

Figure 93 shows that full delamination consistently occurred at 600 mN. Such a finding was corroborated with SEM, EDS, profilometry and cross-section analysis.

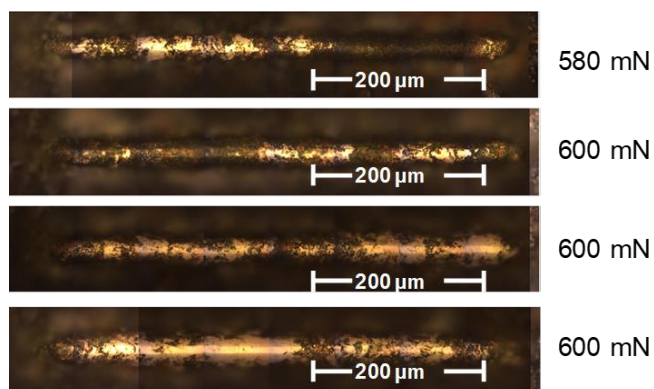


Figure 93. Scratch tracks of the constant load test. Total removal detected at load forces close to 600 mN.

6.3.3.10 SEM and EDS Analysis

Figure 94 shows an SEM image in backscatter mode of a scratch track after a 600 mN constant load scratch test. It can be observed that the scratch track consistently delaminated the corrosion product layer. Such an observation was supported by EDS analysis.

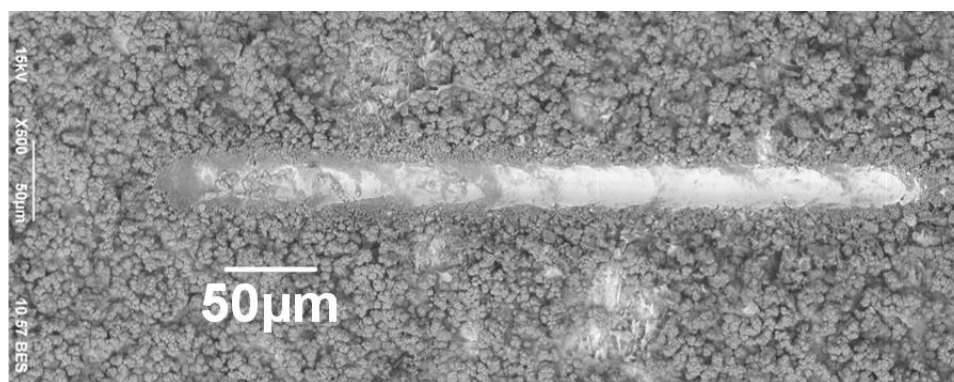


Figure 94. SEM in backscatter mode for a total removal scratch track. 600 mN constant load test.

Figure 95 shows point-analysis EDS on the zones where the layer was present and at the scratch track. After comparing the three zones, the elemental analysis showed that the percentage of iron in the scratch track is consistent with full delamination since more than 80 atom% was detected in that zone with no traces of calcium.

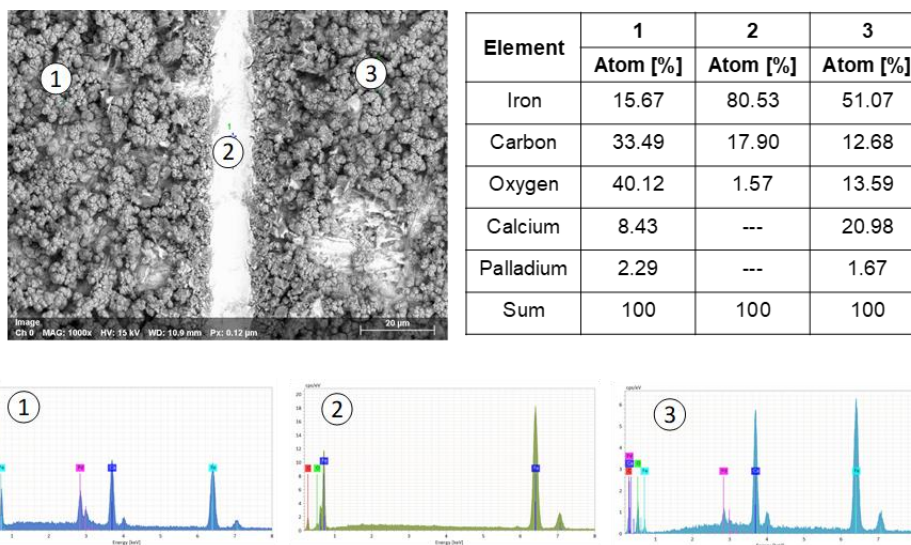


Figure 95. EDS analysis for a total removal scratch track. 600 mN constant load test.

6.3.3.11 Profilometry

Profilometry analysis was also a supportive analysis to determine if the indenter reached the metal substrate. From Figure 96, the depth of the scratch track indicated that the indenter regularly reached the substrate along the test.

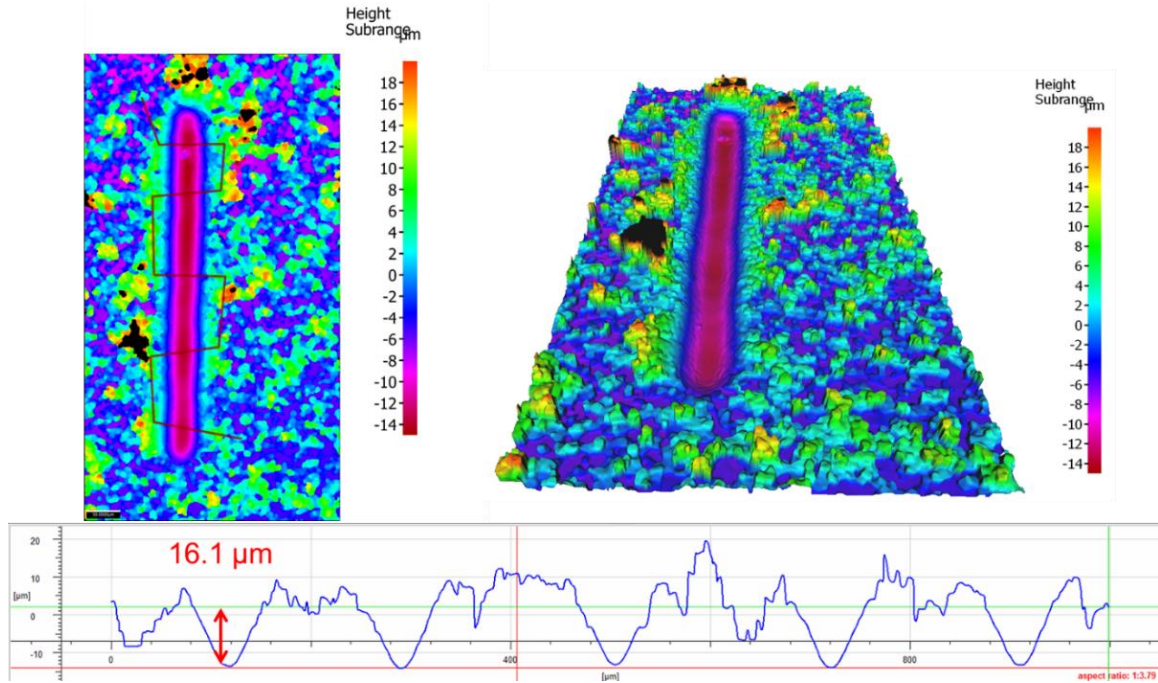


Figure 96. Profilometry for a total removal scratch track. 600 mN constant load test.

6.3.3.12 Cross-Section Analysis

The cross-section analysis shown in Figure 97 is another evidence of full delamination. SEM images demonstrated that the substrate was reached during the constant load scratch testing at 600 mN. EDS mapping analysis is also consistent with the full delamination argument.

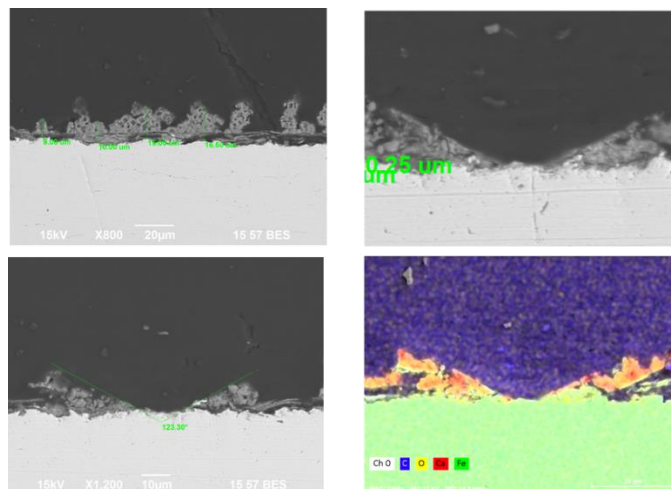


Figure 97. SEM and mapping EDS for the cross-section of a total removal scratch track. 600 mN constant load test.

6.3.3.13 *Vickers Indentation Fracture Tests*

Figure 98 shows the indentation mark and the crack propagation on a calcium carbonate layer with substitutional iron atoms. The fracture toughness was estimated to be $0.98 \pm 0.15 \text{ MPa m}^{1/2}$, a value close to the pure calcium carbonate. This result suggests that the fracture toughness of the calcium carbonate layer with substitutional atoms is dominated by the fracture toughness of the pure calcium carbonate.

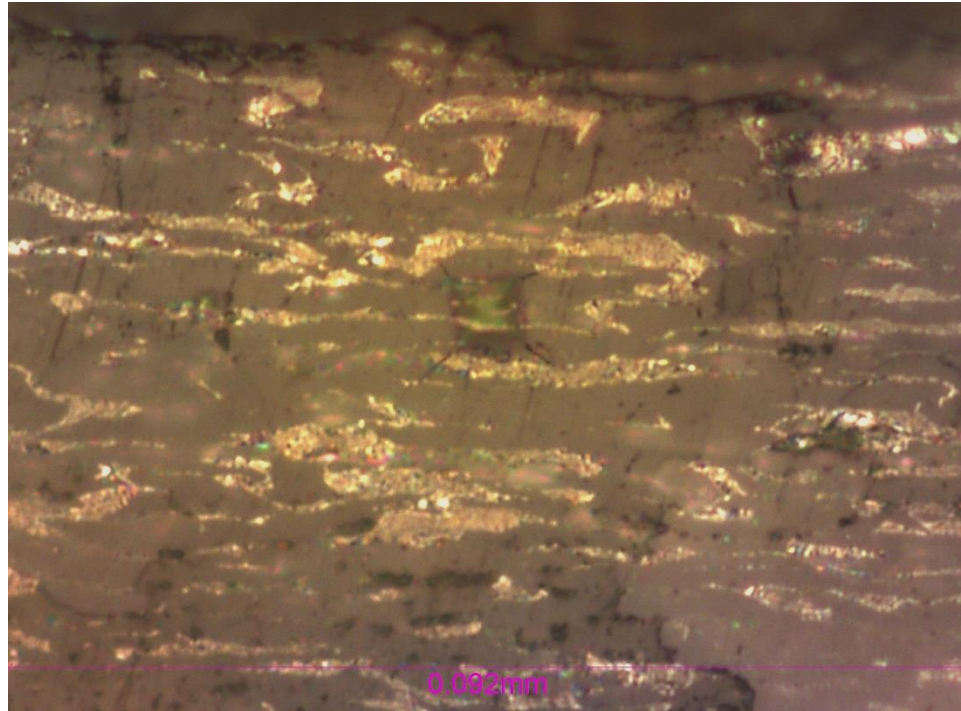


Figure 98. Vickers hardness mark and crack propagation on calcium carbonate with substitutional iron atoms.

6.4 Summary

6.4.1 Comparison of Mechanical Integrity of $FeCO_3$, $CaCO_3$ and $Fe_xCa_yCO_3$

6.4.1.1 Critical Shear Stress

Figure 99 shows the comparison of the critical shear stresses between a pure iron carbonate layer and iron/calcium carbonate layers grown over different numbers of days. The graph indicates that the presence of calcium significantly diminished the minimum shear stress to produce damage (by three orders of magnitude). This effect was observed from day 1 to day 4 layers. In day 7, the minimum force to produce damage in the layer increased by 2 orders of magnitude. This is consistent with the growth of iron carbonate, which is predominant over calcium carbonate at this stage. Regarding the cohesive failure

of a pure iron carbonate layer (associated with the minimum stress to produce erosion) the presence of calcium diminished the minimum force required. This can be explained by the presence of substitutional calcium, that produces internal stresses that reduces the erosion resistance by producing structural defects in the lattice [91].

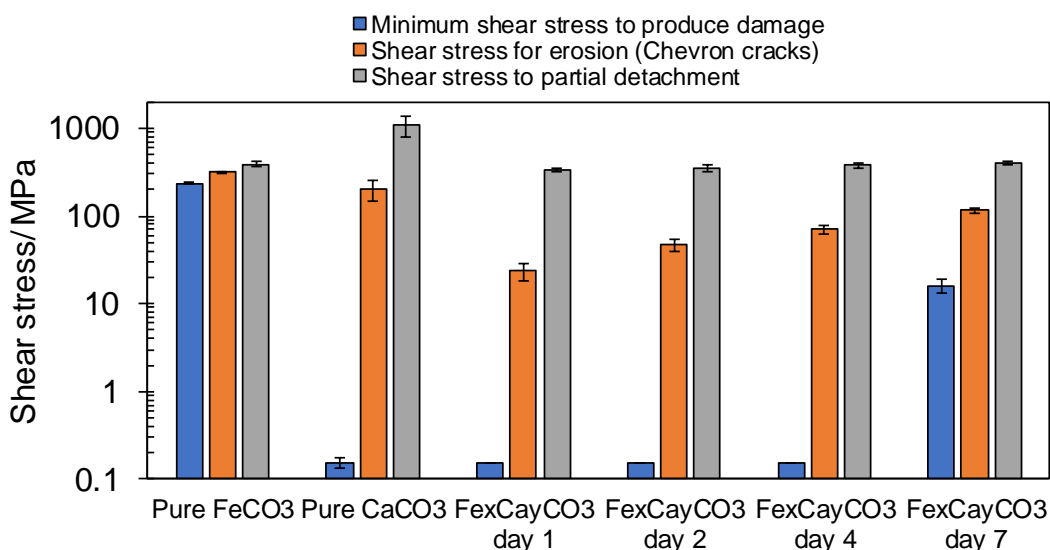


Figure 99. Mechanical integrity comparison between iron carbonate and iron calcium carbonate layers developed at different days. Minimum shear stress values to produce damage (blue bars), minimum shear stress to produce erosion (orange), and minimum shear stress to produce partial detachment of the layer (gray). Error bars: minimum and maximum values obtained.

Regarding the shear stress to produce complete damage, the pure calcium carbonate layer required a higher shear stress than the pure iron carbonate. This result indicates that the crystals of calcium carbonate have a higher adhesion to the iron substrate. It is also noted that the shear stress to produce complete damage in iron calcium carbonate layers was similar to the pure iron carbonate. Such a result suggests that the adhesive properties between the iron/calcium carbonate layer and the metal

substrate is governed by pure iron carbonate. This is consistent with the undermining effect: pure iron carbonate is formed at the interface of the calcium layer and the metal surface. Such a mechanism of formation would imply that the bond between the pure iron carbonate and the steel is the governing factor in the adhesion, which is consistent with the experimental results.

Finally, the minimum shear stress to produce erosion (associated with cohesive failure) would be related to the bond between the $\text{Fe}_x\text{Ca}_y\text{CO}_3$ and the pure FeCO_3 formed underneath. Since the bond between a layer with structural defects and one with no defects is generally weak [91], the more calcium carbonate at the mentioned interface, the less resistance the bond. In turn, this is consistent with the experimental results.

6.4.1.2 Fracture Toughness

Fracture toughness comparison is shown by Figure 100. It is noted that the estimated fracture toughness was increasing along the days in a similar fashion to the critical shear stress to produce damage in the layer. Such a result suggests that the fracture toughness is a function of the amount of substitutional iron in the calcium carbonate scale.

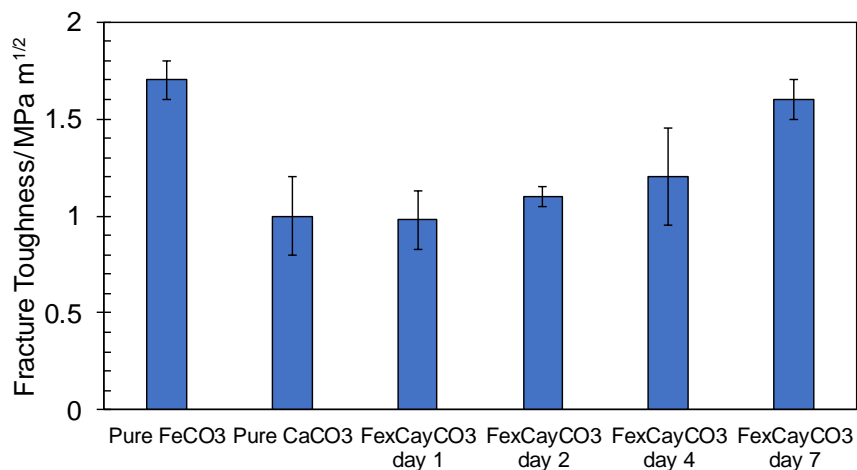


Figure 100. Fracture comparison between iron carbonate and iron calcium carbonate layers developed at different days.

However, there is no obvious relationship between the fracture toughness and the critical shear stresses previously determined, suggesting that there is no relationship between fracture toughness and critical shear stress to produce failures in the layers, as shown in Figure 101, Figure 102, and Figure 103.

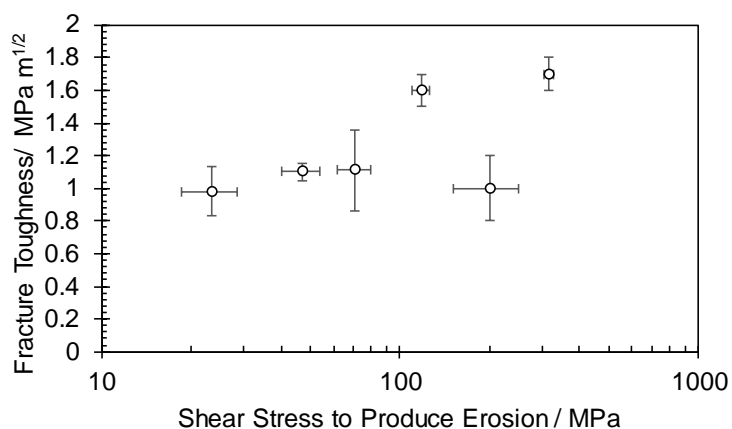


Figure 101. Correlation between minimum shear stress to produce erosion and fracture toughness in the calcium carbonate and iron carbonate layer developed at different days. Vertical error bars: maximum and minimum values of fracture toughness. Horizontal error bars: maximum and minimum values of shear stress.

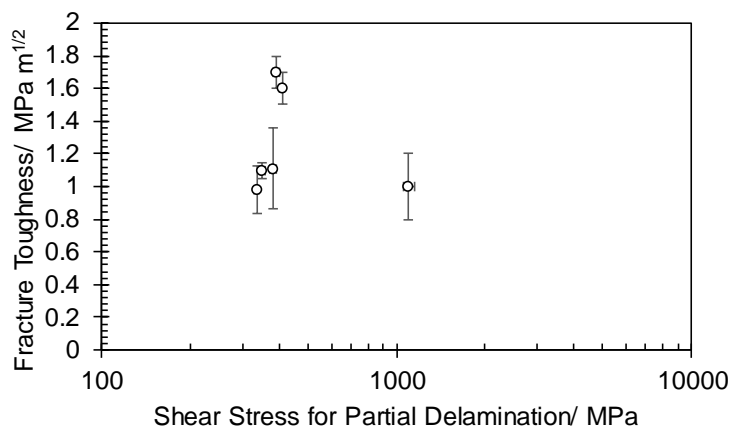


Figure 102. Correlation between minimum shear stress to produce partial delamination and fracture toughness in the calcium carbonate and iron carbonate layer developed at different days. Vertical error bars: maximum and minimum values of fracture toughness. Horizontal error bars: maximum and minimum values of shear stress.

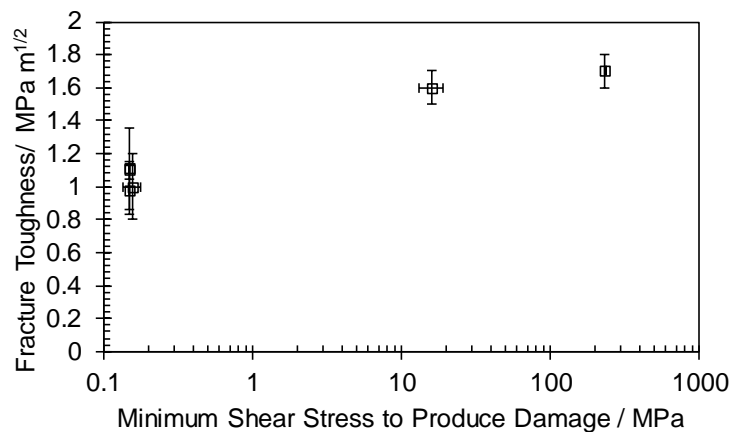


Figure 103. Correlation between minimum shear stress to produce damage and fracture toughness in the calcium carbonate and iron carbonate layer developed at different days. Vertical error bars: maximum and minimum values of fracture toughness. Horizontal error bars: maximum and minimum values of shear stress.

CHAPTER 7: CONCLUSIONS AND FUTURE WORK

7.1 Applicability of Tribology Science Techniques to Corrosion Science

- Scratch testing was successfully utilized to assess the mechanical integrity of an iron carbonate layer on mild steel and establish methods of comparison of forces, both qualitatively and quantitatively. Scratch test theory provided a quantitative tool to assess the adhesive forces of corrosion product layers in the form of shear stress.
- Within the theoretical approach, the approximation of Ollivier and Matthews [58] described the shear stress associated with the delamination of iron carbonate layers (*ca.* 400 MPa) and pure calcium carbonate (*ca.* 1.1 GPa) within a factor of 2. However, it failed to predict the delamination shear stress in corrosion product layers grown under dewing conditions.
 - The shear stress associated with the delamination of the iron carbonate layer from experimental tangential forces was *ca.* 125 kPa. The Ollivier and Mathews formulation yielded *ca.* 1.5 MPa. The relative error is higher than one order of magnitude.
 - In the case of iron sulfide, the delamination shear stress was determined experimentally as *ca.* 44 MPa, whereas the Ollivier and Matthews approach yielded 297 MPa. The relative error surpassed one order of magnitude.
- Consequently, iron carbonate scattered crystals, and iron sulfide layers at low normal forces do not obey the Ollivier and Matthews formulae. Such differences can be explained by the stress-relaxation theory of layers: layers grown under

aqueous environments undergo relaxation, whereas the layers grown under dewing conditions contains high residual intrinsic stresses. Such a postulate needs to be corroborated in future work.

7.2 Adhesive Properties of Layers Grown under Aqueous and Dewing Conditions

- Layer growth under dewing conditions exhibited significantly lower critical shear stress to show an adhesive failure (up to four orders of magnitude). Nevertheless, all of those stresses are two orders of magnitude above the shear stresses typically generated under normal transportation conditions in pipelines. Consequently, it is concluded that the shear stress exerted by fluids is unlikely to produce adhesive damage in the corrosion product layers. The adhesive failure of corrosion product layers is then hypothesized to be associated with thermal stresses due to different thermal expansion coefficients between the substrate and the layer.

7.3 Presence of Substitutional Calcium in Iron Carbonate Layers

- The presence of substitutional calcium in an iron carbonate layer compromised its mechanical integrity in terms of:
 - Shear stress needed to break the outer layer from the surface (minimum damage force)
 - Shear stress to produce cohesive failure.
 - Fracture toughness of the layer.
- The previous point can be explained by stating that the unit cell volume of the calcium carbonate is different than the iron carbonate. Therefore, the

substitutional calcium in the lattice can generate internal stresses that were manifested by the abovementioned mechanical characteristics of the layer.

- The shear stress to produce an adhesive failure was practically unaffected since iron carbonate was the predominant constituent in the interface between the steel and the corrosion product layer.
- Despite the fact that fracture toughness of calcium carbonate scales was seemingly affected in a similar fashion to the shear stress by the presence of substitutional iron atoms, there is no correlation between the fracture toughness and the critical shear stress to produce failure in the layer.
- Regarding the initial hypothesis about the cohesive and adhesive failures of iron carbonate layers affected by the presence of substitutional calcium, there is no conclusive evidence that the calcium carbonate diminishes the adhesive failure of an iron calcium carbonate layer but affects the cohesive strength of the iron carbonate layer.
- Despite the deleterious effect of the calcium on the adhesion properties and mechanical integrity of an iron carbonate layer, the forces required to compromise the mechanical integrity of a carbonate layer (MPa) are orders of magnitude above shear stresses commonly found in transmission pipelines (Pa).
Consequently, the shear stress exerted by a transported fluid by itself is unlikely to produce adhesive damage.

7.4 Recommendations and Future Work

- Lateral force microscopy (LFM) was applied for the determination of the adhesion forces of a single iron carbonate crystal to a steel substrate. However, the conversion of the force obtained to shear stress is dubious since it was not possible to determine the actual contact between the tip and the crystals. Moreover, the range of forces applied by LFM were insufficient to study the bonding forces between fully developed iron carbonate layers and the steel surface.
- In order to successfully apply lateral force microscopy (LFM) a tip with higher spring constants and a larger geometry are needed. The crystals of iron carbonate are of the order of 2 – 20 μm (depending on the environmental conditions from which they are precipitated). Consequently, the AFM probe tip needs to be as large as the crystals to be removed.
- The use of the scratch test gives values of tangential forces needed for delamination as the force balance indicates that the frictional force measures the cumulative effect of the possible sources of stress affecting the adhesion of the layers. The differences between the stresses calculated from measured frictional forces and the Ollivier and Matthews approach were postulated to be caused by intrinsic stresses in the layers. However, a more in-depth study is needed in order to effectively separate the components of the forces associated with the adhesion of corrosion product layers. Thermal stresses due to different thermal expansions of the substrate and the precipitated layer need to be taken into consideration.

Techniques such as the bending cantilever and the use of Stoney's equation are strongly suggested to determine the stresses associated with epitaxial growth of corrosion product layers [70].

REFERENCES

- [1] R. M. Baldwin, "Black Powder Problem Will Yield To Understanding , Planning," *Pipeline Gas Ind.*, vol. 1, pp. 109–112, 1999.
- [2] A. M. Sherik, A. Rasheed, and A. Jabran, "Effect of sales gas pipelines black powder sludge on the corrosion of carbon steel," in *NACE Corrosion Conference*, 2011, no. 11087.
- [3] J. S. Smart, "Black powder movement in gas pipelines," in *NACE Corrosion Conference*, 2011, no. 11089.
- [4] M. Azadi, A. Mohebbi, S. Soltaninejad, and F. Scala, "A case study on suspended particles in a natural gas urban transmission and distribution network," *Fuel Process. Technol.*, vol. 93, no. 1, pp. 65–72, 2012.
- [5] G. Svenningsen, R. Nyborg, A. Sherik, and A. L. Lewis, "Black powder formation in thin water layers under stagnant conditions," in *NACE Corrosion Conference*, 2011, no. 11084.
- [6] S. Ramachandran, K. Cattanaach, V. Jovancicevic, and A. Sherik, "Development of a novel test procedure to understand and mitigate black powder formation in sales gas pipelines," in *NACE Corrosion Conference*, 2010, no. 10186.
- [7] P. Zhang, Z. Han, C. Ye, and L. Zhu, "Problems and mitigation experiences with black powder inside of the long-distance natural gas pipelines," in *NACE Corrosion Conference*, 2012, no. 1589.
- [8] A. M. Sherik, S. R. Zaidi, E. V. Tuzan, and J. P. Perez, "Black powder in gas transmission systems," in *NACE Corrosion Conference*, 2008, no. 08415.
- [9] A. M. Sherik, A. L. Lewis, A. H. Rasheed, and A. A. Jabran, "Black powder inhibitors - performance Study," in *NACE Corrosion Conference*, 2011, no. 11094.
- [10] D. Sander, "Stress measurements of atomic layers and at surfaces," in *Stress and Strain in Epitaxy: Theoretical Concepts, Measurements and Applications*, M. Hanbucken and J.-P. Deville, Eds. New York: Elsevier, 2001, pp. 221–242.
- [11] P. M. Marcus, "Epitaxial strain and epitaxial bending," *Surf. Sci.*, vol. 366, no. 1, pp. 219–227, 1996.
- [12] H. Ibach, "The role of surface stress in reconstruction, epitaxial growth and stabilization of mesoscopic structures," *Surf. Sci. Rep.*, vol. 29, no. 5–6, pp. 195–263, 1997.
- [13] V. Fajardo, C. Canto, B. Brown, D. Young, and S. Nesic, "The effect of acetic acid on the integrity of protective iron carbonate layers in CO₂ corrosion of mild steel," in *NACE Corrosion Conference*, 2008, no. 08333.

- [14] E. Gulbrandsen, "Acetic acid and carbon dioxide corrosion of carbon steel covered with iron carbonate," in *NACE Corrosion Conference*, 2007, no. 07322.
- [15] G. Schmitt, M. Mueller, M. Papenfuss, and E. Strobel-Effertz, "Understanding localized CO₂ corrosion of carbon steel from physical properties of iron carbonate scales," in *NACE Corrosion Conference*, 1999, no. 38.
- [16] S. D. Zhu, G. S. Zhou, J. Miao, R. Cai, and J. F. Wei, "Mechanical properties of CO₂ corrosion scale formed at different temperatures and their relationship to corrosion rate," *Corros. Eng. Sci. Technol.*, vol. 47, no. 3, pp. 177–181, 2012.
- [17] T. Namazu, Y. Isono, and T. Tanaka, "Evaluation of size effect on mechanical properties of single crystal silicon by nanoscale bending test using AFM," *J. Microelectromechanical Syst.*, vol. 9, no. 4, pp. 450–459, 2000.
- [18] D. A. Jones, *Principles and prevention of corrosion*, vol. 14. MacMillan, 1992.
- [19] M. Nordsveen and S. Nešić, "A mechanistic model for carbon dioxide corrosion of mild steel in the presence of protective iron carbonate films — part 1 : theory and verification," *Corrosion*, vol. 59, no. 5, pp. 443–456, 2003.
- [20] E. Remita, B. Tribollet, E. Sutter, V. Vivier, F. Ropital, and J. Kittel, "Hydrogen evolution in aqueous solutions containing dissolved CO₂: Quantitative contribution of the buffering effect," *Corros. Sci.*, vol. 50, no. 5, pp. 1433–1440, 2008.
- [21] C. de Waard and D. E. Milliams, "Prediction of carbonic acid corrosion in natural gas pipelines," in *First International Conference on the Internal and External Protection of Pipes*, 1975, no. 1, pp. 1–8.
- [22] S. Nešić and K. Lee, "A mechanistic model for carbon dioxide corrosion of mild steel in the presence of protective iron carbonate films-Part 3: Film growth model," *Corrosion*, vol. 59, no. 7, pp. 616–628, 2003.
- [23] S. Nešić, "A mechanistic model for carbon dioxide corrosion of mild steel in the presence of protective iron carbonate films — Part 2 : a numerical experiment," *Corros. Sci.*, vol. 59, no. 6, pp. 489–497, 2003.
- [24] W. Sun, "Kinetics of iron carbonate and iron sulfide scale formation in CO₂/H₂S corrosion," Ph.D. Dissertation, Dept. Chem. and Biomolec. Eng., Ohio University, Athens, OH, 2006.
- [25] W. Sun, S. Nešić, and R. C. Woollam, "The effect of temperature and ionic strength on iron carbonate (FeCO₃) solubility limit," *Corros. Sci.*, vol. 51, no. 6, pp. 1273–1276, 2009.
- [26] S. Nešić, "Key issues related to modelling of internal corrosion of oil and gas pipelines – A review," *Corros. Sci.*, vol. 49, no. 12, pp. 4308–4338, Dec. 2007.

- [27] H. Mansoori, D. Young, B. Brown, and M. Singer, "Influence of calcium and magnesium ions on CO₂ corrosion of carbon steel in oil and gas production systems - A review," *J. Nat. Gas Sci. Eng.*, vol. 59, pp. 287–296, 2018.
- [28] Y. Zheng, "Electrochemical mechanism and model of H₂S corrosion of carbon steel," Ph.D. Dissertation, Dept. Chem. and Biomolec. Eng., Ohio University, Athens, OH, 2014.
- [29] Y. Zheng, B. Brown, and S. Nešić, "Electrochemical study and modeling of H₂S corrosion of mild steel," *Corrosion*, vol. 70, no. 4, pp. 351–365, 2014.
- [30] N. Yaakob, M. Singer, and D. Young, "Top of the line corrosion behavior in highly sour environments: effect of the gas/steel temperature," in *NACE Corrosion Conference*, 2014, no. 3807.
- [31] A. Camacho, M. Singer, B. Brown, and S. Nesic, "Top of the line corrosion in H₂S/CO₂ nvironment," in *NACE Corrosion Conference*, 2008, no. 08470.
- [32] Y. Yang, B. Brown, and S. Nesic, "Mechanical Strength and Removal of a Protective Iron Carbonate Layer Formed on Mild Steel in CO₂ Corrosion," in *NACE Corros. Conf.*, no. 10383, pp. 1–19, 2010.
- [33] G. Schmitt, "Fracture mechanical properties of CO₂ corrosion product scales and their relation to localized corrosion," in *Corrosion*, 1996, no. 9.
- [34] J. Robertson and M. I. Manning, "Limits to adherence of oxide scales," *Mater. Sci. Technol.*, vol. 6, no. 1, pp. 81–92, 1990.
- [35] P. J. Burnett and D. S. Rickerby, "The Mechanical Properties of Wear-Resistant Coatings I: Modelling of Hardness Behaviour," *Thin Solid Films*, vol. 148, pp. 41–50, 1987.
- [36] P. J. Burnett and D. S. Rickerby, "The mechanical properties of wear-resistant coatings II: experimental studies and interpretation of hardness," *Thin Solid Films*, vol. 148, pp. 51–65, 1987.
- [37] D. A. King and D. P. Woodruff, Eds., *The Chemical Physics of Solid Surfaces*, 1st ed., vol. 8, no. 9. Elsevier, 1997.
- [38] J. A. Floro *et al.*, "The dynamic competition between stress generation and relaxation mechanisms during coalescence of Volmer-Weber thin films," *J. Appl. Phys.*, vol. 89, no. 9, pp. 4886–4897, 2001.
- [39] W. Nix, "Mechanical properties of thin films," *Metall. Mater. Trans. A*, vol. 20, no. November, pp. 2217–2245, 1989.
- [40] B. W. Sheldon, A. Rajamani, A. Bhandari, E. Chason, S. K. Hong, and R. Beresford, "Competition between tensile and compressive stress mechanisms during Volmer-Weber growth of aluminum nitride films," *J. Appl. Phys.*, vol. 98, no. 4, 2005.

- [41] J. W. Hutchinson, “Stresses and failures modes in thin films and multilayers,” *Notes for a DCAMM Course*. Division of Engineering and Applied Science, Harvard University, Cambridge, MA, pp. 1–3, 1996.
- [42] M. F. Doerner and W. D. Nix, “Stresses and deformation processes in thin films on substrates,” *Crit. Rev. Solid State Mater. Sci.*, vol. 14, no. 3, pp. 225–268, 2012.
- [43] I. Bryan *et al.*, “Surface kinetics in AlN growth: A universal model for the control of surface morphology in III-nitrides,” *J. Cryst. Growth*, vol. 438, pp. 81–89, 2016.
- [44] L. Mordfin, Ed., *Mechanical Relaxation of Residual Stresses*. Baltimore, MD: ASTM International, 1988.
- [45] D. Chicot and a Tricoteaux, “Mechanical properties of ceramics by indentation: principle and applications,” *Ceram. Mater.*, pp. 115–153, 2010.
- [46] S. J. Bull, “Failure mode maps in the thin film scratch adhesion test,” *Tribol. Int.*, vol. 30, no. 7, pp. 491–498, 1997.
- [47] P. J. J. Burnett and D. S. S. Rickerby, “The Relationship Between Hardness and Scratch Adhesion,” *Thin Solid Films*, vol. 154, no. 154, pp. 403–416, Nov. 1987.
- [48] D. Chicot, G. Duarte, A. Tricoteaux, B. Jorgowski, A. Leriche, and J. Lesage, “Vickers Indentation Fracture (VIF) modeling to analyze multi-cracking toughness of titania, alumina and zirconia plasma sprayed coatings,” *Mater. Sci. Eng. A*, vol. 527, no. 1–2, pp. 65–76, 2009.
- [49] S. J. Bull, D. S. Rickerby, A. Matthews, A. Leyland, A. R. Pace, and J. Valli, “The use of scratch adhesion testing for the determination of interfacial adhesion: The importance of frictional drag,” *Surf. Coatings Technol.*, vol. 36, no. 1–2, pp. 503–517, 1988.
- [50] P. J. Burnett and D. S. Rickerby, “The Scratch Adhesion Test: an Elastic-Plastic Indentation Analysis,” *Thin Solid Films*, vol. 157, pp. 233–254, 1988.
- [51] S. Kuiry, “Advanced Scratch Testing for Evaluation of Coatings,” Technical Note on Tribology, Campbell, CA, 2012.
- [52] C. Weaver, “Adhesion of thin films,” *J. Vac. Sci. Technol.*, vol. 12, no. 1, pp. 18–25, Jan. 1975.
- [53] E. . Bull, S J ; Berasategui, “An overview of the potential of quantitative coating adhesion measurements by scratch testing,” *Tribol. Int.*, vol. 39, no. February, pp. 136–165, 2006.
- [54] S. J. Bull and D. S. Rickerby, “New developments in the modelling of the hardness and scratch adhesion of thin films,” *Surf. Coatings Technol.*, vol. 42, no. 2, pp. 149–164, 1990.

- [55] D. Tabor, "Friction, lubrication, and wear," in *Mechanical Design Handbook*, Second Edi., Cambridge, England: McGraw-Hill, 2006, pp. 1–26.
- [56] H. J. Butt and M. Kappl, *Surface and Interfacial Forces*, Second Edi. Wiley-VCH Verlag GmbH & Co., 2017.
- [57] J. S. Mcfarlane and D. Tabor, "Relation between friction and adhesion," *Proc. R. Soc. London. Ser. A. Math. Phys. Sci.*, vol. 202, no. 1069, pp. 244–253, 2006.
- [58] B. Ollivier and A. Matthews, "Adhesion of diamond-like carbon films on polymers: an assessment of the validity of the scratch test technique applied to flexible substrates," *J. Adhes. Sci. Technol.*, vol. 8, no. 6, pp. 651–662, Jan. 1994.
- [59] P. Benjamin and C. Weaver, "Measurement of adhesion of thin films," *Proc. R. Soc. London. Ser. A. Math. Phys. Sci.*, vol. 254, no. 1277, pp. 163–176, Feb. 1960.
- [60] A. J. Perry, "The adhesion of chemically vapour-deposited hard coatings to steel—the scratch test," *Thin Solid Films*, vol. 78, no. 1, pp. 77–94, 1981.
- [61] M. T. Laugier, "Adhesion of TiC and TiN coatings prepared by chemical vapour deposition on WC-Co-based cemented carbides," *J. Mater. Sci.*, vol. 21, no. 7, pp. 2269–2272, 1986.
- [62] M. T. Laugier, "An energy approach to the adhesion of coatings using the scratch test," *Thin Solid Films*, vol. 117, no. 4, pp. 243–249, 1984.
- [63] T. L. Anderson, *Fracture mechanics: fundamentals and applications*. CRC press, 2017.
- [64] A. A. Griffith, "The Phenomena of Rupture and Flow in Solids," *Philos. Trans. R. Soc. London*, vol. 221, pp. 163–198, 1921.
- [65] K. Gao *et al.*, "Mechanical properties of CO₂ corrosion product scales and their relationship to corrosion rates," *Corros. Sci.*, vol. 50, no. 10, pp. 2796–2803, 2008.
- [66] E. Rocha-Rangel, "Fracture toughness determinations by means of indentation fracture," in *Nanocomposites with Unique Properties and Application in Medicine and Industry*, 1st ed., J. Cuppoletti, Ed. Intech, 2011, p. 360.
- [67] H. A. Richard and M. Sander, "Fundamentals of fracture mechanics," in *Solid Mechanics and its Applications*, 2016.
- [68] B. R. Lawn and D. B. Marshall, "Hardness, toughness, and brittleness: an indentation analysis," *J. Am. Ceram. Soc.*, vol. 62, no. 7, pp. 347–350, 1978.
- [69] G. D. Quinn and R. C. Bradt, "On the Vickers indentation fracture toughness Test," *J. Am. Ceram. Soc.*, vol. 90, no. 3, pp. 673–680, 2007.
- [70] X. Feng, Y. Huang, and a. J. Rosakis, "On the Stoney Formula for a Thin Film/Substrate System With Nonuniform Substrate Thickness," *J. Appl. Mech.*, vol. 74, no. 6, p. 1276, 2007.

- [71] W. Li, Y. Xiong, B. Brown, K. E. Kee, and S. Nestic, "Measurement of wall shear stress in multiphase flow and its effect on protective FeCO_3 corrosion product layer removal," in *NACE Corrosion Conference*, 2015, no. 5922.
- [72] Y. Xiong, B. Brown, B. Kinsella, S. Nestic, and A. Pailleret, "AFM studies of the adhesion properties of surfactant corrosion inhibitor films," *NACE Corros. Conf.*, no. 2521, pp. 1–22, 2013.
- [73] J. Han, D. Young, H. Colijn, A. Tripathi, and S. Nešić, "Chemistry and Structure of the Passive Film on Mild Steel in CO_2 Corrosion Environments," *Ind. Eng. Chem. Res.*, vol. 48, no. 13, pp. 6296–6302, 2009.
- [74] D. A. López, W. H. Schreiner, S. R. de Sánchez, and S. N. Simison, "The influence of inhibitors molecular structure and steel microstructure on corrosion layers in CO_2 corrosion," *Appl. Surf. Sci.*, vol. 236, no. 1–4, pp. 77–97, Sep. 2004.
- [75] Y. Xiong, S. Nestic, and B. Brown, "Probing Adhesion Layers at the Interface using Atomic Force Microscopy," Corrosion Center Joint Industry Project, Advisory Board Meeting, Ohio University, Athens, OH, March, 2012.
- [76] M. Ohring, *Materials Science of Thin Films, Second Edition*. 2001.
- [77] J. E. Sader, J. W. M. Chon, and P. Mulvaney, "Calibration of rectangular atomic force microscope cantilevers," *Rev. Sci. Instrum.*, vol. 70, no. 10, pp. 3967–3969, 1999.
- [78] J. E. Sader *et al.*, "Spring constant calibration of atomic force microscope cantilevers of arbitrary shape," *Rev. Sci. Instrum.*, vol. 83, no. 10, 2012.
- [79] U. D. Schwarz, P. Köster, R. Wiesendanger, P. Koster, and R. Wiesendanger, "Quantitative analysis of lateral force microscopy experiments," *Rev. Sci. Instrum.*, vol. 67, no. 7, pp. 2560–2567, 1996.
- [80] Y. Liu, T. Wu, and D. F. Evans, "Lateral force microscopy study on the shear properties of self-assembled monolayers of dialkylammonium surfactant on mica," *Langmuir*, vol. 10, no. 7, pp. 2241–2245, 1994.
- [81] R. J. Cannara, M. Eglin, and R. W. Carpick, "Lateral force calibration in atomic force microscopy: A new lateral force calibration method and general guidelines for optimization," *Rev. Sci. Instrum.*, vol. 77, no. 5, p. 11, 2006.
- [82] M. Tortonese, "Cantilevers and tips for atomic force microscopy," *IEEE Eng. Med. Biol. Mag.*, vol. 16, no. 2, pp. 28–33, 1997.
- [83] S. N. Manonov and M.-H. Whangbo, *Surface Analysis with STM and AFM*, vol. 1. Weinheim, Germany: VCH, 1997.
- [84] ASTM, "Standard Test Method for Adhesion Strength and Mechanical Failure Modes," *ASTM Int.*, 2010.

- [85] M. Colahan and D. Young, "PI Phase I Progress Report," ICMT, Ohio University, PI Project, Athens, OH, 2015.
- [86] E. Anyanwu, "The Effect of Flow on the Development and Retention of Iron Sulfide Corrosion Product Layers," Ohio University, 2019.
- [87] B. Lafuente, R. T. Downs, H. Yang, and N. Stone, "RRUFFTM Project," *The power of databases: the RRUFF project. Highlights in Mineralogical Crystallography*, T Armbruster and R M Danisi, eds., 2015. .
- [88] G. Svenningsen, M. Foss, R. Nyborg, A. Sherik, and A. L. Lewis, "Laboratory simulation of black powder formation in flowing gas with water condensation," *NACE Corros. Conf.*, no. 11086, pp. 1–11, 2011.
- [89] R. Nyborg, A. Dugstad, and T. G. M. Ret, "Top of Line Corrosion with High CO₂ and Traces of H₂S," *NACE Corros. Conf.*, no. 09283, pp. 1–11, 2009.
- [90] ASTM, "Standard Test Method for Adhesion Strength and Mechanical Failure Modes of," *ASTM Int.*, vol. C1624-05, pp. 1–29, 2010.
- [91] B. Bushan, *Handbook of Micro/Nanotribology*, 1st Editio. Boca Raton, FL: CRC Press LLC, 1999.
- [92] W. D. J. Callister, *Fundamentals of Materials Science and Engineering*. 2001.
- [93] Harry Chandler, *Heat Treater's Guide: Practices and Procedures for Irons and Steels*. 1995.
- [94] The Materials Information Society, *ASM Handbook Volume 3 - Alloy Phase Diagrams*. 1992.
- [95] R. Abbaschian, L. Abbaschian, and R. E. Reed-Hill, *Physical Metallurgy Principles*, 4th ed. Stanford: Cengage Learning, 2009.
- [96] I. Tamura, H. Sekine, and T. Tanaka, *Thermomechanical processing of high-strength low-alloy steels*. Butterworth-Heinemann, 2013.
- [97] A. Monsalve *et al.*, "Obtention of a Multiphasic Steel from a 0.084%C, 1.44% Mn and 0.81%Si Steel," *Rev. Lat. Met. Mat.*, vol. 33, no. 2, pp. 254–264, 2013.
- [98] D. Dowson, C. M. Taylor, T. H. C. Childs, and M. Godet, *Thin Films in Tribology*. London: Elsevier, 1993.
- [99] D. S. Burnett, P. J., Rickerby, "The Relationship Between Hardnes and Scratch Adhesion," *Thin Solid Films*, vol. 154, no. 154, pp. 403–416, 1987.
- [100] M.J. Neale, "Lubrication and Reliability Handbook," *Lubr. Reliab. Handb.*, 2001.
- [101] K. Kato and K. Adachi, "Wear Mechanisms," in *Modern Tribology Handbook*, B. Bushan, Ed. Columbus, OH: CRC Press, 2001, pp. 273–300.

- [102] B. Bhushan and A. V. Kulkarni, "Effect of normal load on microscale friction measurements," *Thin Solid Films*, vol. 278, no. 1–2, pp. 49–56, 1996.

APPENDIX A: CHARACTERISTICS OF THE API 5L X65 STEEL

Steel can be defined as a solid solution of iron with alloying elements such as carbon and silicon [92]. Even at very low concentrations of carbon, the mechanical properties of steel, such as toughness, yield strength, and hardness can be significantly enhanced [92]. Depending on the heat treatment and content of carbon, steel can attain different mechanical properties depending upon the developed microstructure [92]–[94]. The microstructure can be defined as the microscopy-observed phase structure of steel revealed by a metallographic etchant, typically a corroding agent [92], [95]. The phases of steel are mainly comprised of different crystallographic structures of iron and are shown in Figure 104.

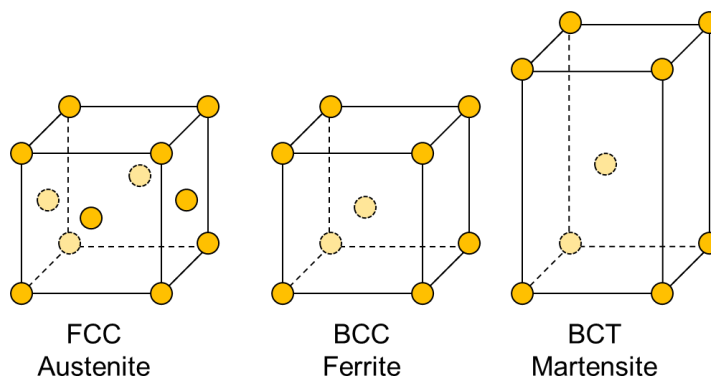


Figure 104. Crystal structures of iron's different phases. Face-centered cubic (FCC) corresponds to austenite or γ -iron; body-centered cubic (BCC) corresponds to α and δ -ferrite. The body-centered tetragonal unit cell (BCT) corresponds to a diffusionless transformation phase called martensite. Adapted from [92].

Figure 105 shows the Fe-C diagram showing the stable phases as a function of temperature and composition. The composition of the proposed steel is given in Table 13.

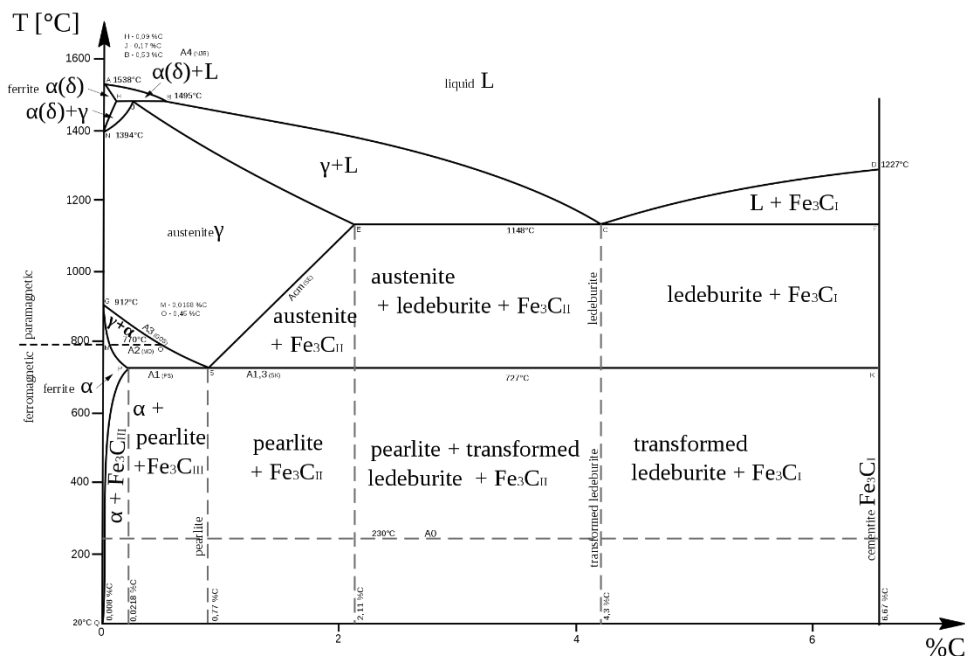


Figure 105. Binary phase diagram of iron (Fe) and carbon (C). Thermodynamically stable phases are shown: α -ferrite, γ -iron (austenite), δ -ferrite and cementite (Fe_3C). A1 is the eutectoid temperature; A2 is the α -ferrite austenitic transformation temperature; A3 denotes the hypoeutectoid temperature of austenite transformation; A_{CM} is the hypereutectoid temperature of austenitization. Retrieved from <https://upload.wikimedia.org/wikipedia/commons/thumb/e/e1/Fe-C.svg/2000px-Fe-C.svg.png> [Accessed: 02-Jan-2017].

Table 13

Chemical Composition of the API 5L X65 Steel (wt. %) Used in this Research

C	Mn	Si	P	S	Al	Ni	Cu
0.035	1.42	0.16	0.0055	0.0013	0.029	0.27	0.17
Mo	Cr	Nb	Ti	V	N	Ca	Fe
0.09	0.24	0.034	0.011	0.039	0.005	0.0018	Balance

The steel utilized in this research is a low-carbon steel (0.035 wt.%), which according to the Fe-C diagram shown in Figure 105, the stable phases are γ -iron at temperatures higher than approximately 830 °C, a solid solution of austenite and α -ferrite between 830 and 727 °C, and pearlite at lower temperatures. It also should be noted that a

high manganese content is present in the steel (1.42 wt.%). Manganese is an austenite stabilizer [92], [94], [96], which means that the austenite phase can be attained at a lower temperature than indicated in the Fe-C phase diagram. Nevertheless, the binary diagram of Fe-Mn indicates that the content of manganese in the steel would not significantly affect the austenitization point[94].

Finally, in terms of microstructure, the present steel has undergone a thermo-mechanical control process (TMCP) according to the steel provider. A thermo-mechanical control process is defined as a process that involves heating and controlled rolling to generate a more refined grain structure through recrystallization and deformation[96]. The process is illustrated in Figure 106. The first step is heating the steel up to the austenitization temperature, then the steel is rolled while it is cooled, generating refined austenitic grains. In a second rolling and cooling step, some grains deform and other remain unrecrystallized as the temperature drops. In a third simultaneous rolling and cooling process, the temperature decreases up to the two-phase zone and α -ferrite grains start nucleating on the γ -iron grain boundaries. Ferrite cannot dissolve as many alloying elements as austenite. Consequently, precipitation occurs causing hardening. Finally, the temperature reaches a point of no phase transformation. The final microstructure will depend upon the chemical composition and the cooling rate of the process [96]. In this case, due to the low content of carbon and high content of manganese, the final microstructure is expected to be α -ferrite[96].

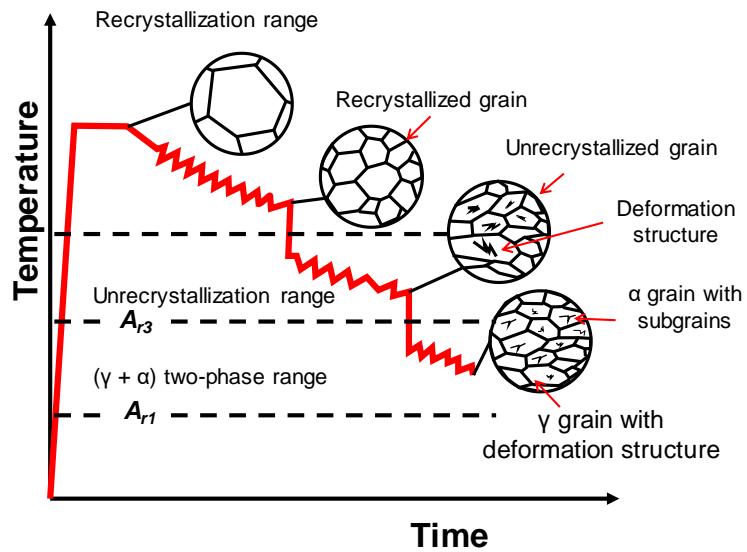


Figure 106. Thermo-mechanical control process. A_{r3} denotes the hypoeutectoid temperature of austenitic transformation and A_{r1} the eutectoid temperature. Adapted from [96].

By etching with 2% Nital, the microstructure of a steel specimen revealed the presence of ferrite as shown in Figure 107 and Figure 108.

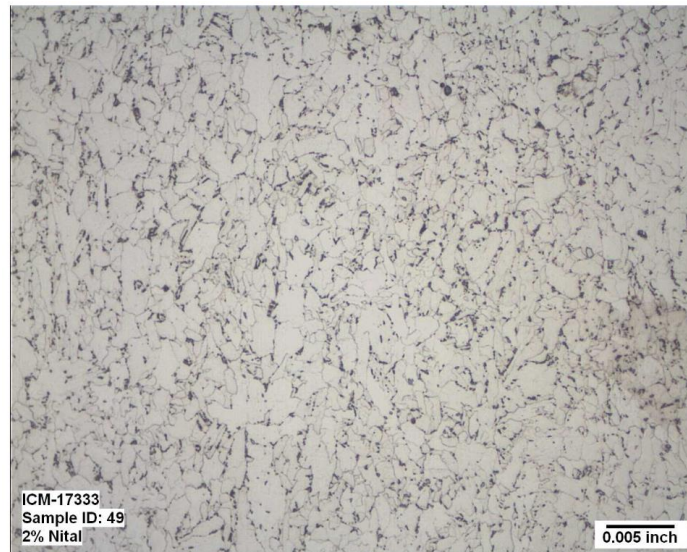


Figure 107. Microstructure of the proposed X65 steel. Ferrite is the predominant phase.

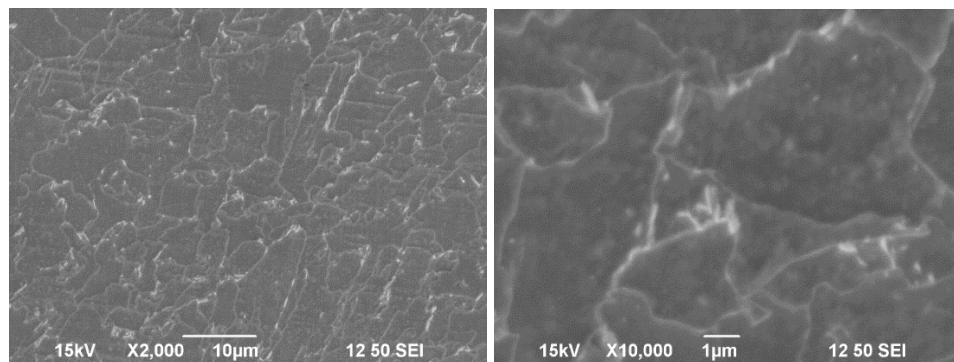


Figure 108. SEM images of the microstructure of the proposed X65 steel. Ferrite is the predominant phase.

In order to confirm the presence of α -ferrite as expected from the Fe-C diagram phase, XRD was performed on the steel specimen. By comparison with the literature [97], the XRD pattern indicates the presence of α -ferrite as shown in Figure 109. Consequently, it is concluded that the predominant phase on the X65 steel used in this research is ferrite with precipitated carbides.

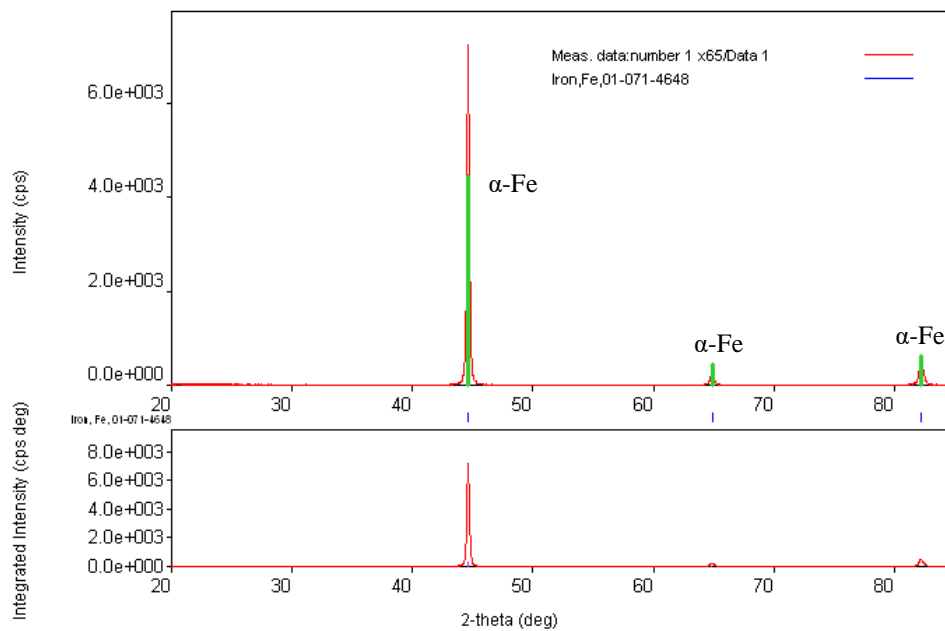


Figure 109. XRD pattern of the X65 steel showing the presence of ferrite.

APPENDIX B: STATISTICAL ANALYSIS FOR THE VICKERS INDENTATION METHOD

The basic principle of the Vickers indentation method is that the print of the indenter is proportional to the loading force of the apparatus. This condition makes hardness independent from the loading force as long as the diagonals of the prints are equal. In order to test the validation of each indentation, a steel sample with no corrosion product was used to perform Vickers hardness tests at different loading rates; 10 measurements at different loads were taken (at 10, 25, 50, 200, 300, 500 and 1000 gf). The results are shown in Figure 110. Such results indicate that there is not a significant difference in the hardness obtained at different loading forces.

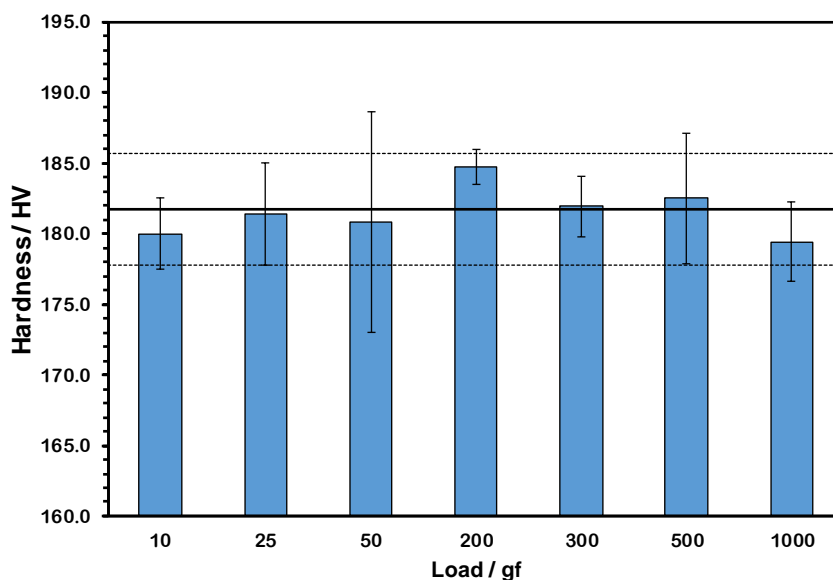


Figure 110. Blue bars represent the average value of each load population. Error bars: standard deviation for each load population. Horizontal black solid line: average of the whole sample population. Horizontal dashed lines: ± 1 standard deviation of the whole sample population.

APPENDIX C: LATERAL FORCE MICROSCOPY

The basic principle of atomic force microscopy (AFM) is depicted in Figure 111.

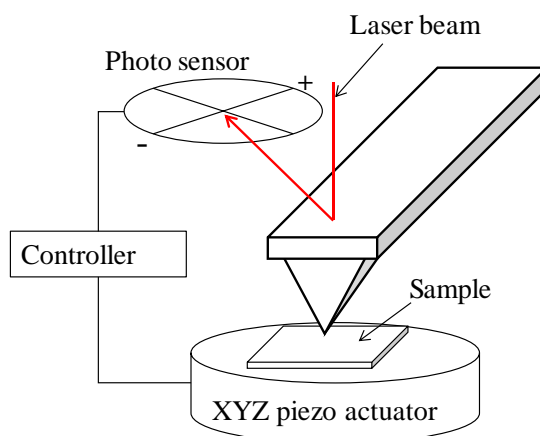


Figure 111. Basic principle of atomic force microscopy (AFM). A cantilever is placed upon a sample surface. The XYZ piezo actuator moves the sample in any desired direction in the XYZ plane. Such movements in combination with the sample interface morphology generate a torsion / bending on the cantilever. The photo sensor registers the movements of the cantilever as the displacement of the laser beam reflected from the cantilever is proportional to the torsion/bending of the cantilever. The controller sends a feedback signal to the piezo actuator for a more precise movement.

Lateral force microscopy (LFM) is a specific application of the AFM. As its name suggests, this technique utilizes lateral movements to produce friction forces between the tip and the surface of the sample. Such a movement also produces a torsion angle (β) as shown in Figure 112.

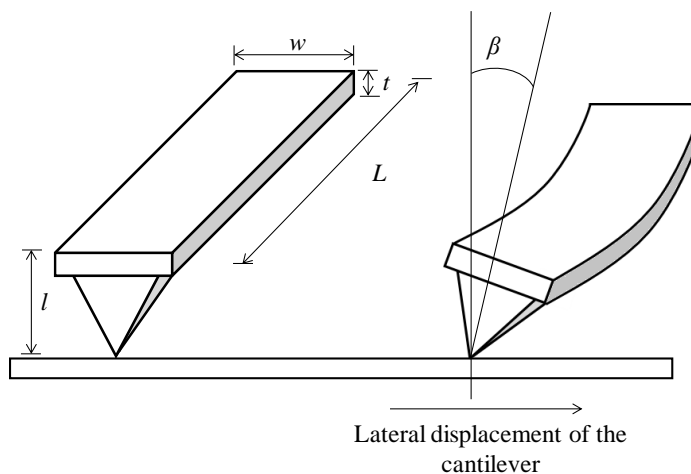


Figure 112. Torsion angle (β) of the cantilever generated by lateral displacement of the cantilever. L is the length of the cantilever; l is the height of the tip; w is the width and t is the thickness of the cantilever.

The torsion angle is proportional to the aforementioned friction and, at the same time, the torsion is registered by the deflection of the laser beam detected by the photo sensor as shown in Figure 113.

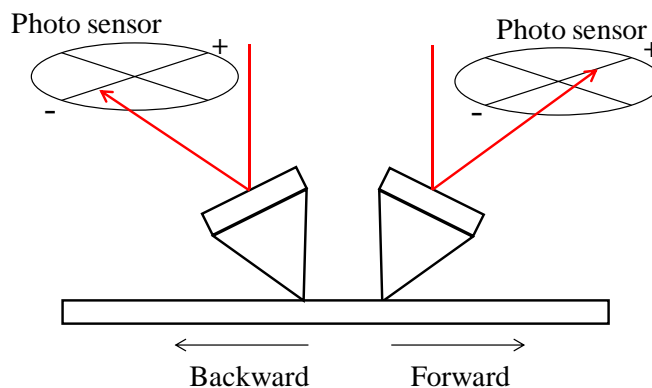


Figure 113. Changes in the laser deflection due to torsion recorded by the photo sensor. At the right, the forward displacement of the cantilever (trace) generates a positive deflection of the laser beam on the photo sensor. At the left, the backward movement of the cantilever (retrace) generates a negative deflection of the laser beam on the photo sensor. Such deflection is proportional to the friction force between the tip and the sample's surface.

Forward displacement of the cantilever causes a positive bias on the photo sensor, recorded in Volts; while a negative displacement of the cantilever generates a negative bias on the photo sensor also registered in Volts. Such forces are plotted in a voltage *versus* displacement curve (found in literature as “friction loop” [79], [80]), as shown in Figure 114. From this plot, the voltage difference between the trace and the retrace (ΔV) can be obtained.

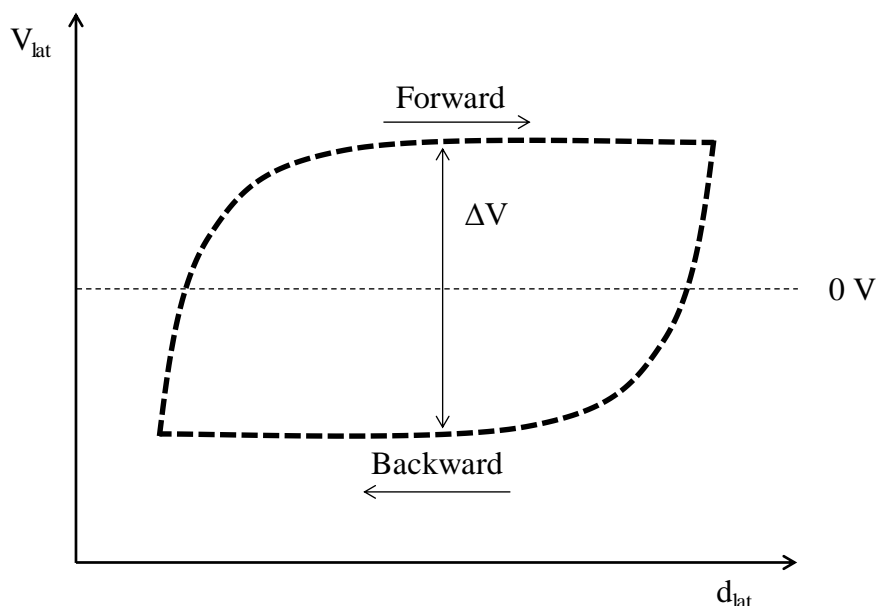


Figure 114. Voltage recorded from the lateral displacement of the cantilever. In the graph: x-axis represents the lateral displacement, y-axis represents the voltage recorded in the displacement of the cantilever. ΔV is the difference in voltage between the forward (trace) and backward (retrace) displacement of the cantilever.

Regarding calculations, the previously-mentioned torsion angle, β , can be calculated from the voltage difference between the trace and retrace. [79]

$$\beta = \frac{\Delta V}{2C_{lat}} \quad (32)$$

Where C_{lat} is the lateral torsional force constant, which is proportional to the vertical spring constant (k):

$$C_{lat} = mk \quad (33)$$

m is the ratio of the lateral and vertical displacement-voltage sensitivity:

$$m = \frac{m_{lat}}{m_{ver}} \quad (34)$$

The slopes m_{lat} and m_{ver} are obtained from the displacement-voltage curves as shown in Figure 115.

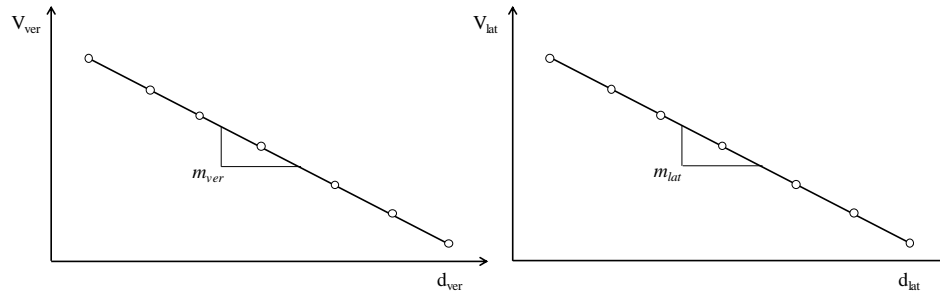


Figure 115. Voltage-displacement curves for vertical and lateral displacement.

The lateral force is then defined to be proportional to the torsion angle (β) the ratio of the torsional force constant (C_{tor}) and the length of the tip and the cantilever in the form:

$$F_{lat} = \frac{C_{tor}}{Ll} \beta \quad (35)$$

Where C_{tor} is dependent on the mechanical properties and dimensions of the cantilever:

$$C_{\text{tor}} = \frac{Gwt^3}{3} \quad (36)$$

Where G is the shear modulus of the cantilever, w is the width and t is the thickness of the cantilever as shown in Figure 112.

Finally, the normal deflection sensitivity, α , is taking into account and the lateral force can be calculated as [79][80]:

$$F_{\text{lat}} = \left(\frac{Gwt^3}{3L^2} \right) \left(\frac{\alpha}{m} \right) (\Delta V) \quad (37)$$

Or:

$$F_{\text{lat}} = k_{\text{lat}} \alpha_{\text{lat}} (\Delta V) \quad (38)$$

Where α_{lat} is the lateral deflection sensitivity of the tip.

APPENDIX D: SCRATCH MODELS FOR ADHESIVE AND COHESIVE FAILURE

The Ollivier and Matthews [58] model, and associated formulae, was insufficient to describe the delamination behavior of all the corrosion product layers, namely, iron sulfide and iron carbonate layer. The Ollivier and Matthews formulation assumes deformation of the substrate when the delamination occurs. There is also an implicit assumption that the friction force is negligible in comparison to the plowing term, as fully described by Bull, *et al.*[49] However, there were some observations in the tests that might be at odds with the assumptions (and thereby, with the model). The first observation is that the delamination of corrosion product layers grown under dewing conditions occurs with a negligible deformation of the substrate. The second is that the recorded coefficient of friction is in the order of frictional forces of two sliding bodies (between 0 to 0.3)[98]. Therefore, a more comprehensive model that accounts for the friction is necessary to describe the behavior of the layers. Next, some of the most common models in the open literature will be briefly discussed; their potential application for corrosion science is also noted.

Benjamin and Weaver

Benjamin and Weaver [59] initially assumed that the tip of the scratch tester can be modeled as a hard sphere. Regarding the interaction with the film/substrate, the authors distinguished two possible scenarios: classical Hertzian contact between the “sphere” and a flat surface, and plastic deformation of the substrate. However, the authors only developed the case for plastic deformation (a similar scenario assumed by the Ollivier and Matthews formulation). The tangential force (F_T) was then proposed to be a

function of the forces to produce a plastic deformation (hardness of the substrate), the forces of adhesion between the film and the substrate, and the plowing term producing deformation and loss of adhesion:

$$F_T = \frac{d^3}{12R} H_S + \frac{\pi\tau}{4} d^2 + dtH_F \quad (39)$$

Where d is the scratch track width, R is the tip radius, H_S is the substrate hardness, τ is the shear stress between the film-substrate interface, t is the thickness of the film, and H_F is the hardness of the film.

In terms of applicability for corrosion science, the model is built upon the same assumptions as Olliver and Matthews, adding the term for the thickness and hardness of the film. Therefore, the results and their analyses might not be significantly different from those initially presented in the current thesis.

Laugier

As described in the introduction of this thesis, Laugier [61], [62] introduced a model for scratch testing accounting for compressive stresses within the film (σ_x), Poisson's ratio (ν), coefficient of friction between the indenter and the coating (μ), and Young's moduli for the substrate and the film. Laugier assumed that the compressive stresses within the film play a governing role when Hertzian contact is assumed (at the initial step of the scratch). Later, the normal force (F_N) and plowing term play a major role when the tip is penetrating the film. Consequently, the first part of the scratch experiment can be quantified by the classical Hertzian contact radius of a sphere (a) on a flat surface [61], [62]:

$$a^3 = \frac{3}{4} F_N R \left(\frac{1 - \nu_S^2}{E_S} + \frac{1 - \nu_F^2}{E_F} \right) \quad (40)$$

Where the subscript “S” denotes substrate and “F” denotes film.

Following Laugier’s derivation [61], [62], the total compressive stress (σ_x) between the indenter and the film can be expressed as:

$$\sigma_x = \frac{F_N}{2\pi a^2} \left[(4 + \nu_S) \frac{3\pi\mu}{8} - (1 - 2\nu_S) \right] \quad (41)$$

Finally, Laugier [61], [62] argued that the shear stress acting on the substrate-film interface (τ) was approximately equal to:

$$\tau \approx \frac{\sigma_x a}{R} \quad (42)$$

However, this expression is only valid when $a \ll R$. In the case of the corrosion product layers tested in this thesis, the values of a are lower than R by less than 40 to 50%. Therefore, the applicability of Equation (42) must be treated with caution.

Burnett and Rickerby

Another model to describe the forces acting during the scratch test was proposed by Burnett and Rickerby [99]. The authors assumed that the governing parameters in the delamination of a film from a substrate were the elastic-plastic indentation stress, the internal stresses, and the plowing term. The authors proposed the following formula to describe the acting forces during the critical load event (L_C). The critical load is the normal force required to produce the delamination of the film from the substrate.

$$L_C = \frac{A_C}{\nu_F \mu} \left(\frac{2E_S W}{t} \right)^{0.5} \quad (43)$$

Where A_C is the cross-sectional area of the scratch track and W is the work of adhesion, a term that is the sum of all the forces acting on the interface between the substrate and the film, resulting in the delamination event.

In summary, the most commonly used scratch models in the open literature account for the forces involving the delamination event. Whereas most of them assume that the delamination occurs when the substrate experiences plastic deformation, the model from Laugier assuming Hertzian contact can potentially be used for situations where the plastic deformation assumption does not apply. However, the model requires specific inputs, such as the values for the Poisson's ratio and Young modulus of the film; this makes it challenging for potential applications.

APPENDIX E: PRELIMINARY RESULTS ON WEARING

Introduction

The data in the current thesis indicated that the shear stress required to produce cohesive and adhesive failures of corrosion product layers are orders of magnitude higher than the values typically found in commercial oil and gas transmission pipelines. A possible explanation for the black powder formation associated with the flow in pipelines can be the damage produced by wear. Wear can be defined as gradual material removal from a surface caused by the mechanical interaction between two surfaces [91], [100], [101]. The removal can be caused by microfracture, chemical dissolution, or by melting at the contact interface [101]. The most commonly reported mechanisms of wear can be described as adhesive, abrasive, fatigue, and corrosive [101]. Moreover, the wear mode of a type of layer/material might not be exclusive. A layer/material can undergo different wear mechanisms at various times. For instance, a layer can experience frictional heating, then undergo chemical film formation [101].

Wear is typically reported in units of volume of material removed over force applied (*i.e.*, mm^3/mN) [91], [101]. The removed volume is also commonly plotted *versus* the number of cycles during the wear testing [91], [100], [101]. The resulting plots are called wear volume curves [91], [100], [101]. Depending on the behavior of the material, there are three types of wear volume curve, as shown in Figure 116.

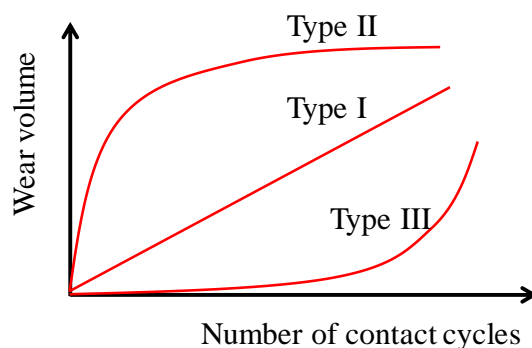


Figure 116. Types of wear curve. Adapted from [91]

Type I (or ideal wear) indicates that the wear occurs at a constant rate during the whole process, *i.e.*, the same volume of material is removed at each cycle. Type II implies that a material initially experiences a high wear rate until a critical value is achieved, then reaches a low steady wear rate. Finally, Type III represents a material that undergoes low wear rate in the beginning, but after a critical number of contact cycles experiences a change from low to high wear rate. Type II is commonly reported for metals [91], [101], whereas Type III is usually associated with ceramics [91], [101], [102]. The reasons behind the Type III wear mode are associated with crack formation and propagation for the material in question [91], [101]. At the same time, crack initiation and propagation is dependent on the surface finish, material properties, and frictional conditions (lubricated or unlubricated contact) [91].

Working Hypothesis

The cohesive failure of an iron carbonate layer can be the cause of the presence of iron carbonate in the black powder composition. Therefore, the constant addition of forces causing minimum damage to the surface is hypothesized to cause the cohesive

failure of an iron carbonate layer. As a second hypothesis, the effect of forces (*i.e.*, thickness diminution of the layer) is postulated to be additive.

Such hypotheses can be tested *via* scratch test. By performing multiple passes in tests, it is possible to determine if the forces applied on a scratch track are additive to its equivalent single scratch test, and subsequently produce a cohesive failure of the layer.

Experimental Method

The process of testing the hypothesis is illustrated in Figure 117. A constant load scratch test is repeated over the same zone. The thickness of the layer is recorded at each pass until a cohesive failure is detected. With the recorded information, a wear volume curve for, say, iron carbonate can be constructed to determine the type of wear (similar to Figure 116). The steps to construct a wear volume curve are the following:

1. Determine a load at which minimum damage is produced without reaching the cohesive failure by using progressive load scratch testing. Corroborate the result with constant load scratch tests.
2. Once the working force has been determined, the next step is to perform a multiple-pass scratch test at a constant load and record the thickness of the layer at each step from the penetration depth of the scratch test. The process is illustrated in Figure 117.

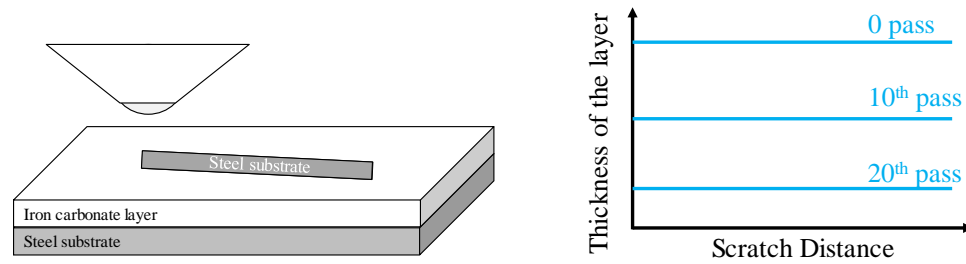


Figure 117. Multiple-pass constant load scratch test to determine the diminution of the layer thickness.

- By using the penetration depth from the scratch test, determine the wear volume (V) by using the partial volume of a sphere (tip) as shown in Figure 118 and calculated with Equation (44).

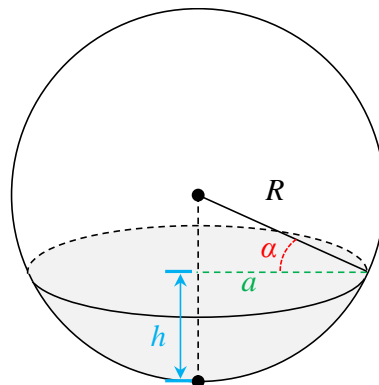


Figure 118. The partial volume of a sphere based on height (h). R is the radius of the tip, a is the scratch width left by the test; α is the angle formed between R and a .

$$V = \frac{\pi h}{6} (3a^2 + h^2) \quad (44)$$

- Plot the volume *versus* the number of passes.

Preliminary Results

An iron carbonate layer was developed as per Table 1. In order to obtain a reference plane for each scratch pass, *i.e.*, homogenize and level the layer, the sample was sequentially polished with diamond paste from 9 to 0.025 μm . In order to determine the working normal force, a progressive load scratch test from 0.1 to 800 mN was conducted as shown in Figure 119.

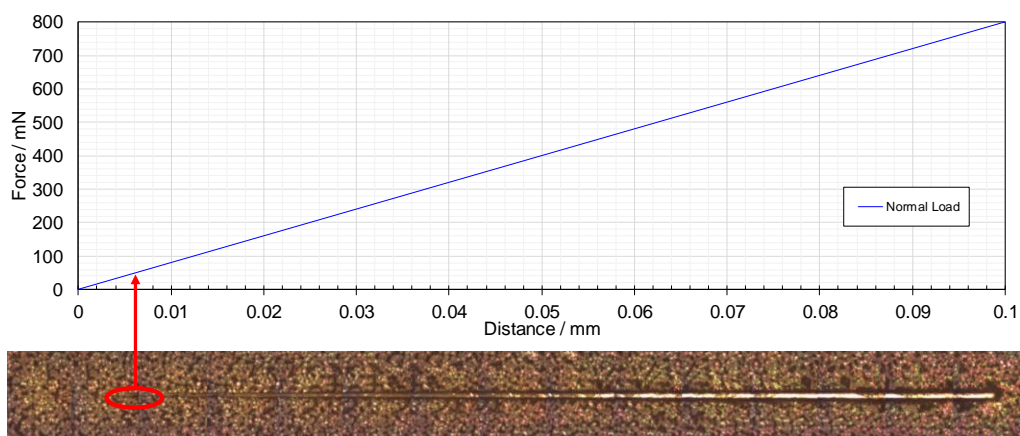


Figure 119. Progressive load scratch test to determine the working force for the wear test.

Optical microscopy was utilized to determine the force that produced minimum damage, without producing an adhesive failure, on a polished iron carbonate layer. The force was *ca.* 70 mN. The value was confirmed by performing constant load scratch tests at 50 and 70 mN as illustrated by Figure 120. The damaged zone at 70mN is illustrated in Figure 121

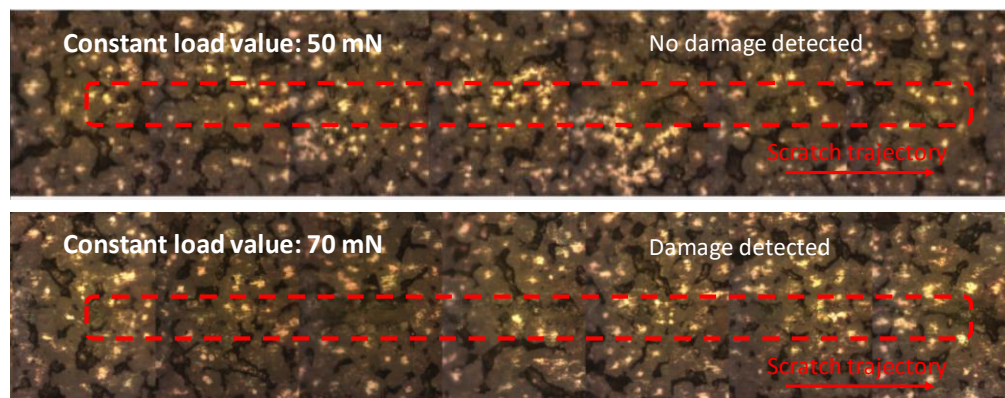


Figure 120. Constant load scratch test to determine the working force for wear test.

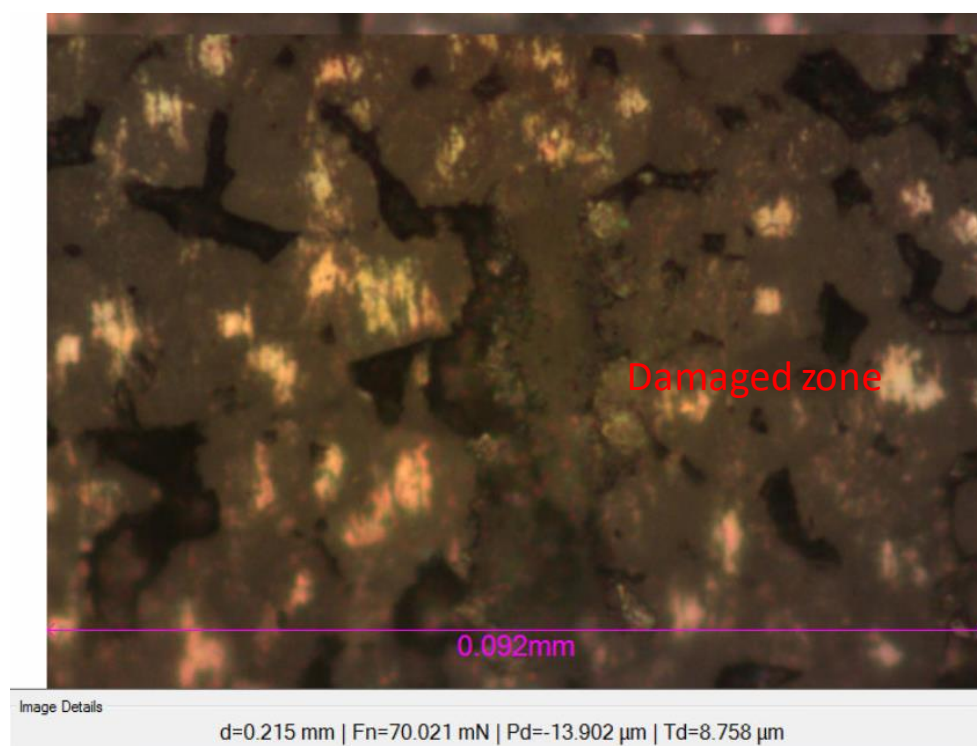


Figure 121. Constant load scratch test to determine the working force for the wear test.

With the working force determined, the multiple-pass scratch test was conducted 6 times. The recorded penetration depth and the forces involved are shown in Figure 122.

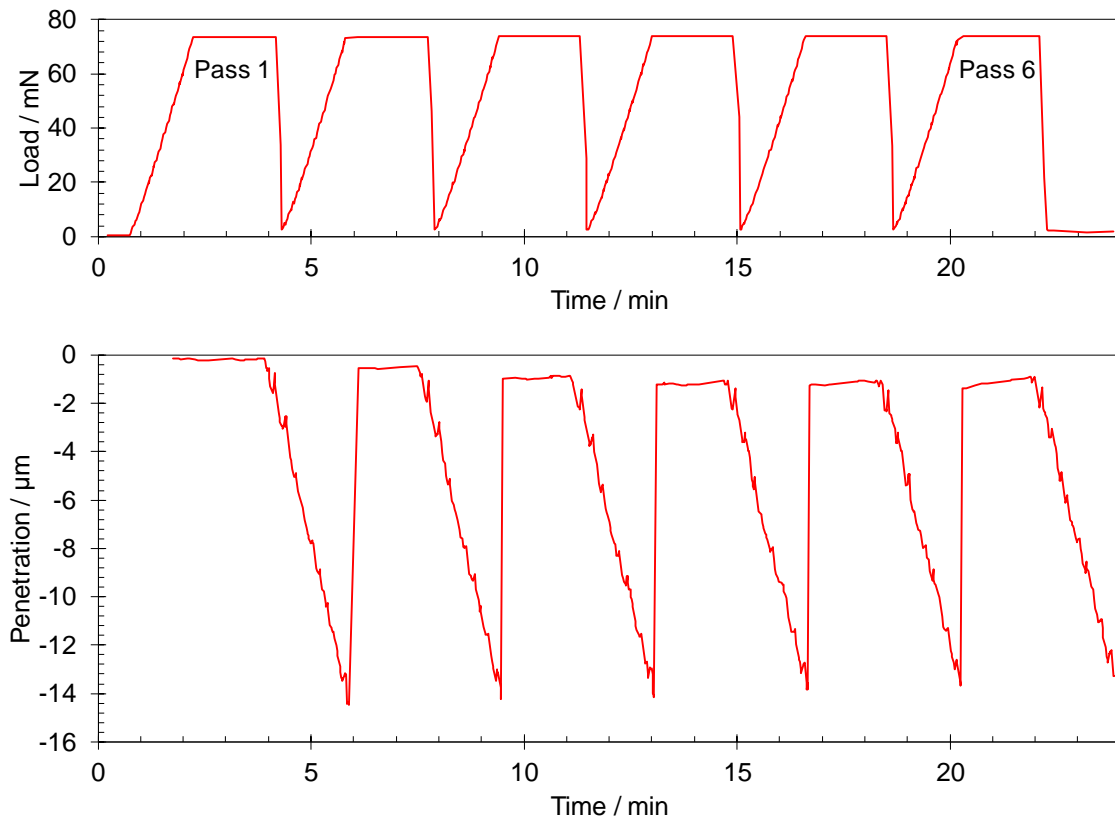


Figure 122. Multiple-pass scratch test. Top graph: loading force through multiple passes on the same zone. Lower graph: penetration measured by the scratch tester at different passes.

Finally, the wearing volume (V) was calculated using Equation (44) and plotted against the number of passes, as shown in Figure 123. Wear rate (WR) was calculated by taking the slope of the wear volume curve and dividing by the applied normal force [101]; the initial wear rate is *ca.* $0.27 \mu\text{m}^3/\text{mN}$ (namely, for the first two passes). After the third pass, the wear rate increased by a factor of 2 (up to $0.56 \mu\text{m}^3/\text{mN}$). This behavior is consistent with the Type III wear curve described in Figure 116.

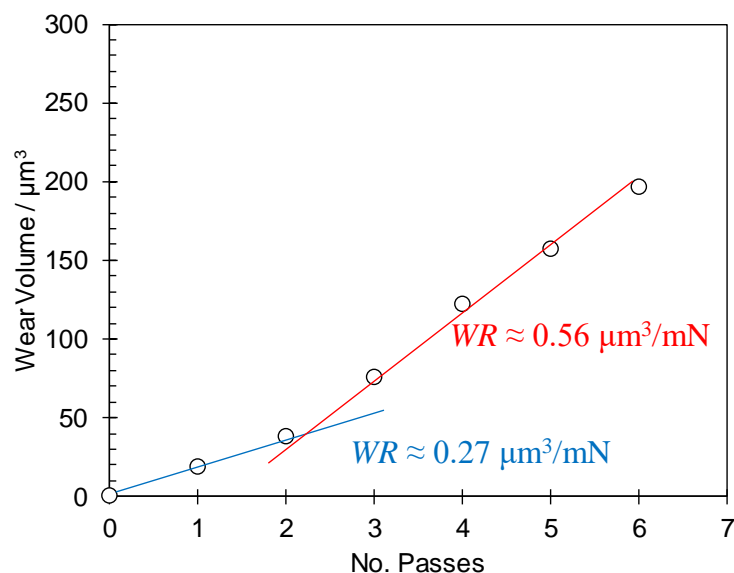


Figure 123. Wear volume curve for the polished iron carbonate layer. Wearing rates (WR) suggest that the wear is obeying the Type III wear curve behavior.

Such a result suggests that the delamination of the iron carbonate layer is more likely to happen with further passes at the same loading force. However, more tests are required to determine the exact number of passes.

Finally, the additive effect hypothesis was tested by performing a 1 pass 420 mN constant load scratch test with the initial assumption that 6 passes of 70 mN would sum up to 420 mN of total damage. However, the profilometry analyses (shown in Figure 124) revealed that after 6 passes of a scratch test of 70 mN loading force the thickness was reduced *ca.* 1.2 μm , whereas the single pass 420 mN constant load scratch test diminished the thickness by *ca.* 2.5 μm . This difference produced a deviation of a factor of two. This result suggests that the multiple passes scratch test effects are not additive by a simple sum of forces.

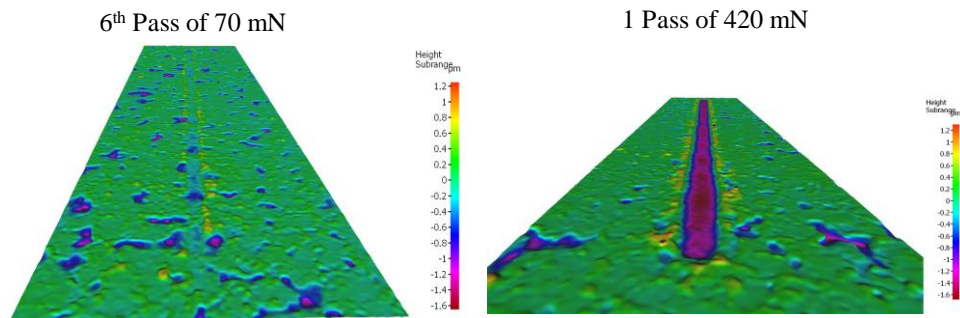


Figure 124. Profilometry of a 6-pass 70mN constant load scratch test, and a single pass 420 mN constant load scratch test.

Summary

- Iron carbonate is consistent with the Type III wear curve (associated with ceramics). More work is needed to determine the number of passes to produce an adhesive failure.
- Multiple passes in a constant load scratch test are additive in terms of thickness reduction. However, the addition is not a linear sum of forces. Its effect regarding deformation and delamination is therefore non-linear (in comparison to a single test).

APPENDIX F: FRACTURE TOUGHNESS AT THE CROSS-SECTION

Introduction

Fracture toughness is dependent on the residual tensile stresses on thin layers [98]. Therefore, the distribution of such stresses might produce anisotropy in the corrosion product layers. For example, the cross-section fracture toughness would not be the same as the fracture toughness from the top. Consequently, the purpose of the study discussed in this appendix was to explore the fracture toughness in the cross-section of the corrosion product layers, namely, iron carbonate, calcium carbonate, and iron calcium carbonate. The reader is reminded that the iron sulfide layer did not exhibit K_{IC} fracture toughness behavior, therefore, the analysis did not include iron sulfide.

Experimental Procedure

The specimens were mounted in epoxy and cut in cross-section. Next, the specimens were sequentially ground with 180, 400, and 600 grit sandpaper. Later, the specimens were sequentially polished with 9, 3, and 0.25 μm diamond suspension with a polishing cloth. Vickers nanoindentation tests were performed at 20 mN loading force (2 mN for iron carbonate). In order to calculate the fracture toughness (K_{IC}), optical microscopy was used to measure the crack length and the diagonals from the Vickers' indenter print.

Iron Carbonate

The iron carbonate presented a challenge for the cross-section relating to the thickness of the layer. Since the maximum thickness of the layer was *ca.* 6 μm , the

indentations at a loading force of 20 mN produced cracks invalid for the fracture toughness analysis as shown in Figure 125.

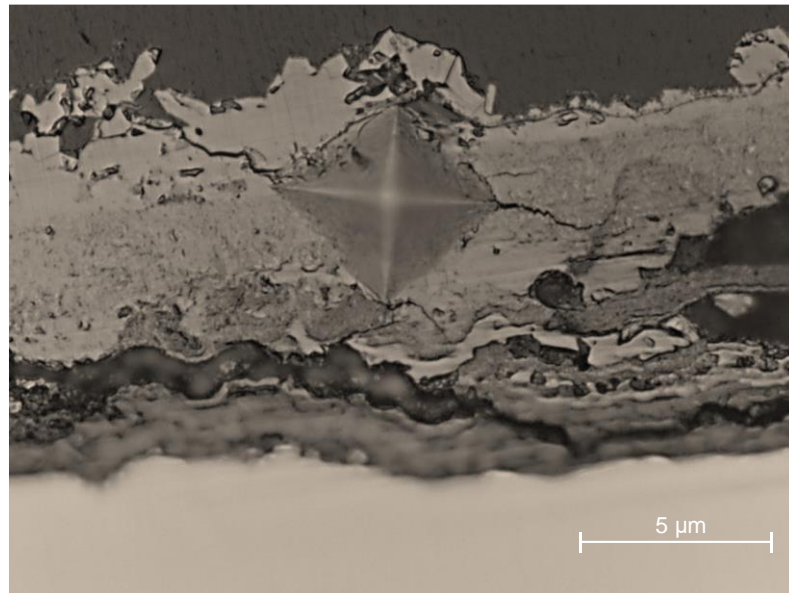


Figure 125. First attempt to determine the K_{IC} mode fracture toughness in the cross-section of iron carbonate. The crack propagation was stopped by the epoxy and the metal-layer interface.

As a solution, the indentation forces were diminished by an order of magnitude (2 mN), producing measurable cracks as shown in Figure 126. The fracture toughness of the iron carbonate was determined to $1.5 \pm 0.2 \text{ MPa m}^{-1/2}$, which is in good agreement with the fracture toughness in the top view ($1.7 \pm 0.1 \text{ MPa m}^{-1/2}$).

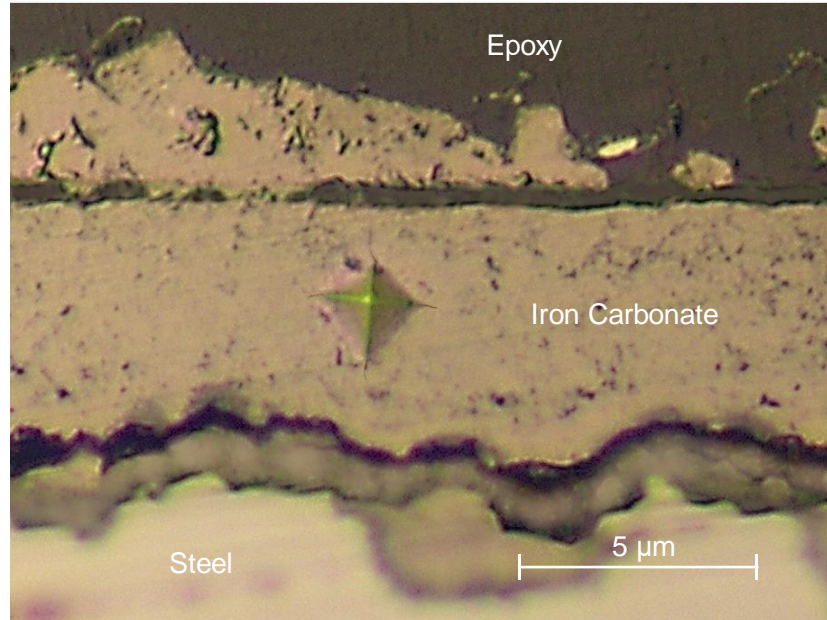


Figure 126. Determination of K_{IC} mode fracture toughness in the cross section of an iron carbonate layer.

Calcium Carbonate

The fracture toughness in the cross-section of a calcium carbonate was determined from Figure 127 and Figure 128. As a result, the fracture toughness was $0.85 \pm 0.1 \text{ MPa m}^{-1/2}$. This value is in good agreement with the fracture toughness obtained from the top view layer ($1 \pm 0.2 \text{ MPa m}^{1/2}$).

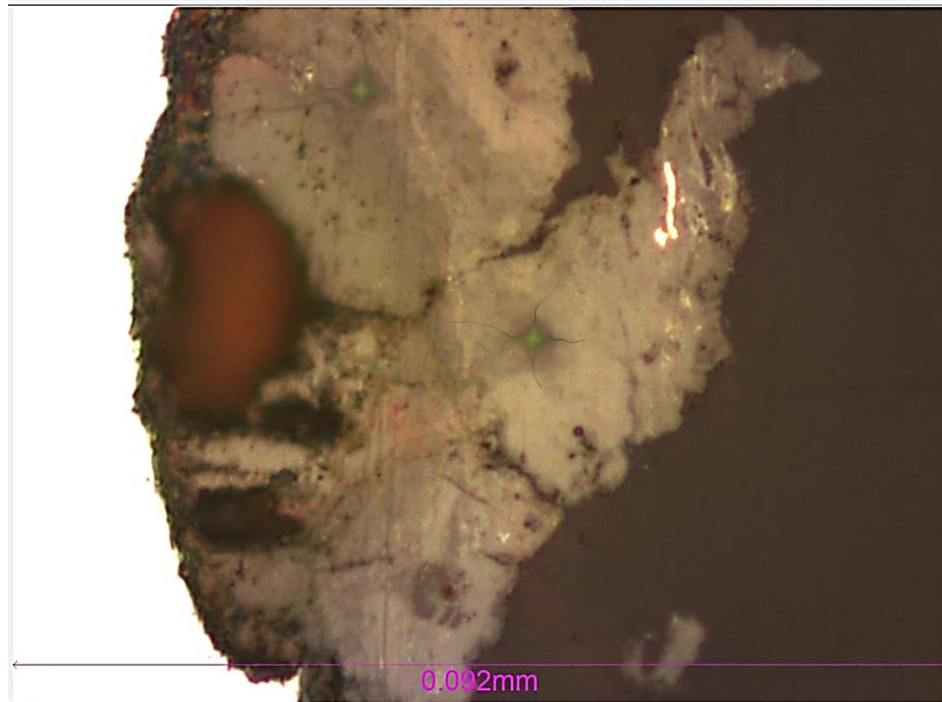


Figure 127. Determination of K_{IC} mode fracture toughness in the cross-section of a calcium carbonate layer.

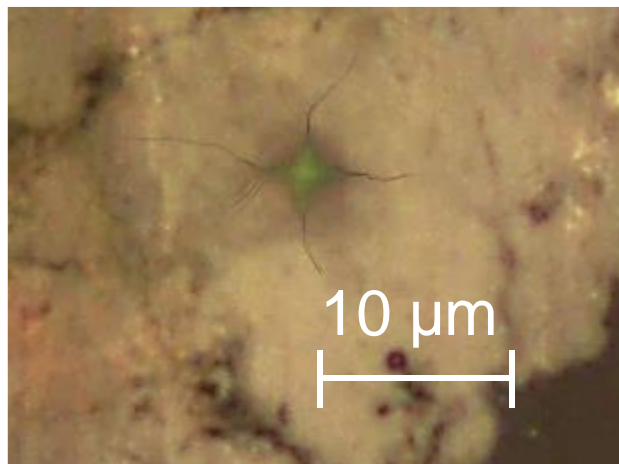


Figure 128. Zoomed image of the Vickers' indentation print from Figure 127.

Iron Calcium Carbonate

Finally, the fracture toughness of samples of iron calcium carbonate layers was determined. Figure 129 and Figure 130 show the indentation prints at different parts of the cross-section.

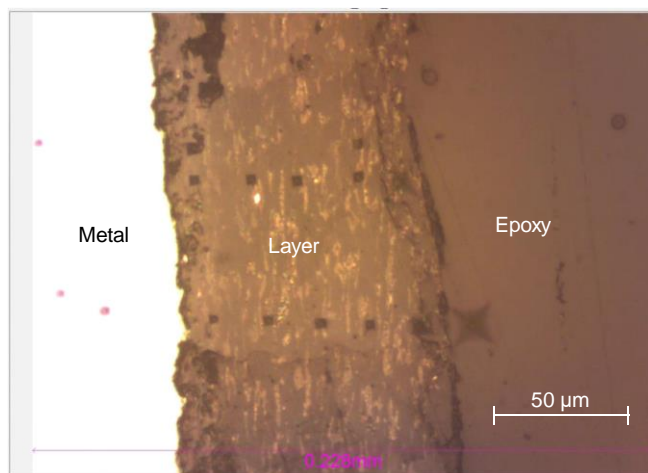


Figure 129. Indentation pattern for fracture toughness determination.

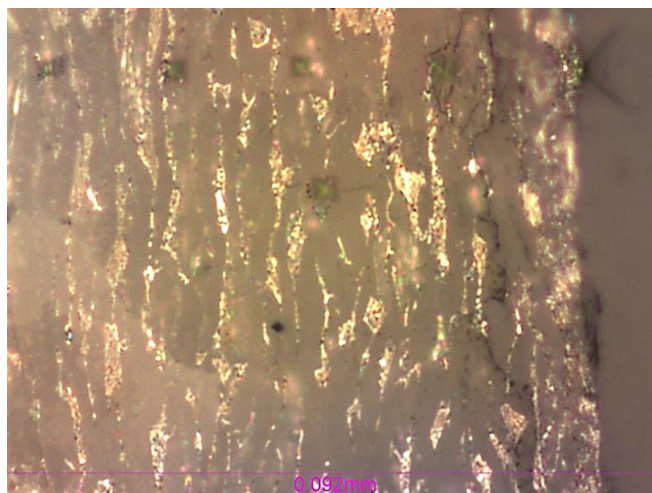


Figure 130. Zoomed image of the Vickers' indentation prints from Figure 129.

The summary of the fracture toughness data obtained from the cross-sections as well as their counterpart top views is summarized in Figure 131. It is observed that the average values between both, cross-section and top, are in good agreement.

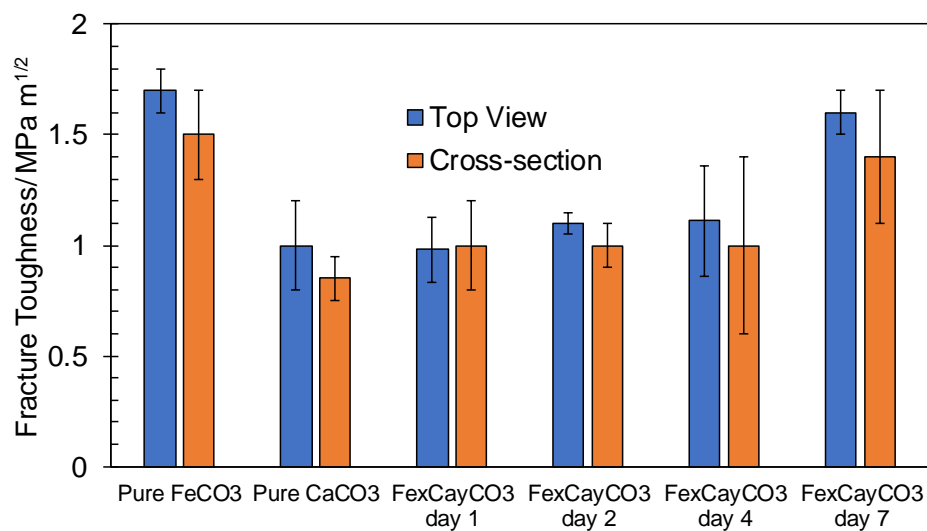


Figure 131. Summary of fracture toughness (K_{IC}) obtained at the cross-section and the top view of the layers.



OHIO
UNIVERSITY

Thesis and Dissertation Services